"Manifestations of Atmospheric Gravity Waves in the Airglow at 95 km."

by

P.G. Jacob, B.Sc.(Hons.)
Mawson Institute for Antarctic Research

Submitted in fulfilment
of the requirements for the degree of
Doctor of Philosophy.

University of Adelaide

November, 1985.

To Claire and Jessie

This thesis contains no material which has been accepted for the award of any other degree or diploma in any University and, to the best of my knowledge and belief, it contains no material previously published or written by another person, except where due reference is made in the text of the thesis. I consent to this thesis being made available for photocopying and loan by the librarian of the University of Adelaide upon acceptance of the degree.

P.G. Jacob.

CONTENTS

ABSTRACT.

It has been just over twenty years since internal gravity waves have been generally considered as playing a major role in atmospheric dynamics. These waves provide an efficient mechanism for the transfer and redistribution of energy throughout the atmosphere and there is little doubt as to their importance in the understanding of the complex nature of our atmosphere.

This thesis describes an optical method for remotely sensing a portion of the atmospheric gravity wave spectrum and investigating the energetics and dynamics of these waves through observation of the atmospheric nightglow. To such an end, the λ557.7 nm emission line was chosen for its high intensity, compared to other emissions, and its well defined, narrow emission layer at 95 km. The interaction of gravity waves with this emission layer allows wave periods up to four hours and horizontal phase velocities to be inferred from spectral analysis of photometric measurements made from three spaced fields of view in the sky. The analysis of the observations gives results which are entirely consistent with the linear theory of gravity waves as outlined in the thesis.

By reverse ray tracing the detected waves from the 95 km observation level, likely generation mechanisms in the troposphere are identified, with the main sources being upper level jet streams. Instances of frontal and thunderstorm activity are also noted. The observations indicate that the majority of detected waves originate

from the lower regions of the atmosphere with the direction of propagation of these waves partially polarized by the middle atmosphere wind system.

Measurements of the relative intensity of fluctuations in the λ557.7 nm emission have enabled estimates of the mean energy density of gravity waves to be made and extrapolated to cover the entire gravity wave spectrum with a mean spectral index of 1.7.

Restrictions in gravity wave vertical wavelengths, imposed by the middle atmosphere and wave dissipation, also limit the range of their vertical group velocities. This confinement along with energy density estimates, permit an evaluation of the average vertical energy flux of the entire gravity wave spectrum incident on the 95 km level. A value of 15 mWm^{-2} for the mean energy flux of gravity waves is consistent with those of other workers using completely different techniques. It is also established that over 85% of the energy flux at the 95 km level is contributed by waves with periods less than four hours.

SUMMARY.

In order to introduce common atmospheric terminology, Chapter 1 deals with the structure of the earths stationary atmosphere with the effects which give rise to airglow. Particular attention is payed to the λ557.7 nm nightglow emission, its height distribution and generation mechanisms. Chapter 2 introduces atmospheric waves, referring mainly to the underlying theory of gravity waves, defining wave parameters and variables used throughout the text. Considerable effort was made to prevent the text from resembling a Greek alphabet soup by presenting the wave theory concisely, using the simplest of atmospheric models. The propagation of gravity wave energy is discussed along with the means by which wave energy and momentum can be transferred to the atmosphere at critical levels and via dissipation. Finally the influence of gravity waves on the λ557.7 nm emission layer is considered which leads logically to Chapter 3 where the instrument, specifically designed to observe this effect, is presented. The general layout and workings of the instrument are discussed.

To decompose the observed gravity wave field into its separate components, a cross spectral analysis technique is used; its application is described in Chapter 4. The realization of gravity wave horizontal phase velocity is presented along with the error estimates incurred from the analysis procedure. Preliminary results are discussed.

In the following chapter observed waves are traced from the 95 km level to the tropopause. Although more complicated ray tracing techniques exist, it was felt due to the unavoidable uncertainty in the required wind profiles, that the more sophisticated methods would provide little benefit. In fact the simpler multilayer approach used with mean monthly wind data give very useful results. Possible wave generation sources are identified and their generating mechanisms briefly discussed. It is concluded that the majority of gravity waves detected at 95 km are generated low in the atmosphere. The remaining two chapters are concerned with the spectra of gravity waves and show how the observations of wave parameters and their power spectra may be used to estimate the mean energy density of gravity waves over their entire spectrum and to estimate the vertical energy flux.

ACKNOWLEDGEMENTS.

I would like to thank the Director of the Mawson Institute for Antarctic Research, Dr. Fred Jacka, for his supervision and optimistic guidance throughout this project. Thanks also to Don Creighton for his great assistance with the electronics and mechanical construction of the equipment, aided by the cheerful help of the Institutes technical staff. I mention too my fellow students for their comradeship.

Special appreciation to my wife and family for their continued support and understanding.

Chapter 1. The Stationary Atmosphere.

1.1. Introduction.

The main factors influencing the earths atmosphere are the earths gravitational and magnetic fields, the gases which make up the atmosphere and solar radiation. In a stably stratified atmosphere, under the influence of gravity, the atmospheric pressure and density decrease exponentially with altitude. This is generally expressed in the familiar hydrostatic equation

$$p=p_o \exp(-z/H)$$

where p_o is the pressure at some reference altitude z_o and H is the pressure scale height, defined as the increase in altitude necessary for the pressure to decrease by a factor of 1/e. A similar equation can be stated for the atmospheric density.

By far the most important energy source for the earth and its atmosphere is solar radiation. Energy from the sun not only is the source of life to the biosphere, but provides the driving force for the dynamics of the atmosphere and oceans. Even if only a stationary atmosphere is considered, solar radiation plays a major role in its structure. The sun radiates over the entire spectral range, from gamma rays to radio waves. The main constituents of the atmosphere, molecular oxygen and nitrogen, are dissociated and ionized by the shorter

wavelength radiation with the minor atmospheric constituents such as water vapour and carbon dioxide, also contributing to the active chemistry of the atmosphere, (Mc Ewan and Phillips, 1975).

The earths atmosphere can be divided into regions on the basis of its temperature structure. On average, above the earths surface the temperature decreases with altitiude, i.e. a positive lapse rate, up to a level between 10 km and 12 km known as the tropopause. The region below the tropopause is the troposphere where normal weather activity is confined. Above the tropopause the temperature increases with height through the region of the stratosphere. This heating is due to ultraviolet radiation, (λ200 nm-λ300 nm), being absorbed by atmospheric ozone, itself produced by the photodissociation of molecular oxygen at wavelenghts below λ290 nm. A further temperature maximum is reached at the stratopause near 50 km, above which the temperature once again decreases through the mesosphere to reach a minimum at the mesopause at about 85 km. Above the mesopause is the thermosphere where the kinetic temperature again increases with height, asymptotically approaching a value in the region of 1500°K to 2000°K, about one thousand kilometres above the earths surface.

Below about 90 km the composition of the atmosphere is essentially the same as that at sea level. This sub region is referred to as the homosphere, where diffusion is slow and atmospheric composition is maintained by turbulent

mixing. Above this level, known as the turbopause, is the heterosphere where turbulence is supressed due to the large mean free paths of atmospheric particles.This region is in diffusive equilibrium and each gas can be regarded as having its own height distribution. The term lower atmosphere is used to refer to the region up to about 10 km, the middle atmosphere for the region between 10 km and 100 km and the upper atmosphere above 100 km.

At large altitudes, where high energy solar radiation is abundant, ionization of atoms and molecules result in the production of positive ions and free electrons which recombine relatively slowly. This ionosphere has a lower limit at about 60 km with a peak in the electron concentration at approximately 250 km. The ionosphere is divided into four main regions. The E region, centred at about 110 km, was first identified in the early days of radio communication. Acting as a mirror, reflections from this level drastically increased the distance over which radio signals could be transmitted. The letter E was used in the 1920's to refer to the electric field of the waves reflected from the layer. Subsequently layers below and above this region were identified as the D region at about 85 km and the F_1 and F_2 regions at 200 km and 250 km respectively. The electron content decreases above 250 km due to the decrease in concentration of ionizable species and has a lower limit at 60 km from the reduction in intensity of the ionizing radiation. The ionosphere shows large temporal fluctuations in height and electron content

depending on solar activity, (Ratcliffe, 1972). A pictorial representation of the earths atmospheric structure with reference to the regions discussed can be seen in figure (1.1.1).

The earth is not only irradiated by electromagnetic radiation from the sun but also by an ionized plasma, mainly of protons and electrons, "blown out" from the solar corona. This solar wind, being ionised, interacts with the outer regions of the earths magnetic field where the particles are guided along the magnetic field. This results in a significant influx of energetic particles into the polar regions of the upper atmosphere where the magnetic field lines converge.

1.2. Airglow.

The excitation, dissociation and ionization of atmospheric species by the absorption of solar radiation and collision with energetic particles, gives rise to a myriad of physico-chemical processes. These can produce spectral emission of light from the near ultra violet through to the infra red. Two main types of atmospheric emissions occur, one being airglow and the other aurora. The auroral phenomena are distinguished from airglow in that they are due to excitation processes arising from the collision of energetic particles, principally from the solar wind. The aurorae are generally much more irregular and intense than airglow and are restricted to high magnetic latitudes where the flux of incident particles is

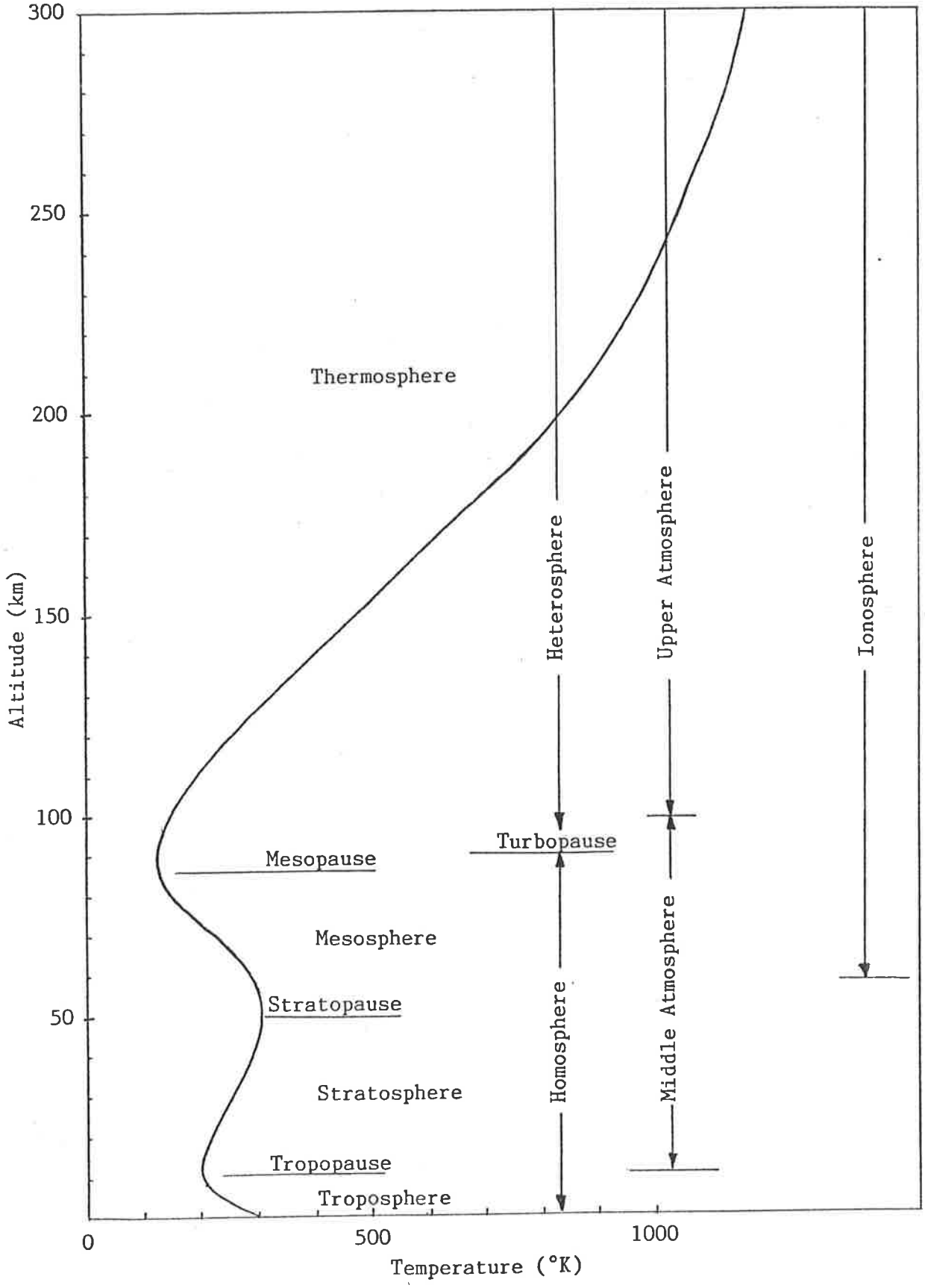

Figure 1.1.1. Mid latitude atmospheric temperature profile indicating regions and nomenclature.

highest. The contribution to atmospheric luminosity from the aurora at mid latitude zenith is very small and will not be pursued further, (Chamberlain and Jacka, 1979). In contrast, the airglow is not restricted to high latitudes, is much less intense and more continuous. The airglow results from chemical reactions among the atmospheric constituents and with sunlight.

Airglow observations are considered in three main types, in accordance with the time of day the measurements are made. Airglow observed during the day and night are referred to as dayglow and nightglow respectively where as ground based measurements made when the sun is below the horizon but still illuminating the upper atmosphere is called twilightglow. Strictly speaking, twilightglow is essentially dayglow measured from the earths night side. Many of the dayglow emissions are visible to a ground based observer, however the intense background radiation of the day sky makes the observation of the dayglow emission difficult, (Hunten, 1967).

Three main mechanisms are responsible for the dayglow: these are fluorescence, resonant scattering of sunlight and photoelectric excitation. During the day energy is stored in photodissociation products of the atmosphere. By night this energy is released by a variety of chemiluminescent processes resulting in the nightglow.

1.3. The λ557.7 nm nightglow.

It is now necessary to discuss in more detail the airglow emission pertinent to this study, namely the green line nightglow emission at λ557.7 nm.The reaction producing the emission is well known, being the electric quadrupole transition of excited atomic oxygen,

$$O(^1S) \xrightarrow{\tau_1} O(^1D) + h\nu_{557.7}$$

with τ_1 the $O(^1S)$ radiative lifetime. However, the exact mechanism for the production of $O(^1S)$ is still under contention, (Slanger and Black, 1977). Chapman (1931a) suggested that the recombination energy of O_2 was available for transfer to an $O(^3P)$ atom enabling it to be excited to the $O(^1S)$ state giving the Chapman mechanism,

$$3O(^3P) \xrightarrow{k_1} O(^1S) + O_2 \qquad (1.3.1.)$$

where k is the rate coefficient for the reaction. This may be followed by quenching of the $O(^1S)$ by mainly $O(^3P)$ and O_2.

$$O(^1S) + O(^3P) \xrightarrow{k_2} O(^1D) + O(^3P) \qquad (1.3.2.)$$

$$O(^1S) + O_2 \xrightarrow{k_3} O(^3P) + O_2 \qquad (1.3.3.)$$

Thirty years later, Barth and Hilderbrandt, (1961) conducted laboratory experiments, the results of which have since been found to be erroneous, showing that the

rate coefficient for the Chapman mechanism is far too low to account for the observed green line emission intensity. They proposed an alternative two step mechanism,

$$2O(^3P) + M \xrightarrow{k_4} O_2^* + M \qquad (1.3.4.)$$

followed by

$$O_2^* + O(^3P) \xrightarrow{k_5} O_2 + O(^1S) \qquad (1.3.5.)$$

where M represents the neutral atmospheric species O, O_2, or N_2. Here the excited oxygen, O_2^* can be quenched by M or $O(^3P)$,

$$O_2^* + M \xrightarrow{k_6} O_2 + M \qquad (1.3.6.)$$

and

$$O_2^* + O(^3P) \xrightarrow{k_7} O_2 + O(^1D \text{ or } ^3P) \qquad (1.3.7.)$$

and O_2^* may undergo radiative deactivation

$$O_2^* \xrightarrow{\tau_2} O_2 + h\nu_{Herzberg} \qquad (1.3.8.)$$

The λ557.7 nm volume emission rates for both mechanisms in photons m^{-3} sec^{-1} are, (Rao et al, 1982).

$$Q_c = \frac{k_1 [O]^3}{1 + \tau_1(k_2[O] + k_3[O_2])} \qquad (1.3.9.)$$

and

$$Q_b = \frac{k_3 k_4 / k_6 [O]^3 [M]}{1+\tau_1(k_2[O]+k_3[O_2])(k_7/k_6[O]+[M]+(\tau_2 k_6)^{-1})} \qquad (1.3.10.)$$

where the square brackets represent the concentration of the species. For clarity the (^{3}P) reference to the oxygen ground state has been disgarded.

Regardless of which mechanism predominates, both equations (1.3.9) and (1.3.10) give similar intensity height distributions. The rate coefficients are weakly temperature dependent and the intensity from either mechanism can be expressed as

$$Q \propto [O]^3 \; T^{\frac{1}{2}} \qquad (1.3.11.)$$

where T is the temperature, (Rao et al, 1982; Tohmatsu and Nagata, 1963; McEwan and Phillips, 1975).

1.4. Height distribution of the λ557.7 nm emission.

Part of the solar radiation incident on the earths atmosphere is absorbed by dissociation and ionization of its constituent gases. At any level, the production rate of dissociation or ionization is proportional to the product of the gas concentration and the intensity of radiation, (Ratcliffe, 1972). At the top of the atmosphere

the production is small since the concentration of gas is small, however, as the radiation penetrates the atmosphere the production rate rises as the concentration increases. Below a certain height, despite an increasing concentration, the intensity of radiation becomes so depleted by previous absorption at higher levels, that the rate of production begins to decrease. Therefore there exists a level where the rate of production reaches a maximum. This maximum is referred to as a production or Chapman layer, its shape depending on the atmospheric gases and the energy of the radiation. Layers of this kind were investigated in a classical paper by Chapman (1931b) who predicted the coincidence of the atomic oxygen production layer with the emitting height of the λ557.7 nm radiation.

Rocket borne experiments such as those conducted by Thomas and Young, (1981); Offerman and Drescher, (1973), show good consistency between the peak altitude of the atomic oxygen and λ 557.7 nm emission profiles. Such a profile comparison can be seen in figure (1.4.1). Further direct experimental data on the emission profiles are reported by Gulledge et al, (1968) and Witt and Stegman, (1979). Theoretical estimates of the peak of the emission profile from both the Chapman and Barth excitation mechanisms show reasonable agreement with experimental observations, (Slanger and Black, 1977; Roa et al, 1982). The consensus of these data which will be adopted herein gives an altitude of the emission peak of 95 km with a half width of approximately 6 km.

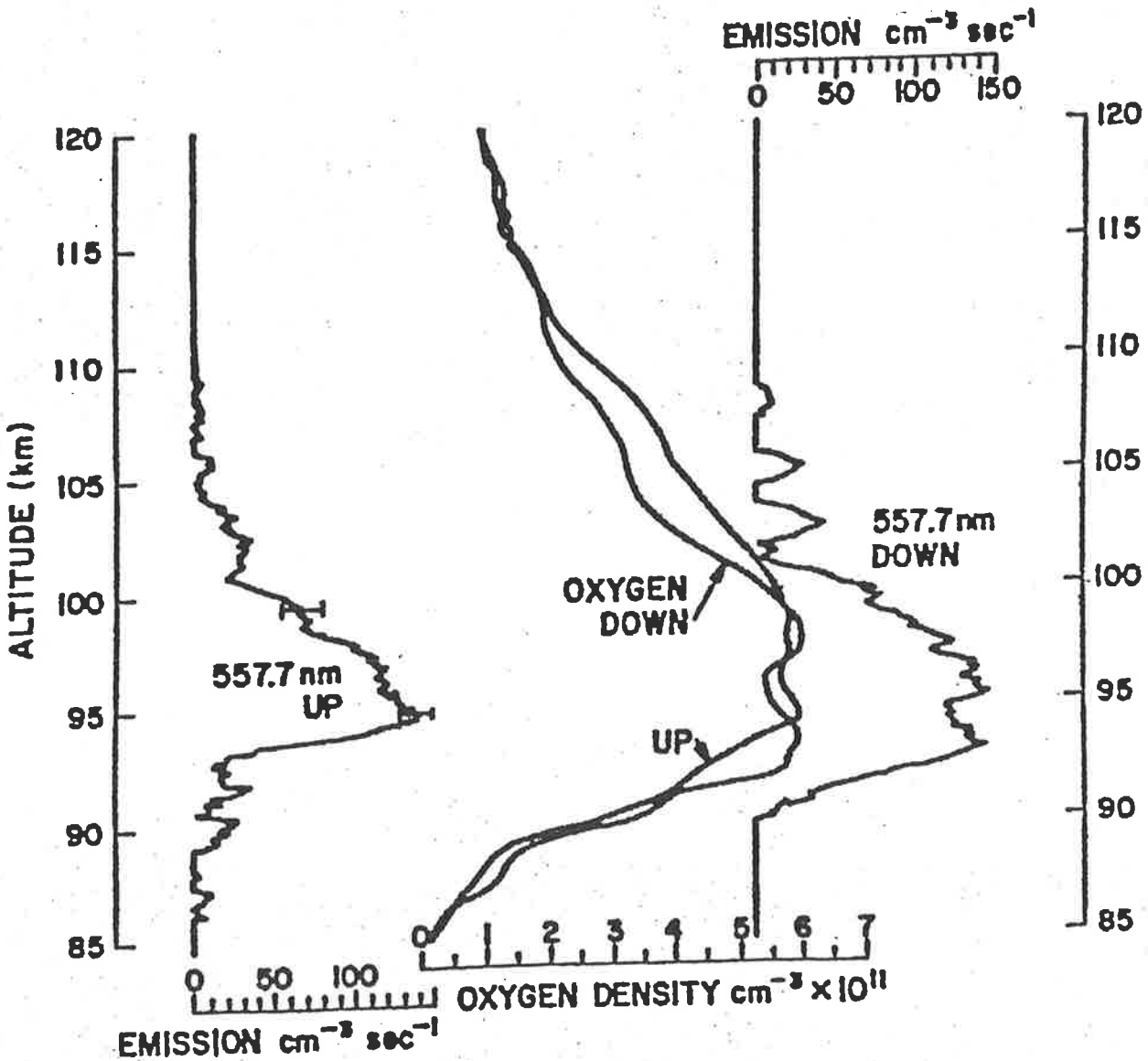

Figure 1.4.1 Oxygen and airglow. From left to right is shown the λ557.7 nm green line on the upleg of the rocket trajectory, the oxygen density on both upleg and downleg and the green line emission on the downleg. Adapted from Thomas and Young, (1981).

It should be noted that a second λ557.7 nm emission peak occurs at about 250 km, due to the dissociative recombination of molecular oxygen ions,

$$O_2^+ + e^- \longrightarrow O(^1S) + O(^1D) \qquad (1.4.1.)$$

The transition of $O(^1S)$ and $O(^1D)$ to the ground state give rise to the upper thermospheric green and λ630 nm red lines. However, the peak of the upper thermospheric green line is much less predominant, with a half width of tens of kilometres and an emission intensity a factor of ten to one hundred times less than that produced at 95 km, (Gulledge et al, 1968). The contribution of this second emission to this study is considered negligable.

Chapter 2. Atmospheric Waves.

2.1. Introduction.

Some of the earliest recorded observations of wave activity in the atmosphere date back to the 1880's, where the effects of waves could be clearly seen in the periodic structure of noctilucent clouds which form near the mesopause at high latitudes. In the early 1920's when radio engineers began using the ionosphere as a reflector to extend the range of radio communication, the problem of periodic fading of the reflected signal soon became apparent. Experiments showed that this fading was caused by moving ripples in the lower ionosphere, focussing and defocussing the radio signal. Martyn (1950) proposed that these disturbances were due to cellular atmospheric standing waves perturbing the ionosphere.

Direct observations of noctilucent clouds and meteor and rocket trails showed small wavelike irregularities superimposed on relatively steady background wind and temperature profiles, (Fogle and Haurwitz, 1966; Lillen and Whipple, 1954). Indirect measurements by radio techniques such as partial reflection, Doppler radar and backscatter radar also revealed similar irregularities in the mesosphere and thermosphere, (Georges 1967; Munro 1958). These irregularities became known as travelling ionospheric disturbances (TID's), exhibiting horizontal wavelengths of hundreds to thousands of kilometres, horizontal phase velocities ranging from tens to hundreds of metres per second and periodicities from minutes to

hours. Hines (1960) developed and modified Martyn's theory of atmospheric cellular waves and convincingly argued that the observation of TID's, originally thought to be due to turbulence, could be explained as manifestations of propagating atmospheric gravity waves. This wave interpretation has been shown to be consistent with TID observations and it is now generally accepted that gravity waves play a major role in upper atmospheric dynamics.

2.2. Acoustic-Gravity waves.

The earths atmosphere is capable of sustaining considerable wave activity. The most familiar are sound waves which are longitudinal compression waves relying on the atmospheric elasticity as the restoring force. The gravitational field of the earth gives rise to an atmospheric density stratification and introduces another restoring force, the buoyancy force. A small vertical displacement of an air parcel from a more dense to a less dense region will result in a gravitational force acting on the parcel, returning it to its original position since it is heavier than the surrounding atmosphere. As a consequence of the parcel's inertia it will overshoot its equilibrium position and be acted on by a buoyancy force resulting in a harmonic oscillation, the frequency of which is known as the Vaisala Brunt frequency N, (Lindzen, 1971; Tolstoy, 1963). Since gravity acts only in the vertical direction, the related wave processes are highly anisotropic in contrast to acoustic waves which exhibit isotropic behaviour.

In order to study the propagation of waves in the atmosphere, the physical properties of the atmosphere must be known. The principal properties are density, pressure, composition, temperature, and motion. These parameters are highly variable in both time and space and it is therefore necessary to introduce simplifing assumptions by means of defining a model atmosphere from which to initiate a mathematical description. The model atmosphere described follows that proposed by Hines, (1960) in so far as it is assumed, in the absence of waves, to be stationary, isothermal and uniform in composition. It is also assumed to be electrically neutral and that waves undergo no dissipation. Although this may appear an oversimplification, the conditions of an isothermal and stationary atmosphere can be relaxed by considering thin isothermal layers in a reference frame moving with the background atmosphere. The effects of wave dissipation will be considered separately in a later discussion.

The Eulerian representation of the equations of motion in this model atmosphere can be written

Equation of continuity:

$$\frac{D\rho}{Dt} + \rho(\underline{\nabla}.\underline{V}) = 0 \qquad (2.2.1.)$$

Equation of force:

$$\rho\frac{D\underline{V}}{Dt} + \underline{\nabla}p - \rho\underline{g} + 2\rho\underline{W}x\underline{V} = 0 \qquad (2.2.2.)$$

Equation of energy:

$$\frac{Dp}{Dt} - C^2\frac{D\rho}{Dt} = 0 \qquad (2.2.3.)$$

where the Eulerian or mobile operator is defined as

$$\frac{D}{Dt} = \frac{\partial}{\partial t} + (\underline{V}.\underline{\nabla})$$

and

$\underline{V}$ - fluid velocity

ρ - atmospheric density

p - atmospheric pressure

$\underline{g}$ - gravitational accelaration

C - velocity of sound

$\underline{W}$ - angular velocity of the earth

The effect of the earths rotation is two fold. Since the atmosphere rotates with the earth then there exists a centrifugal acceleration, the effects of which can be incorporated into that of gravity. The second is the Coriolis psuedo force which acts perpendicular to the direction of air flow and earths rotation. This apparent deflecting force (per unit mass) appears in equation (2.2.2) as $2\underline{W}x\underline{V}$.

A further assumption in the development of gravity wave theory is that pertubations of the atmospheric parameters due to a gravity wave are small; at any given time these parameters can be represented as $\rho = \rho_o + \rho'$; $T=T_o+ T'$, $p=p_o+ p'$, and $V=V'$, since V_o is assumed zero.

Products of the primed quantities are considered negligable and substitution into equation (2.2.1.), (2.2.2.) and (2.2.3.) give the linearized equations of motion.

Wave solutions to these equations can be found in complex form such that

$$p'/p_o P = \rho'/\rho_o R = V_h/X = V_z/Z \propto \exp i(\omega t - k_h x - k_z z) \quad (2.2.4.)$$

where P,R,X and Z are referred to as the polarization constants, (Hines, 1960), k_h and k_z are the horizontal and vertical complex wavenumbers and ω the angular frequency of the wave. By coordinate rotation about the z axis, wave propagation is chosen to have zero y component. The dispersion equation relating the horizontal and vertical wave numbers is then

$$k_z^2 = k_h^2 \, (N^2 - \omega^2)/(\omega^2 - f^2) - (N_A^2 - \omega^2)/C^2 \quad (2.2.5.)$$

where the Vaisala Brunt frequency $N = (\gamma-1)^{\frac{1}{2}} g/C$ (2.2.6.)

the acoustic cut off frequency $N_A = \gamma g/2C$ (2.2.7.)

and the inertial frequency $f = 4\pi \sin \phi/T$ (2.2.8.)

Here γ is the ratio of specific heats, T the earths rotation period and ϕ the latitude, (Gossard and Hooke, 1975).

Since this study deals with vertical propagating internal waves, the wave vectors k_h and k_z are considered to be purely real. A purely imaginary k_z implies an evanescent

wave, that is a wave which decays exponentially with height being supported by some boundary or interface. These waves will receive no further consideration. Rewriting equation (2.2.5) with $k_h = \omega/V$, where V is the horizontal phase velocity of the wave, for $k_z^2 > 0$ then,

$$\frac{N^2 - \omega^2}{\omega^2 - f^2} > \frac{V^2}{\omega C^2}(N_A^2 - \omega^2) \qquad (2.2.9.)$$

for waves to propagate vertically. From equation (2.2.6) and (2.2.7), $N_A^2 > N^2$ since γ is necessarily less than 2. Because N_A, N, ω, and f are all real and positive then it is apparent that for $\omega^2 < f^2$ the condition of equation (2.2.9) can not be met, implying that gravity waves can not propagate vertically with frequencies less than the inertial frequency. For the region where $f^2 < \omega^2 < N^2$ vertical propagation is allowed provided $V < C$. This is referred to as the gravity wave branch and is the principal region of concern. This region covers a frequency range corresponding to periods from 20.9 hours, being the inertial period at 35 degrees latitude, down to the Vaisala Brunt cut off period which, depending on altitude, may vary between 5 and 15 minutes.

Another region where no internal waves can propagate lies between the Vaisala Brunt and acoustic cut off frequencies. For $N^2 < \omega^2 < N_A^2$ equation (2.2.9) has no solution. For frequencies greater than the acoustic cut off frequency, $\omega^2 > N_A^2$ another domain exists called the acoustic branch where $V > C$. Here the effects of gravity can be neglected and wave propagation is isotropic and non dispersive.

2.3. Energy propagation and dissipation.

In a real atmosphere monochromatic waves do not generally exist; but rather as a collection of waves of approximately the same frequency. These waves interfere to form a wave packet or group which travel with a group velocity V_g, different from the phase velocity. The energy associated with the packet travels with the same velocity as the wave group, (Yeh and Liu, 1974).

The variation of group velocity can best be seen using a dispersion diagram which is a pictorial representation of the dispersion relation (2.2.5). This can be rewritten in the form of a general conic, i.e.

$$\frac{k_h^2}{a^2} + \frac{k_z^2}{b^2} = 1 \qquad (2.3.1.)$$

where

$$a^2 = \frac{(N_A^2 - \omega^2)(\omega^2 - f^2)}{C^2(N^2 - \omega^2)} \qquad (2.3.2.)$$

and

$$b^2 = (N_A^2 - \omega^2)/C^2 \qquad (2.3.3.)$$

Remembering that $N_A^2 > N^2$ then for the case of gravity waves with $f^2 < \omega^2 < N^2$ both a^2 and b^2 are positive, therefore equation (2.3.1) represents a family of hyperbolae with different frequencies. For acoustic waves, $\omega^2 > N_A^2$ so b^2 is negative, resulting in a family of ellipses.

A wave with propagation vector $|\underline{k}| = (k_h^2 + k_z^2)^{\frac{1}{2}}$ has horizontal and vertical components of the group velocity given by

$$V_{gh} = \left(\frac{\partial \omega}{\partial k_h}\right) k_z \qquad (2.3.4a.)$$

and

$$V_{gz} = \left(\frac{\partial \omega}{\partial k_z}\right) k_h \qquad (2.3.4b.)$$

Figure (2.3.1) shows the dispersion curves for the gravity and acoustic wave modes in the positive k_h and k_z quadrants. Also shown are wave propagation vectors $\underline{k}$, each with phase elevation angles θ_a and θ_g from the horizontal. The direction of the group velocity vector at the point of contact of $\underline{k}$ with any give ω contour is derived from equations (2.3.4a,b) to be

$$\frac{V_{gz}}{V_{gh}} = -\left(\frac{\partial k_h}{\partial k_z}\right)_{\omega} \qquad (2.3.5.)$$

which is normal to the ω contour. Therefore the direction of the group velocity, hence energy propagation, is given by the outward normal to the ω contour at the point of intersection with the phase velocity vector, (Hines, 1960).

From this pictorial representation it is easy to see that for the case of acoustic waves, the direction of energy propagation is almost collinear with that of phase propagation, with both able to propagate in any direction.

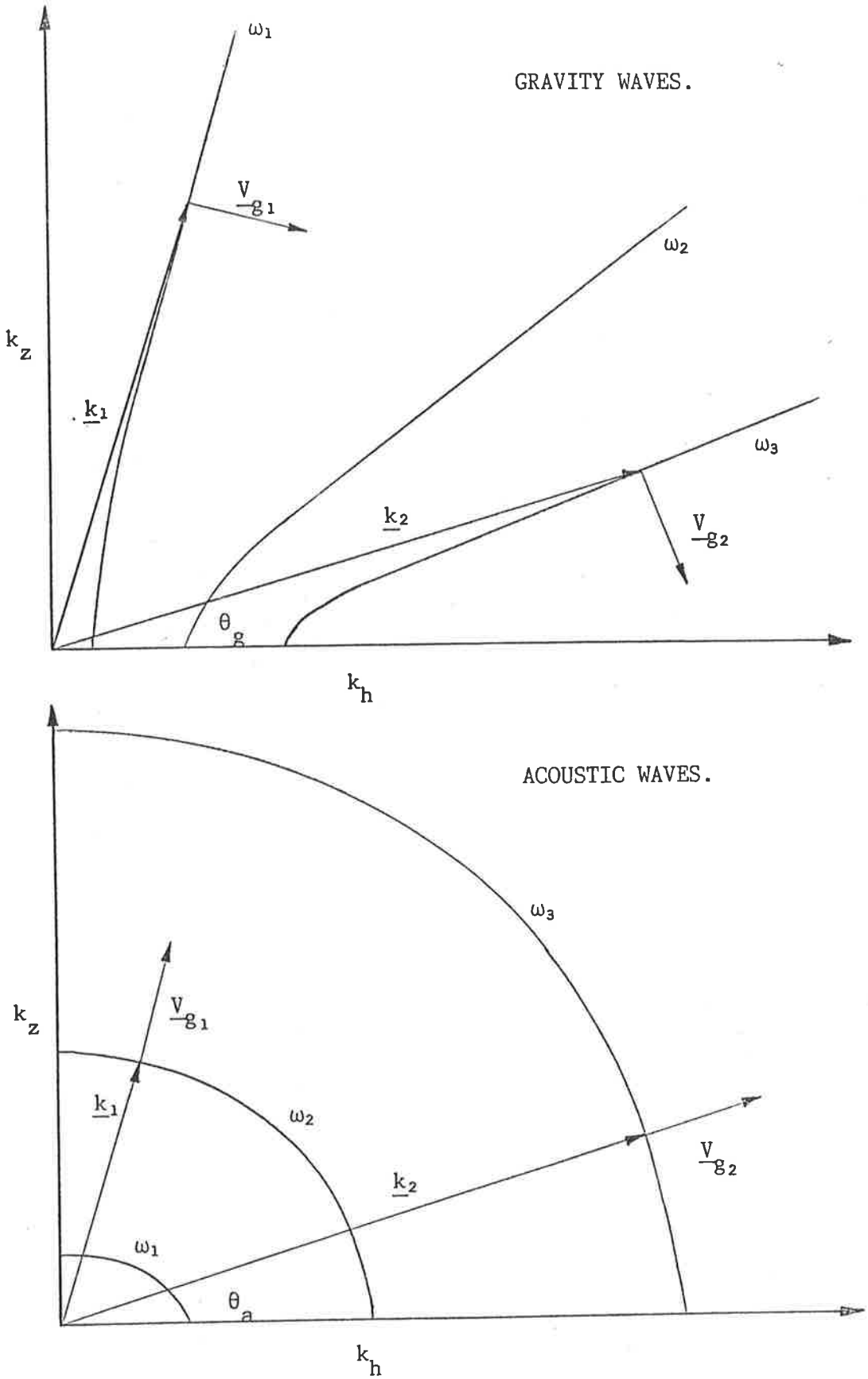

Figure 2.3.1. Dispersion curves for selected gravity and acoustic waves with $\omega_1<\omega_2<\omega_3$. Note the high anisotropy of the gravity wave modes. An upper limit exists for θ_g, where θ_a can take any value. The diagram also illustrates the relation between the phase and group velocities at different frequencies for the two modes.

For gravity waves, depending on the magnitude of the vertical wave vector, the direction of propagation of phase and energy can be up to 90 degrees apart. Due to the fixed direction of the restoring force, gravity waves are highly anisotropic which is apparent from the diagram. For a given frequency there is a maximum angle for phase propagation, given by the slope of the asymptote for that frequency. In general, as $\omega \longrightarrow N$, phase tends to propagate horizontally whereas energy propagates vertically and for $\omega \longrightarrow f$, phase propagates vertically and energy horizontally. It should be noted that the vertical components of phase and energy propagation are in opposite directions, an upward transfer of energy is associated with a downward phase progression and visa versa.

As will be seen later, the majority of waves detected in the upper atmosphere are likely to originate from the more energetic lower atmosphere. Because of the exponential density distribution of the atmosphere, waves generated in the troposphere will grow exponentially in amplitude as they propagate upward as a consequence of energy conservation. Since the neutral density at say 95 km is about six orders of magnitude less than the troposphere, then waves generated in this region need only minute amplitudes in order to significantly influence the upper atmospheric regions.

It is the dissipative effect of the atmosphere on internal wave energy which results in the deposition of the wave energy to the background atmosphere. The effects

of dissipation on upward propagating waves gives rise to a significant energy transfer mechanism from the lower to the upper atmosphere. It has been suggested, (Hines, 1963) that this mechanism may be responsible for the high temperatures observed in the winter time mesosphere.

The three main dissipating processes which convert wave energy to heat are ion drag, viscosity and thermal conduction. Ohmic loss or ion drag occurs when neutral particles, displaced by the motion of the wave, collide with the charged particles of the ionosphere. The effect of the earths magnetic field is to restrict the motion of these charged particles to follow magnetic field lines. Therefore, any wave induced displacement with a component perpendicular to the magnetic field lines will result in energy dissipation in the form of heat. The overall effect is to filter out those waves whose wave fronts are not field aligned. Ion drag only becomes an important dissipative process at altitudes greater than about 100 km since at these heights ionization is truely restricted to move along field lines. At heights between about 60 km and 100 km, ionization is still present but the collision frequency is high and the effect of the earths magnetic field on the motion of charged particles is small. Here in the lower ionosphere the ionization tends to follow the neutral motion.

The effect of viscosity is to randomize the wave motion through particle collisions. Small scale atmospheric turbulence also acts in a similar fashion to

molecular viscosity and is referred to as eddy viscosity which is only important below the turbopause. Energy dissipation due to thermal conductivity arises from the transfer of heat from the compressed to the cooler parts of the wave, that is the parcel motion is no longer adiabatic. Thermal conductivity acts in a similar manner to viscosity and the two dissipative effects can be combined to form the effective viscosity, (Pitteway and Hines, 1963). The result of both dissipative processes is to degrade the organized motions of the individual particles.

The effective viscosity transfers energy from a propagating wave to the background atmosphere in the form of heat, with the smaller scale wave modes being the most severly affected.

2.4. Critical levels.

The condition of a stationary atmosphere can now be relaxed and a background wind vector introduced, $\underline{U}=(U_x,U_y,U_z)$, which is constant in space and time. Consider the wave motion relative to a reference frame moving with the background wind. Recalling the Eulerian operator,

$$\frac{D}{Dt} = \frac{\partial}{\partial t} + U_x\frac{\partial}{\partial x} + U_y\frac{\partial}{\partial y} + U_z\frac{\partial}{\partial z} \qquad (2.4.1.)$$

then if the wave pertubation is expressed as

$$\exp i(\omega t - k_x x - k_y y - k_z z)$$

where ω and $\underline{k}$ are measured in the fixed frame then

$$\frac{D}{Dt} = i\omega - iU_x k_x - iU_y k_y - iU_z k_z$$

$$= i\Omega$$

where $\Omega = \omega - \underline{U}.\underline{k}$ (2.4.2.)

Here Ω is the Doppler shifted frequency, being the wave frequency seen in the moving frame, often called the intrinsic frequency. The dispersion equation (2.2.5) for a non stationary atmosphere can be written simply by replacing the wave frequency with the intrinsic frequency,

$$k_z^2 = k_h^2 (N^2-\Omega^2)/(\Omega^2-f^2) - (N_A^2-\Omega^2)/C^2 \qquad (2.4.3.)$$

Since $\omega = \Omega + \underline{U}.\underline{k}$, the wave group velocities can be written

$$V_{gx} = (\partial\omega/\partial k_x) = (\partial\Omega/\partial k_x) + U_x \qquad (2.4.4a.)$$

$$V_{gy} = (\partial\omega/\partial k_y) = (\partial\Omega/\partial k_y) + U_y \qquad (2.4.4b.)$$

$$V_{gz} = (\partial\omega/\partial k_z) = (\partial\Omega/\partial k_z) + U_z \qquad (2.4.4c.)$$

Hence, as observed from a fixed reference frame, the components of the group velocities are simply the sum of

the group velocity in the moving frame and the background wind. Therefore, energy propagation of the wave packet is advected along by the background flow in addition to its own group velocity relative to the moving system.

In general the vertical component of the background flow, U_z, can be considered negligable compared with the horizontal component, therefore equation (2.4.2) can be written,

$$\Omega = \omega - U_x k_x \qquad (2.4.5.)$$

From the above equation, if the horizontal phase velocity is equal to the background flow then the intrinsic frequency vanishes. This criterion defines a critical layer where coupling between the wave and the wind takes place. Here the wave frequency is Doppler shifted to zero and the wave energy and momentum is transferred to the background wind, (Hines and Reddy, 1967; Booker and Bretherton, 1967).

Reflection of the wave occurs where $k_z^2 < 0$, (Pitteway and Hines, 1965). For the case of medium scale gravity waves where the earths rotation can be neglected, waves are reflected when $\Omega \longrightarrow N$ and when the horizontal phase velocity, $\Omega/k_h \longrightarrow NC/N_A$. The first condition may occur when waves propagate antiparallel to strong background winds and are Doppler shifted to higher frequencies. The latter condition, unrelated to the wind field, limits the horizontal phase speed of the wave. In a

non isothermal atmosphere, the height profile of NC/N_A gives rise to reflection levels in the atmosphere for waves with high phase velocities. This will be discussed in greater detail later.

Levels of reflection and critical coupling are brought about by the Doppler shifting of the wave frequency by the mean flow. For an isotropic wave field, originating low in the atmosphere and propagating to higher altitudes, the middle atmospheric wind field can act as a directional filter, allowing waves of only certain azimuths to reach the upper atmosphere, effectively polarizing the wave field, (Cowling et al, 1971; Yeh et al, 1972; Waldock and Jones, 1984).

2.5. The effects of gravity waves on the λ557.7 nm airglow emission.

As a gravity wave propagates through the atmosphere it perturbes the local atmospheric density and temperature, therefore affecting the atmospheric photochemistry by altering the reaction rates and concentrations of the atmospheric species, (Frederick, 1979).Equation (1.3.11) shows that the intensity of the λ557.7 nm emission is strongly influenced by the atomic oxygen concentration and only weakly dependent on temperature. For this reason the effect of a temperature pertubation on the intensity of the emission through the reaction rates of the emission mechanisms is small and fluctuations in the λ557.7 mn emission brought about by the passage of a gravity wave

will be considered entirely due to pertubations in the atomic oxygen concentration.

By observing relative fluctuations in the amplitude of the emission, the relative amplitude of the atmospheric density oscillations caused by a gravity wave may be inferred.

For the model atmosphere described in §2.2 and if diffusive equilibrium can be assumed then the density of each atmospheric constituent decreases with altitude as $\exp(-z/H_c)$, where H_c is the scale height of constituent c. If diffusive separation resulting from the wave motion itself can be neglected, that is the time scale for the wave oscillation is much less than the diffusion times of the individual species, (Dudis and Reber, 1976; Molina, 1983) and since the photochemical lifetime of the oxygen perturbation is long compared to the wave period, (Tohmatsu and Nagata, 1963), then

$$(\Delta\rho_o/\rho_o) = (\Delta\rho/\rho)(\gamma H-H_o)/((\gamma-1)H_o) \qquad (2.5.1.)$$

where ρ_o and ρ are the mean densities of atomic oxygen and the background atmosphere respectively, H_o the scale height of atomic oxygen and Δ indicates fluctuations in the parameter. Now

$$-1/H_o = (1/[O])/(\partial[O]/\partial z) \qquad (2.5.2.)$$

and

$$\Delta\rho_o/\rho_o = \Delta[O]/[O] \qquad (2.5.3.)$$

Rearranging equation (2.5.1.) gives

$$\frac{\Delta[O]}{[O]} = \frac{1 + (\gamma H/[O])(\partial[O]/\partial z)}{(1-\gamma)} \frac{\Delta\rho}{\rho} = \frac{\alpha\Delta\rho}{\rho} \qquad (2.5.4.)$$

which relates the relative fluctuations in the atomic oxygen concentration to that of the background atmospheric density. This expression, obtained by Weinstock, (1978) by means of different considerations, also holds if diffusive equilibrium is not assumed.

To relate $\Delta Q/Q$ to $\Delta[O]/[O]$, the question of the emission mechanism arises. For the Chapman mechanism, recalling equation (1.3.9)

$$\frac{\Delta Q}{\Delta[O]} = \frac{3k_1[O]^2}{1+\tau_1(k_2[O]+k_3[O_2])} - \frac{k_1k_2\tau_1[O]^3}{(1+\tau_1(k_2[O]+k_3[O_2]))^2}$$

$$= \frac{3Q}{[O]} - \frac{Qk_2\tau_1}{1+\tau_1(k_2[O]+k_3[O_2])}$$

giving

$$\frac{\Delta Q}{Q} = \left[3 - \frac{k_2\tau_1[O]}{1+\tau_1(k_2[O]+k_3[O_2])}\right] \frac{\Delta[O]}{[O]} \qquad (2.5.5.)$$

Using the rate coefficients of Slanger and Black, (1977) and the atomic and molecular oxygen concentrations at the peak of the emission layer from Battaner, (1975) then

$$\Delta Q/Q = 2.1\ \Delta[O]/[O] \qquad (2.5.6.)$$

Similarly for the Barth mechanism

$$\Delta Q/Q = 1.9\ \Delta[O]/[O] \qquad (2.5.7.)$$

Here the exact shape of the emission profile is unimportant provided that the [O], [O_2] and the reaction rates do not change very much within the emission layer. Combining equations (2.5.4) and (2.5.6,7) gives a relation between the relative intensity fluctuations of the green line emission and the background atmospheric density due to the passage of a gravity wave

$$\Delta\rho/\rho = (1/2.1\alpha)\Delta Q/Q \qquad (2.5.8.)$$

for the Chapman mechanism and,

$$\Delta\rho/\rho = (1/1.9\alpha)\Delta Q/Q \qquad (2.5.9.)$$

for the Barth mechanism.

The value of α depends on the relative height distribution of the emission and atomic oxygen profiles. Since the observation of intensity fluctuations comes from a narrow emission layer, then the values defining α in equation (2.5.4) will depend on where this layer is situated in relation to the atomic oxygen profile.

Three cases are considered. The first is for the emission maximum occuring above the atomic oxygen peak, as suggested by the observations of Offerman and Drescher (1973). The second is where the emission and atomic oxygen peaks are coincident, reported from the measurements made by Thomas et al (1981) and finally where the emission peak occurs on the underside of the atomic oxygen maximum. This final hypothesis, put forward by Rao et al, (1982), uses modelled atomic oxygen profiles and theoretically determines the height differences between the atomic oxygen and emission peaks for both the Chapman and Barth mechanisms. The results of Rao et al, (1982) show that the peaks are essentially the same height for the Chapman mechanism but are displaced, with the emission peak being up to 3.6 km lower than the atomic oxygen maximum, if the Barth mechanism is assumed.

The values of H, [O] and $\partial[O]/\partial z$ which specify α in equation (2.5.4) have been averaged over the emission layer and are summarized for the three hypotheses in the following table

Hypothesis	α	$\Delta\rho/\rho = \beta\Delta Q/Q$	
$Q_{zm} > [O]_{zm}$	-0.6	$\beta = 0.8$	C
		$= 0.9$	B
$Q_{zm} = [O]_{zm}$	-1.3	$= 0.4$	C
		$= 0.4$	B
$Q_{zm} < [O]_{zm}$	-0.4	$= 1.3$	B

Table 2.5.1.

Where C and B refer to the Chapman and Barth mechanisms respectively, Q_{zm} and $[O]_{zm}$ being the altitude of the peaks in the emission and the atomic oxygen height profiles.The fact that $\alpha<0$ indicate that the variations in the density are out of phase with those of atomic oxygen concentration, (Weinstock, 1978; Battaner and Molina, 1980).

The significance of the relation between relative intensity fluctuations in the green emission to those of the atmospheric density will become apparent later when estimates of gravity wave energy densities are derived from observations of the λ557.7nm nightglow intensity.

Chapter 3. The three field photometer.

3.1. Introduction.

Fluctuations in the intensity of up to six different nightglow emissions from three separate regions of the sky can be simultaneously measured by a photometer to be described. The instrument is essentially three individual photometers sharing the same objective optics. A motor driven wheel with positions for six interference filters can be remotely controlled, allowing the filters to be cyclically placed into each of the three fields. The three field photometer (3FP) is of novel design and highly flexible in as much as many different nightglow emissions can be studied, either for comparison or individually.

The first photometer was constructed in 1980. This instrument was installed and made operational at Mawson base, Antarctica (67°S, 62°E), in 1981. During this time a second identical instrument was constructed, and in late 1982 was commissioned at Mt. Torrens (34°S, 138°E), near Adelaide. A total of 55 nights of data were recorded at Mawson; however, none of these data were suitable for analysis due to the overwhelming noise from the λ557.7 nm auroral emission. Although it was obvious the aurora would be present, it was expected that there would be times when the auroral oval was well enough removed from Mawson to allow the nightglow emission to predominate. This was not the case, and, being a time of solar maximum, the zenith aurora was rarely negligable for any significant interval.

This thesis will therefore deal exclusively with results from data later obtained from the Mt. Torrens instrument.

3.2. Optics.

The photometer optics are schematically shown in figure (3.2.1). The objective lens, L_1, forms the entrance pupil to the system and is the only part of the instrument exposed to the outside environment. A glass window, mounted on an electrically heated metal cylinder, is positioned below it to contain and warm the air, preventing water vapour from inside the laboratory from condensing on the lens.

A second lens, L_2, positioned a distance l_2 (the back focal length of lens L_2) below the objective, focusses a cone of light onto the image plane such that the axis of the cone is parallel to the central axis of the instrument, that is perpendicular to the image plane. This then describes a telecentric optical system, that is, the axis of the light cone subtended at the image plane is always perpendicular to the image plane for all three fields.

The fields of the photometer are defined by three field stops in the image plane which are separated by angles of 120 degrees. If the distance to the centre of the field stop from the central axis is b then the off zenith angle to the centre of each field is given by,

$$\theta = \arctan(b/l_2) \qquad (3.2.1.)$$

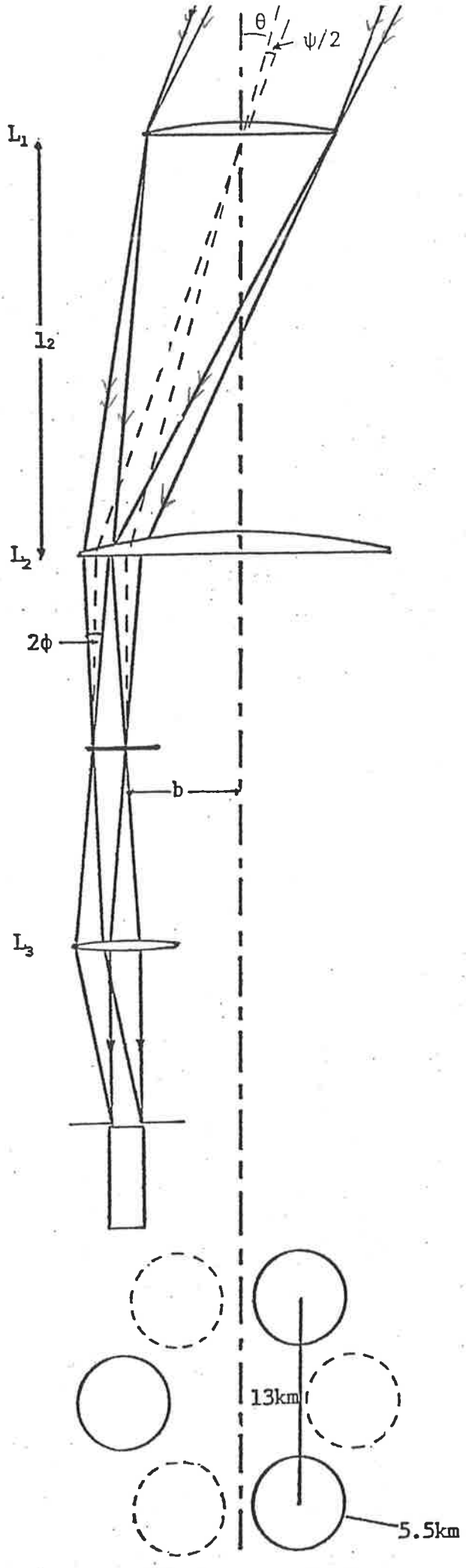

Objective lens and entrance pupil.

Telecentric lens focuses a cone of light with axis perpendicular to the filter plane.

Plane of the filter wheel which carries up to 6 different filters. Filter holders allow tilting of interference filters for fine tuning.

Collimating lens.

Exit pupil.

Photomultiplier. EMI 9658

Plan view of the three fields. The solid circles show the relative positions of the three filters over the photo-multipliers while the dashed circles are 'hidden' filters which can be brought into view by a 60° rotation of the filter wheel.

The dimensions refer to the fields of view at 95 km.

Figure 3.2.1. Photometer optics.

The angular field of view of each field, ψ, is defined by the diameter of the field stop, d such that

$$\psi = 2(\arctan[(2b+d)/2l_2] - \theta) \qquad (3.2.2.)$$

the shape of the field stops, hence the fields of view being circular. From the dimensions of the instrument and using field stops of 48mm diameter then θ =5.2 degrees and ψ =3.3 degrees.
Projecting to the 95 km level gives each field a diameter of 5.5 km, centred at the apexes of an equilateral triangle and separated by a distance of 13 km.

A wheel lies in the focal plane of the instrument with positions for six field stops. This wheel can be motor driven in increments of 60 degrees allowing each stop to be cyclically placed into each field. The field stops used here are interference filters which not only define the size of the field but also the wavelength of light detected.

Immediately below the filter wheel is an electrically operated rotary solenoid which, whenever deactivated, optically isolates the detector system. Divergent light from the filters pass through the open shutter and is collimated onto the exit pupils which lie on the photocathodes of the photomultiplier detectors.

Lenses L_2 and L_3 have antireflection coatings so, discounting the interference filters, losses due to Fresnel reflection from all of the optical components is approximately 20%.

3.3. Detectors.

The three photomultiplier detectors are EMI type 9658B with S20 photocathodes deposited on a prismatic window. The spectral response of the photocathode peaks at around λ430 nm and declines, almost linearly, to a cut off at about λ900 nm. The quantum efficiency, $q(\lambda)$, of a photocathode at a given wavelength is defined as the number of photoelectrons emitted from the photocathode per incident photon, usually expressed as a percentage. If the photocathode material is deposited on the underside of a plane window, photons passing through the window may be reflected from the glass-photocathode interface and lost. The effect of a prismatic window is to totally internally reflect these photons, enabling them to be incident on the photocathode more than once, thereby increasing the overall quantum efficiency, (Oke and Schild, 1968). Below is the quantum efficiency for selected wavelengths taken from the EMI specification.

9658B	λ(nm)	q(λ) %
	430	25
	500	19
	530	17
	558	15
	630	10

Table (3.3.1)

Since the photomultipliers are used in a low light level application, a pulse counting detection technique is used. To reduce the dark count level generated by

thermionic emission at the photocathode, the photomultipliers are cooled. For the S20 photocathode the dark count rate can be reduced by two orders of magnitude by cooling to about -20°C, (Harkin et al, 1969; Davies, 1972). This is achieved by sealing the photomultipliers in a stainless steel cooling chamber through which is pumped a methanol water coolant from a remote refrigeration plant. The system gives operating temperatures typically of -25°C. To prevent condensation of water on the photocathodes, three thermal windows, consisting of dry nitrogen filled perspex cells, are sealed above the photocathodes.

Each photomultiplier has its own variable power supply. Prior to installation, each photomultiplier was tested under cooled conditions with a constant low level light source. Individual tube characteristics were assesed and supply voltages chosen such that each tube was operated at its optimum signal to noise ratio and high gain, (Jonas and Alon, 1971).

High speed pulse amplifiers are connected to the anodes of each photomultiplier with a low level discriminator distinguishing, to some extent, photon induced counts from lower level background noise. The pulse width is then standardized with a monostable to 20 ns to comply with the minimum pulse width detectable by the counting circuitry. The pulse amplifier-discriminators have frequency responses of approximately 20 MHz, and are mounted in three separate metal boxes directly below the

photomultiplier cooling unit. The entire instrument, with associated electronics, is housed in a light proof metal cabinet with removable doors for access to the filter wheel assembly and electronics. A cross sectional view of the photometer, showing component layout can be seen in figure (3.3.1)

3.4. Filters.

In order to select regions of the nightglow for analysis, narrow bandpass interference filters were used as field stops in the focal plane of the photometer. These interference filters are essentially Fabry-Perot etalons with a solid dielectric spacer an intergral number of half wavelengths thick at the desired transmitting wavelength. Either side of the spacer are dielectric stacks consisting of alternating high and low refractive index quarter wave layers. The bandpass and bandwidth of these filters are specified using collimated light normally incident to the filter. If incident light is at a small angle to the filter, the bandpass is shifted to shorter wavelengths and the bandwidth broadened. The displacement of the bandpass when a filter is in a convergent beam of semi angle ϕ is one half of the displacement when the filter is in a collimated beam incident at an angle ϕ to the normal, (Eather and Reasoner, 1969).

The semi angle of convergence of incident light on the filters is given by

$$\phi = \arctan (D_1/2l_2) \qquad (3.4.1.)$$

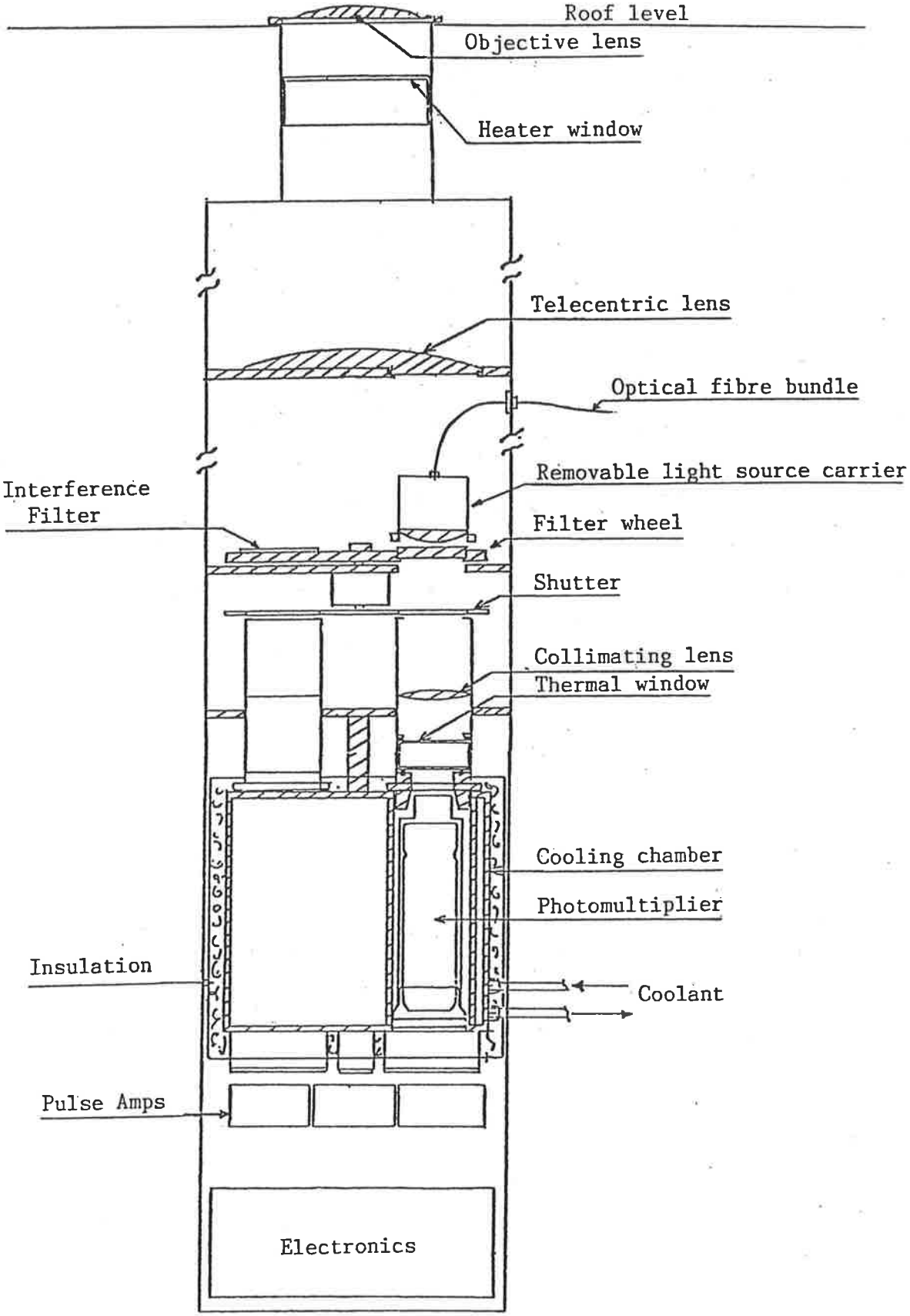

Figure 3.3.1. Cross section of photometer showing component layout.

where D_1 is the aperature diameter of the objective lens. This was taken into account when specifying filters for the photometer. Other factors affecting the bandpass of interference filters are age, temperature and their moisture resistance, (Blifford, 1966). In order to fine tune the filters, allowance was made to tilt them in their holders.

All filter calibrations were performed with the filters located in the photometer. For this in situ technique, the objective lens was covered and a removable calibration light source carrier introduced directly above the filter as illustrated in Figure (3.3.1.). A fibre optic bundle, spread into a linear array was fixed in front of the exit slit of a grating monochromator; the fibre bundle was then passed through a light tight feed through in the photometer cabinet to the light source carrier. The fibres terminate at the focal point of a plano convex lens, the surface of which is unpolished to diffuse the light. The field of view and aperature are now defined by the filter and exit pupil diameters; light from the carrier is thus equivalent to a diffuse monochromatic source from the sky. This method has the distinct advantage of calibrating the filters in identical conditions to normal photometer operation.

Using a white light source with the necessary blocking filters, the monochromator was scanned and the photometer data logging system used to record filter tranmission characteristics. The filters used and their specifications

are tabulated below. The λ530 nm and λ500 nm filters were used to measure the nightglow continuum in the region of the λ557.7 nm emission. The λ435 nm filter was employed to determine observing conditions by measuring the λ435.8 nm mercury emission from city street lights, scattered by atmospheric haze or cloud.

Filter	bandpass (nm)	bandwidth (FWHM) (nm)
558	557.8	0.8
530	530	4
500	496	1
435	435.8	1.6

Table (3.4.1)

3.5. Expected signal and scaling.

The basic unit for measuring airglow intensity is the Rayleigh, R, named after the fourth Lord Rayleigh who made the first measurements of the absolute intensity of the nightglow. Airglow has an apparent surface brightness or intensity, but the emission is from a volume of excited gas along the line of sight of the observer. The output of an emitting column with a cross section of one square centimetre and assuming isotropic emission with no scattering or absorption may be expressed by

$$I = \int_0^\infty Q(r)\, dr \qquad (3.5.1.)$$

where Q(r) is the volumetric emission rate for a given wavelength a distance r from the observer in megaphotons $cm^{-3} sec^{-1}$. The airglow intensity is then I Rayleighs. That is one Rayleigh is the "surface" emission or intensity of $10^6 / 4\pi$ photons $cm^{-2} sr^{-1} s^{-1}$.

The number of photons entering the photometer with entrance pupil area A and field of view ω steradians is therefore

$$A\omega \; I/(4\pi x \; 10^{-6}) \text{photons sec}^{-1} \qquad (3.5.2.)$$

If photometer optic losses are assumed to be 20% and filter transmittance and photomultiplier quantum efficiency are given by $T(\lambda)$ and $q(\lambda)$ respectively then the count rate is,

$$P = \frac{0.8 \; q(\lambda) \; T(\lambda) \; A\omega \; Ix10^6}{4\pi} \qquad (3.5.3.)$$

The intensity of the λ557.7 nm nightglow is typically 250R (Chamberlain, 1961), therefore, from photometer and filter specifications given earlier, the expected count rate from the λ557.7 nm emission gives $P \simeq 600$ KHz.

As stated, the filter wheel is rotated in steps, pausing in each position. The total time for the filter wheel to rotate one full revolution is 30 seconds, this then gives the sampling time for any one filter in a given field. For gravity waves, the Vaisala Brunt cut off frequency determines the lower limit and at 95 km this

corresponds to a period of about 5 minutes. This is well above the minimum measurable period by the photometer of one minute, given by the Nyquist sampling condition.

For reliable filter wheel movement, this sampling rate gives an acquisition time of 3.6 seconds in each field with a travel time of 1.4 seconds between fields. This gives the average counts per sampling interval of 2.2×10^6 counts.

The λ557.7 nm airglow emits isotropically over a large region and because the photometer samples only a small fraction of this region then the measured counts per time interval will have a Poisson distribution with a variance equalling the mean. This gives an expected standard deviation of $\simeq 1480$. Scaling of the counts is necessary since 16 bit counters are used and, for greater flexibility, a manually selectable scaling range from 32 to 2048 in powers of 2 is used. In order to reduce scaling errors, scale factors much less than the standard deviation were used, but not so small as to overflow the counters during an enhancement of the nightglow. Scaling factors for the other filters were similarly selected.

3.6. Photometer control.

The photometer has been designed to operate automatically with control of the instrument and data logging directed by a CBM micro computer. Photometer functions controlled by the computer are; filter wheel position, shutter and photomultiplier power supplies.

These are controlled by an eight bit control word which may be overridden to allow for manual operation via front panel controls. Photometer status is read by the computer by two eight bit status words containing information on the filter wheel position, shutter status and the preset scaling factors for each filter. The status word also contains an overlight bit, activated from a light sensitive detector located below the objective lens. This safeguard offers protection to the photomultipliers by closing the shutter and turning off the power supplies if the light level approaches a predetermined upper limit, typically that of a full moon at zenith. Another safeguard is a lock out timer which cuts power to the photometer and microcomputer once a set time has been reached, also preventing a cold start after a power failure.

Communication between photometer and computer is serial via parallel-serial converters. Scaled counts from each field are transmitted along three separate lines to counters interfaced to the computer. All lines in and out of the photometer are optically isolated to reduce any electrical interference.

Acquisition timing is controlled by the computer's internal clock, giving a time jitter error of less than 1% at the maximum counting frequency. Prior to an observation run, start and stop times are entered via the keyboard and after setting the photometer to automatic mode the system can be left to operate unattended. After reaching the start time the computer will begin to step the filter

wheel and record data while continually checking photometer status and the overlight condition. After the stop time has been exceeded the system will automatically close down.

Scaled counts and scaling factors which are read from the photometer are recorded on floppy disk. Every thirty seconds a total of 18 numbers, up to eight digits each, are outputted from the photometer corresponding to the six filter positions and three fields of view. To increase the data capacity of the storage medium the counts are not rescaled but instead a single digit, representing the scale factor, is coded into the scaled counts and recorded. This gives a data capacity of about nine hours of continuous operation which is adequate for a full nights observing.

A block diagram showing the complete photometer system can be seen in figure (3.6.1).

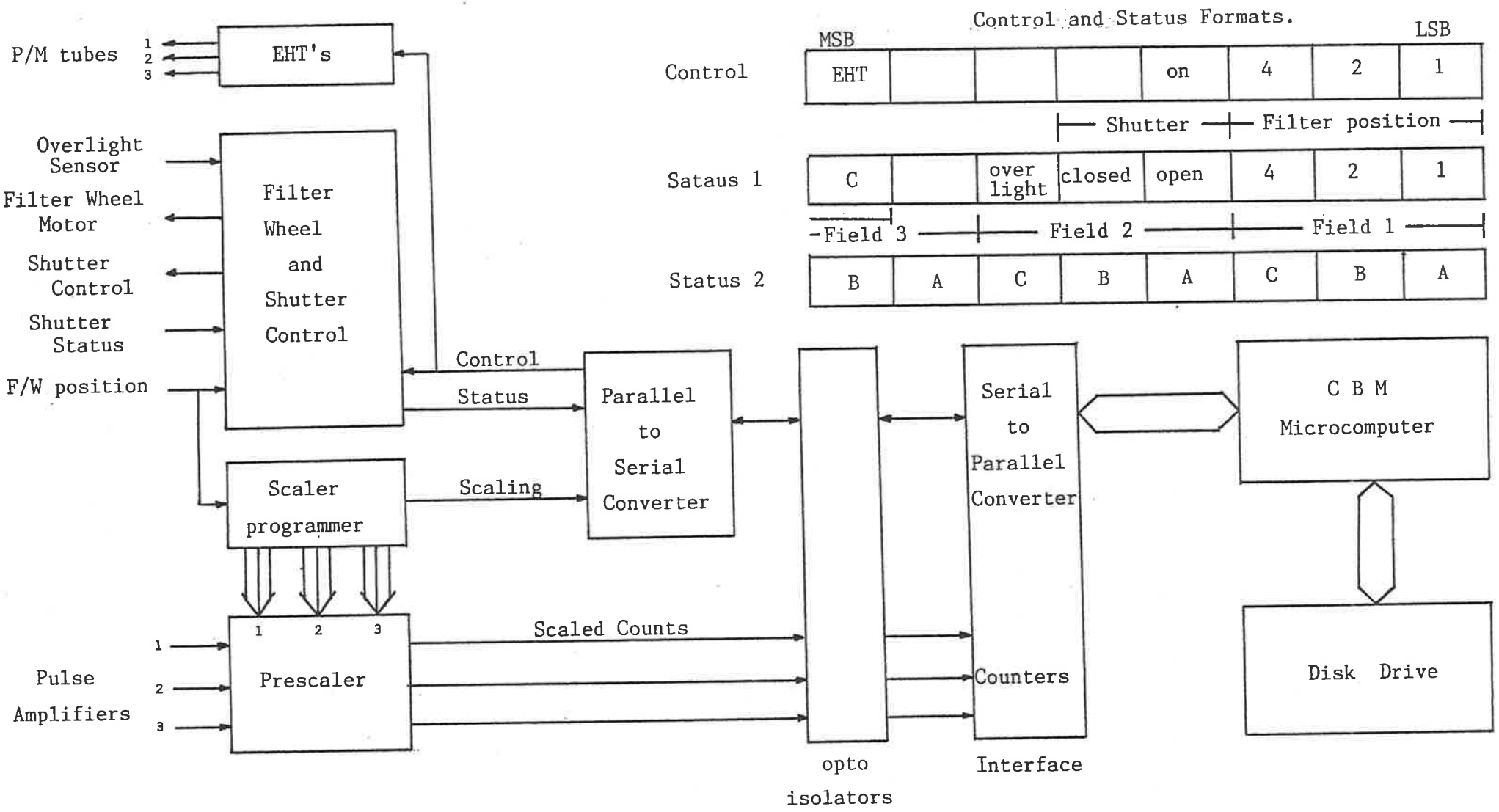

Figure 3.6.1. Block diagram of photometer and associated equipment.

Chapter 4. Data Analysis.

4.1. Introduction.

Between the months of December 1982 and July 1984 a total of 41 nights of photometer observations were recorded using the Mt. Torrens photometer. Power failures and other unforseen problems resulted in only 23 nights where the data length was of sufficient duration for adequate analysis. Due to poor observing conditions, only 16 of these 23 nights were of high enough quality to be considered for the presented analysis. Of the data selected, the seasonal distribution of the observations is approximately equal with six summer, six winter and four equinoxial observations.

Apart from diurnal variations, fluctuations in the nightglow intensity recorded by the photometer are considered to be mainly due to atmospheric gravity waves passing across the fields of view. In order to decompose this wave field into single wave groups of individual periods and velocities, a cross spectral analysis method was used on the records. This involved taking each pair of fields in turn and computing the amplitude and phase spectra for each frequency interval. An estimate of the coherence between the three cross spectra gives a measure of the correlation between the time series. These parameters enable phase and hence time shifts to be inferred for all periodicities showing high power and coherence. A true horizontal phase velocity can then be assigned to any detected wavelike disturbance.

The data, originally recorded on mini floppy disks, were transferred to mass storage on the University's Cyber 173 mainframe computer which was used for the analysis.

4.2. Data preselection.

The raw data for each night were plotted and visually inspected for quality. High correlation between the background recordings at λ435 nm, λ500 nm, and λ530 nm with the λ557.7 nm emission usually indicated extraneous light interference, presumably due to scattered light from cloud or haze. This contamination, although often intermittent, usually precluded the data from any further analysis. Acceptable data ideally contained smooth, oscillating fluctuations in the λ557.7 nm signal compared to the lower, much less eventful recordings of the background.

Occasionally, never simultaneously in all fields, random high level spurious spikes were monitored. The exact cause of these events is not known but since their duration was always for only one data point, their generation could not be due to any atmospheric airglow phenomena. Likely causes for these spikes are real emissions, such as meteors or aircraft lights or a non luminous effect generated by the photomultipliers and electronics from radioactive decay or electrical interference. These spikes were removed and set to the local data mean.

4.3. Prespectral data treatment.

For any given filter there is a time delay between measurements from one field to the next as the filter moves between fields on the filter wheel. Taking field one as an arbitary reference, if the filter wheel moves from field one to two and on to three, then the time series for field two is temporally retarded one third, for field three two thirds of a filter wheel revolution with respect to field one. For the case of a filter wheel revolution of thirty seconds field two lags field one by ten seconds and field three lags field one by twenty seconds. A parabolic interpolation over three points was used to advance fields two and three the necessary fractions of a data interval to make the observations in each of the three fields effectively simultaneous, (Bevington, 1969).

Although the photomultipliers were selected to be as similar as possible with their operating voltages set to give maximum signal to noise ratio, the gains of the tubes were different. In order that each field would be given equal weighting, the time series were normaized by dividing each series by its total number of counts.

The mean of each time series was subtracted and any linear trend removed to improve the stationarity of the data. This results in the removal of the zero frequency and the suppression of the lowest, non zero frequency component in the spectra.

Since the recordings were of finite duration the data series were multiplied by a data window of amplitude one which steps to zero outside the data interval.

The Fourier transform of the data is therefore the convolution of the data spectrum with the spectral window, the Fourier transform of the data window. The abrupt edges of a square data window give rise to side lobes in the spectral window which can leak power into the higher frequency components, decreasing their reliability, (Brault and White, 1971; Bracewell, 1965). To reduce this leakage the first and last 10% of the data were multiplied by a cosine taper thereby rounding the edges of the data window resulting in a significant attenuation of the side lobes, (Jenkins and Watts, 1969).

By shaping the data window, spectral leakage can be reduced but never entirely eliminated. Since the average data length was between seven and eight hours with a sampling interval of thirty seconds, the analysis could provide information for periodicities between one minute and about four hours. Inspection of the data suggested periods ranging from the Vaisala Brunt cut off to a few hours with a seemingly high percentage of periods between ten and forty minutes. In order to obtain the best spectral estimates for these frequencies, leakage from the lower frequencies could be further reduced by prewhitening the spectrum, (Jenkins, 1961). As the name suggests, this involves flattening or whitening the spectrum, decreasing the power in the lower frequencies and therefore further decreasing leakage caused by the spectral window. This is done prior to transformation by digitally filtering the data with a simple first difference filter

$$y_t = x_t - x_{t-1} \qquad (4.3.1.)$$

This results in the amplitude and phase spectra being multiplied by the gain and phase functions of the filter give by

$$G(f) = 2|\sin\pi f| \qquad 0 \leqslant f < 1/2\Delta t \qquad (4.3.2.)$$
$$\Phi(f) = \pi(f-\tfrac{1}{2})$$

where Δt is the sampling interval and f the frequency, (Jenkins and Watts, 1969). As can be seen the gain function strongly attenuates the low frequencies, acting as a high pass filter. Although the digital filter phase shifts the spectra, the relative phase between fields remains unaltered since the same filter is applied to the time series of all three fields.

4.4. Cross spectral estimates.

Each time series was then Fourier transformed using a fast Fourier transform routine, (Brigham, 1974). Where digital filtering was applied, the transform was recoloured by multipling by the inverse gain function. If $X_m(t)$ represents the time series for field m then

$$X_m(t) \overset{FFT}{\longleftrightarrow} A_m(f) + jB_m(f) \qquad (4.4.1.)$$
$$m=1,2,3$$

For the cross spectrum between two series, the in phase or co spectrum is defined as, (Jenkins and Watts, 1969)

$$L(f)_{mn} = [A_m(f)A_n(f) + B_m(f)B_n(f)]/G(f)T \qquad (4.4.2.)$$
$$mn=12,23,31$$

and the out of phase or quadrature spectrum

$$Q_{mn}(f) = [A_m(f)B_n(f) - A_n(f)B_m(f)]/G(f)T \qquad (4.4.3.)$$

$$mn=12,23,31$$

The cross spectrum is then

$$C_{mn}(f) = L_{mn}(f) \widehat{\oplus} Q_{mn}(f) \qquad (4.4.4.)$$

$$mn=12,23,31$$

To increase the reliability, these estimates can be averaged over several adjacent frequency intervals to give the smoothed spectral estimates $\overline{L}_{mn}$, $\overline{Q}_{mn}$, and $\overline{C}_{mn}$. For convenience the frequency dependence has been dropped in the following discussion.

The smoothed cross amplitude spectral estimate can now be defined as

$$\overline{A}_{mn} = (\overline{L}^2_{mn} + \overline{Q}^2_{mn})^{\frac{1}{2}} \qquad (4.4.5.)$$

For a bivariate analysis, the cross amplitude spectrum gives a measure of the common power between the two time series m and n for each frequency interval. Since both time series have been normalized, the cross amplitude estimates the spectral density.

The smoothed phase spectral estimator is,

$$\overline{\Phi}_{mn} = \arctan(-\overline{Q}_{mn}/\overline{L}_{mn}) \qquad (4.4.6.)$$

which estimates the phase difference between series m and n for each frequency interval.

When the spectral density and phase spectra are used in conjunction it is possible to identify frequencies having high power which are common to both series and the relative phase relationship at those frequencies.

An additional parameter is also introduced, the squared coherence spectral estimator.

$$\overline{K}^2_{mn} = \overline{A}^2_{mn} / \overline{C}_{mm}\overline{C}_{nn} \qquad (4.4.7.)$$

The smoothed squared coherence, or more conveniently the coherence, provides a non dimensional measure of the correlation between the two time series as a function of frequency, ranging from zero for uncorrelated series to one for identical series. It should be noted that the recolouring of the data does not change the phase or coherence spectra but only reconstitutes the weight to the lower frequency spectral components in the spectral density.

The length T of the record determines the extent to which peaks in the spectra may be distingushed: the minimum resolvable frequency is given by 2/T. The sampling interval, Δt determines the maximum frequency which can be obtained and is given by the Nyquist condition, $f_N = 1/2\Delta t$ Spectral smoothing by averaging over a number of spectral intervals, decreases the frequency resolution proportionally and a compromise must be made as to the reliability of the spectrum and the degree of resolution required.

The cross spectral analysis is done for each pair of fields taken cyclically. The three resulting cross and coherence spectra are averaged together to increase reliability without loss of resolution. This procedure is done for all of the observed optical emissions for each frequency interval.

4.5. Horizontal phase velocity.

The purpose of the spectral analysis is to determine the horizontal phase velocities of any periodic fluctuations present in the records. It is assumed that these fluctuations are principally due to the propagation of internal atmospheric gravity waves and that these waves exhibit plane wave fronts and do not significantly change in structure while passing over the fields of view of the photometer. These assumptions seem to be reasonable for medium scale gravity waves and make for a simpler calculation of horizontal phase velocity.

For a given optical emission, the phase spectrum $\overline{\Phi}_{mn}$ gives the time differences for each frequency interval between any two of the three fields.

$$\tau_{mn} = t_m - t_n = \overline{\Phi}_{mn}/2\pi f \qquad (4.5.1.)$$

The apparent velocities in the direction of the line joining fields m and n are therefore

$$v_{mn} = d/\tau_{mn} \qquad (4.5.2.)$$

where d=13 km, the distance separating the fields at the 95 km level. These velocities are component velocities of the wave front and a true phase velocity, $\underline{V}$ can be realized by taking the perpendicular from the origin to the line of best fit of the three apparent velocity vector endpoints, (Freund and Jacka, 1979). Figure (4.5.1) shows the field orientations for the Mt. Torrens photometer with an example of how the phase velocity is determined from the apparent velocities. The direction of $\underline{V}$ is given by θ taken clockwise from north. For the example given, the line of best fit can be considered as the wave front moving across the fields with speed indicated by the length of the vector V and direction θ. For this instance the wave front would first be detected in field two and then field one, so field two would lead field one. Similarly, field one leads field three so the apparent velocities v_{21} and v_{13} are positive, however, field three lags field two making v_{32} negative. Ideally the three time shifts should sum to zero and an indication of this is given by the linear correlation coefficient to the line of best fit, (Briggs and Golley, 1969).

4.6. Error estimates.

Since the photometer records only a small sample of the emitted photons from the nightglow pattern the time shifts, and hence the horizontal phase velocities, are statistical estimates of these parameters. Following Freund and Jacka (1979), the relative error in the phase

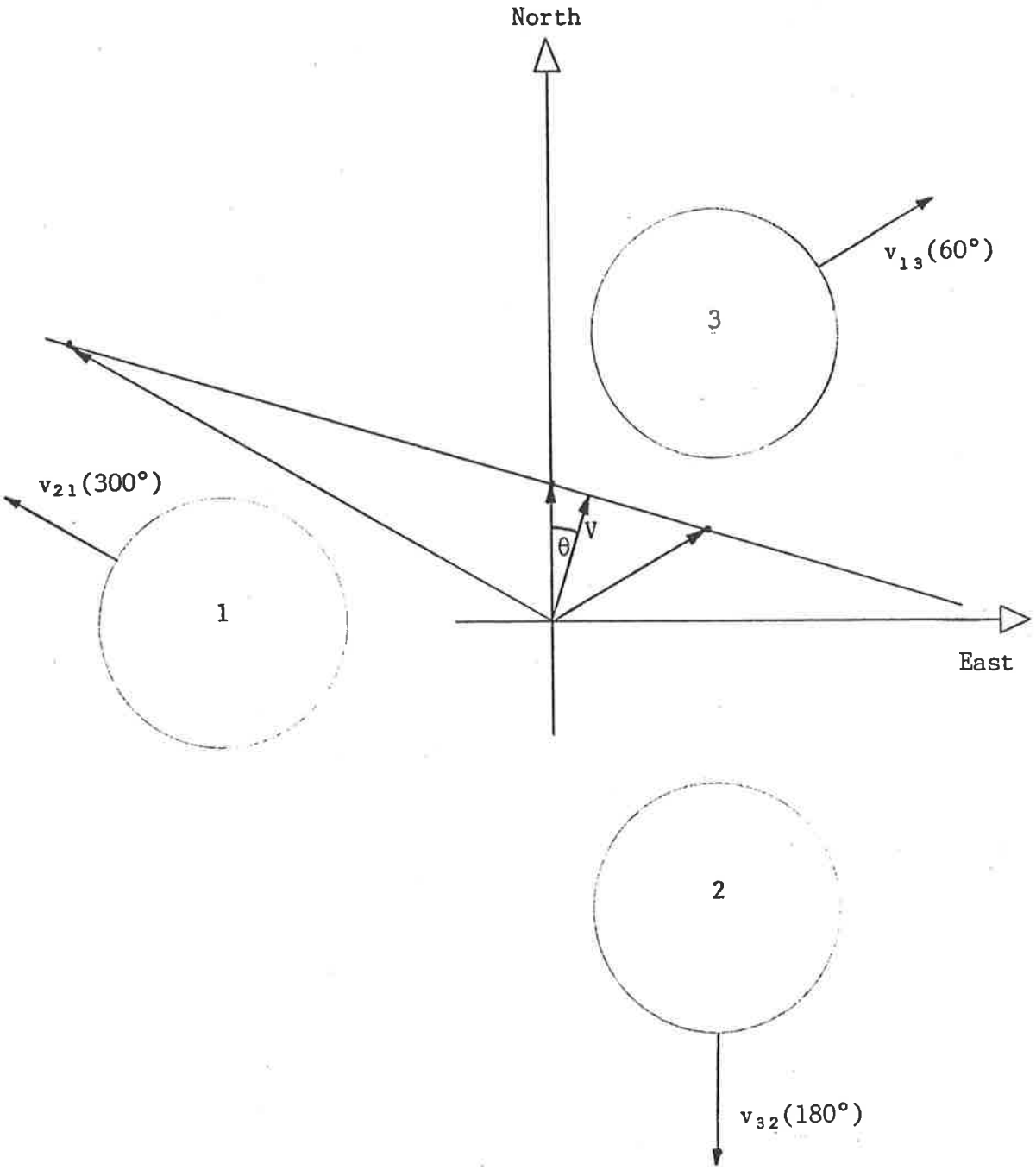

Figure 4.5.1. Field orientations of the Mt. Torrens photometer when projected to the 95 km level. The true phase velocity is the perpendicular, through the origin, to the line of best fit of the apparent velocity vectors.

velocity can be quantified by considering the expected number of photons to be recorded by field m from a sinusoidal oscillation to be represented as

$$\langle N_m(t) \rangle = N_o[1 + \frac{\varepsilon}{2} \sin \frac{2\pi(t - t_m)}{T}] \qquad (4.6.1.)$$

where T is the period of the oscillation, N_o the background level and ε the relative peak to peak intensity fluctuation, all considered constant. The general form of the variance of a function $f(x_i)$ may be written as, (Bevington, 1969)

$$\sigma^2(f) = \sum \left(\frac{\partial f}{\partial x_i}\right)^2 \sigma^2(x_i) \qquad (4.6.2.)$$

so

$$\sigma^2(N_m) = (N_o \varepsilon \pi / T)^2 (\cos^2 \frac{2\pi}{T}(t - t_m))\ \sigma^2(t_m) \qquad (4.6.3.)$$

If the signal is observed for a time T_L extending over several periods then the mean variance reduces to

$$\sigma^2(N_m) = (N_o \varepsilon \pi / T)^2\ T_L \sigma^2(t_m)/2 \qquad (4.6.4.)$$

since $\langle \cos^2 2\pi/T(t-t_m) \rangle = \frac{1}{2}$

Because N_m is distributed as a Poisson variate $\sigma^2(N_m) \simeq N_o$ so equation (4.6.4) can be written as

$$\sigma^2(t_m) = (T/\pi\varepsilon)^2 (2/N_o T_L) \qquad (4.6.5.)$$

The apparent velocities are expressed by equation (4.5.2) so for equivalent fields $\sigma^2(t_m)=\sigma^2(t_n)$, therefore

$$\sigma^2(v)/v^2 = 2v^2\sigma^2(t_m)/d^2 \qquad (4.6.6.)$$

Each field is viewed sequentially, therefore the mean relative error is increased by a factor of three. Combining equations (4.6.6) and (4.6.5) gives,

$$\frac{\sigma(v)}{v} = \frac{6vT}{d\pi\varepsilon(N_o T_L)^{\frac{1}{2}}} \qquad (4.6.7.)$$

To include the effects of the instrument then N_o can be taken to be the mean number of counts which can be expressed as $\omega\delta I_o x\, 10^6$ where ω is the solid angle of the field of view, I_o the mean nightglow intensity in Rayleighs, and δ incorporates the optic losses and detector efficiency. Observing a plane wave of period 20 minutes for 40 minutes and using the instrument specifications discussed in §3.3 and §3.5 with ε =0.02, then for an apparent velocity of say 50 ms^{-1} the mean relative error that can be expected in the apparent velocity is about 2%.

Further error is also introduced in the method of analysis. The variance of the spectral estimates can be reduced by smoothing, however this decreases the resolution and a compromise must be reached. To estimate this error in the phase velocity derived from the spectral analysis requires an estimate of the spectral phase variance.

This is given by, (Jenkins and Watts, 1969)

$$\sigma^2(\bar{\Phi}_{mn}) \simeq (1/\nu)[1/\bar{K}^2_{mn} - 1] \qquad (4.6.8.)$$

where ν is the number of spectral estimates averaged and $\bar{K}^2_{mn}$ the mean coherence. As can be seen, for the variance in the phase estimate to be small the time series must exhibit high coherence.

As mentioned earlier, a finite data length implies a convolution of the spectrum with the spectral window. The effect of this is to broaden the spectral peaks and introduce leakage between closely spaced frequency intervals, introducing a bias into the spectrum. This leakage can be reduced by window shaping but not eliminated. The most significant bias appears in the quadrature spectra, near zero where the amplitude is small or in areas where the spectrum changes rapidly. This leakage produces bias in the phase estimate and can be expressed as, (Jenkins and Watts, 1969)

$$B(\bar{\Phi}_{mn}) \simeq \frac{0.063}{T^2}\left(\frac{d\bar{\Phi}_{mn}}{df}\frac{d}{df}\ln\bar{A}^2_{mn}\right) \qquad (4.6.9.)$$

The constant relates the type of window used and the equation can be rewitten using $df = \nu/T$

$$B(\bar{\Phi}_{mn}) \simeq \frac{0.063}{\nu^2}\,\Delta\bar{\Phi}_{mn}\,\Delta\ln(\bar{A}^2_{mn}) \qquad (4.6.10.)$$

The mean square error, or the variance of the true phase velocity is given by the sum of equations (4.6.8) and (4.6.10)

$$\sigma^2(\bar{\Phi}_{mn}) \simeq \frac{0.004}{\nu^4} \left(\Delta\bar{\Phi}_{mn}\Delta\ln\bar{A}^2_{mn}\right)^2 + \frac{1}{\nu}\left(\frac{1}{\bar{\bar{K}}^2_{mn}}-1\right) \qquad (4.6.11.)$$

with $\sigma^2(\tau_{mn}) = \sigma^2(\bar{\Phi}_{mn})/(2\pi f)^2$

As discussed in §4.5, a straight line is fitted to the apparent velocity vector endpoints. This is done by transforming the vectors to an x,y (East, North) coordinate system and using a standard least square fitting routine to give the line of best fit, y=a+bx. The relative error in the apparent velocity is $\sigma^2(v)/v^2 = \sigma^2(\tau)/\tau^2$ where the subscripts have been omitted for clarity. This shows that the errors in the velocities are not equally weighted since the error in the apparent velocity is large for small time shifts. The uncertainty in the coefficients are then approximated by, (Bevington, 1969)

$$\sigma^2(a) = \frac{1}{\Delta}\sum(x_i^2/y_i) \; ; \; \sigma^2(b) = \frac{1}{\Delta}\sum(1/y_i) \qquad (4.6.12.)$$

where $\Delta = \sum(1/y_i)\sum(x_i^2/y_i) - [\sum(x_i/y_i)]^2$

The horizontal phase velocity, $\underline{V}$ is found from the perpendicular, through the origin, to the line of best fit. The distance of the origin to the intersection of the line y=a+bx and y=-x/b gives the magnitude of the velocity with the direction measured clockwise from the y axis. In

polar coordinates the velocity can be represented,

$$\underline{V}(r,\theta) = \underline{V}[(a^2/b^2+1)^{\frac{1}{2}}, \arctan(-b)] \qquad (4.6.13.)$$

From the above equation the uncertainty in the magnitude of the velocity can be determined as

$$\sigma^2(v)/v^2 = \sigma^2(a)/a^2 + \sigma^2(b)/b^2 \qquad (4.6.14.)$$

and the direction

$$\sigma^2(\theta) = \sigma^2(b) \cos^4\theta \qquad (4.6.15)$$

4.7. Selection criteria.

This analysis was carried out for each pair of fields taken cyclically, i.e. mn=(1,3), (3,2) and (2,1), resulting in a phase velocity with associated error estimate and linear correlation coefficient, mean spectral density and coherence for each frequency interval up to the Nyquist cut off for the λ557.7 nm and background emissions. In order to examine any short periodicities in the data which may be averaged out if coherent only for a few cycles, the data from each night was multiplied by a data window of variable length. The analysis was then iterated for each window and stepped an interval of about 20% of the window length along the full data length. The data were also analysed by first averaging over two spectral estimates, thereby giving good frequency

resolution, and again averaged over three or four to give greater reliability once dominant periodicities were indentified.

For apparent periodicities to be regarded as real periodic intensity fluctuations passing over all three fields of the photometer, they must show high spectral power in all fields and a mean coherence corresponding to a 90% or larger confidence level, (Julian, 1975). The linear correlation coefficient to the line of best fit must also be high since this discriminates against periodicities with horizontal wavelengths less than twice the field spacing.

When the analysis is iterated, each time the data window is stepped, the above selection criteria and the phase velocity must exhibit consistency between at least two consecutive windows. Periodicities selected this way should have phase velocity error estimates typically less than 20% and to be considered as resulting from the λ557.7 nm emission, should not show any correlation with the results of the background analysis for the same frequency interval. The phase velocity of the selected periodicities naturally varies as the data window is stepped along. This may be due to the wave train accelerating or rotating with time or to random errors of the analysis. A weighted mean was taken using the velocity error estimates as the weighting factors.

The entire analysis procedure was tested and verified using computer generated time series of several known periodicities, relative time shifts and noise.

4.8. Results.

Of the 16 nights of acceptable data, a total of 130 periodicities satisfied the selection criteria and are considered to be manifestations of gravity waves as they pass through the λ557.7 nm emission layer. A number distribution of the observed periods of these selected waves can be seen in figure (4.8.1) in period intervals of 20 minutes. Also shown is the horizontal wavelength distribution calculated from the observed wave phase velocity and period. As suggested by the histograms, the majority of detected waves are of the shorter periods with horizontal wavelengths below a few hundred kilometres. However, this observation is considerably biased towards the shorter periods and wavelengths due to the relatively short observational data length. For observation periods of say seven hours in the summer to nine hours in winter, wave periods greater than half the data length are disregarded by the analysis due to the large unreliability of this lowest frequency interval, (Jenkins and Watts, 1969). The reduction of the data window lengths and stepping of data windows, as discussed in the previous section, also favours the detection of the shorter wave periods for the same reason.

The estimation of direction of gravity wave phase velocity suffers no such bias and provides some useful information. Figures (4.8.2.) show the directions of phase propagation for observed waves for summer and winter. This direction is indicated by an arrow, the length of which is proportional to the phase speed.

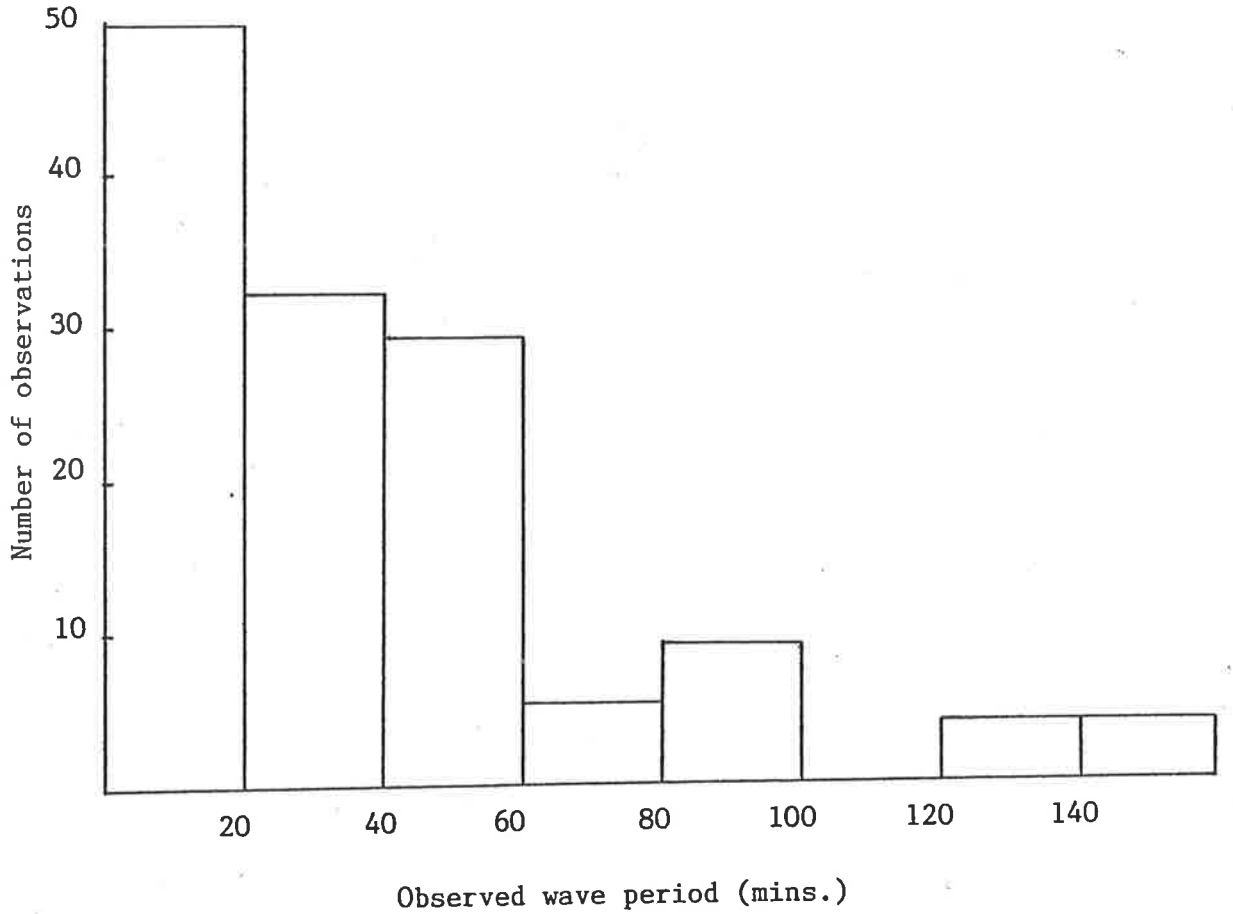

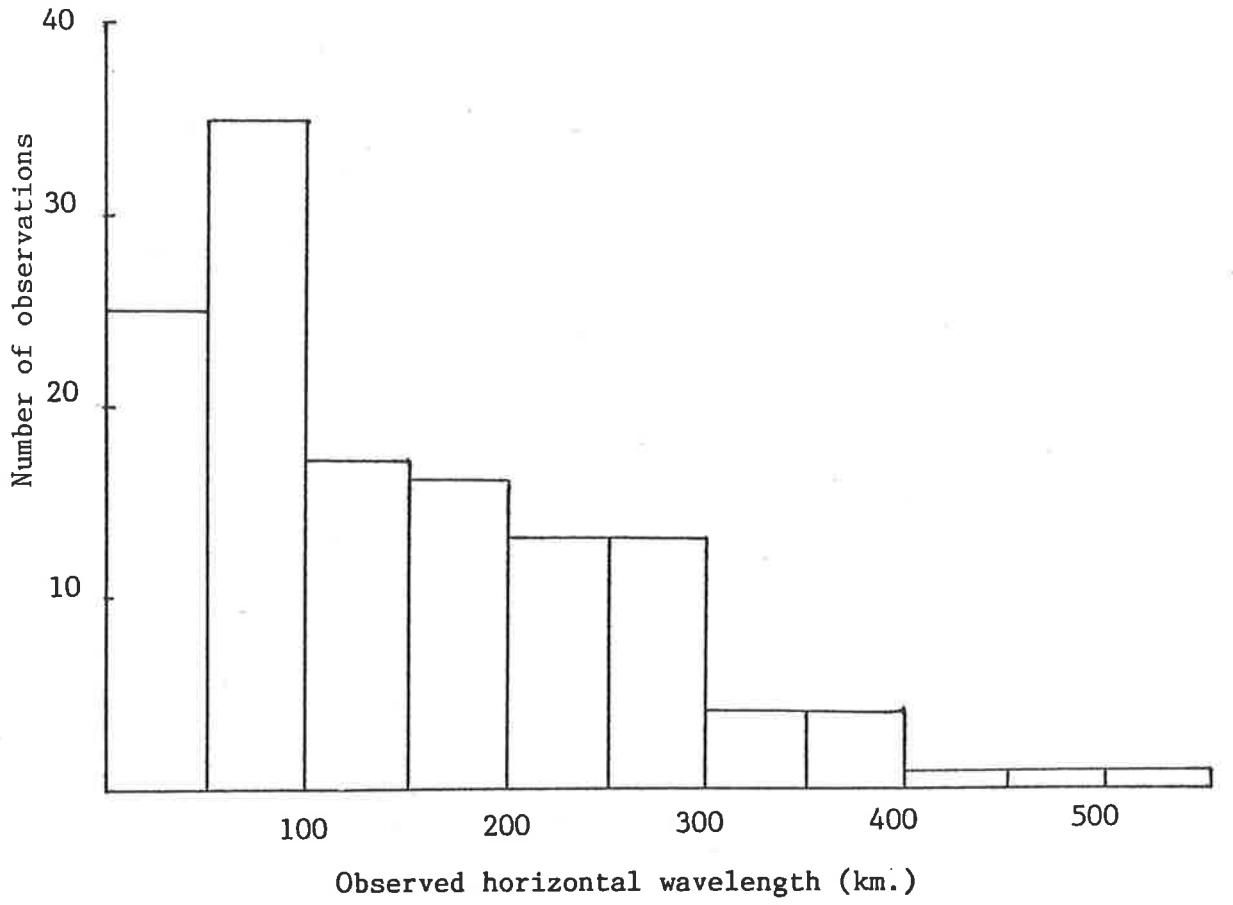

Figure 4.8.1. Number distribution of waves observed from 3FP against wave period and horizontal wavelength.

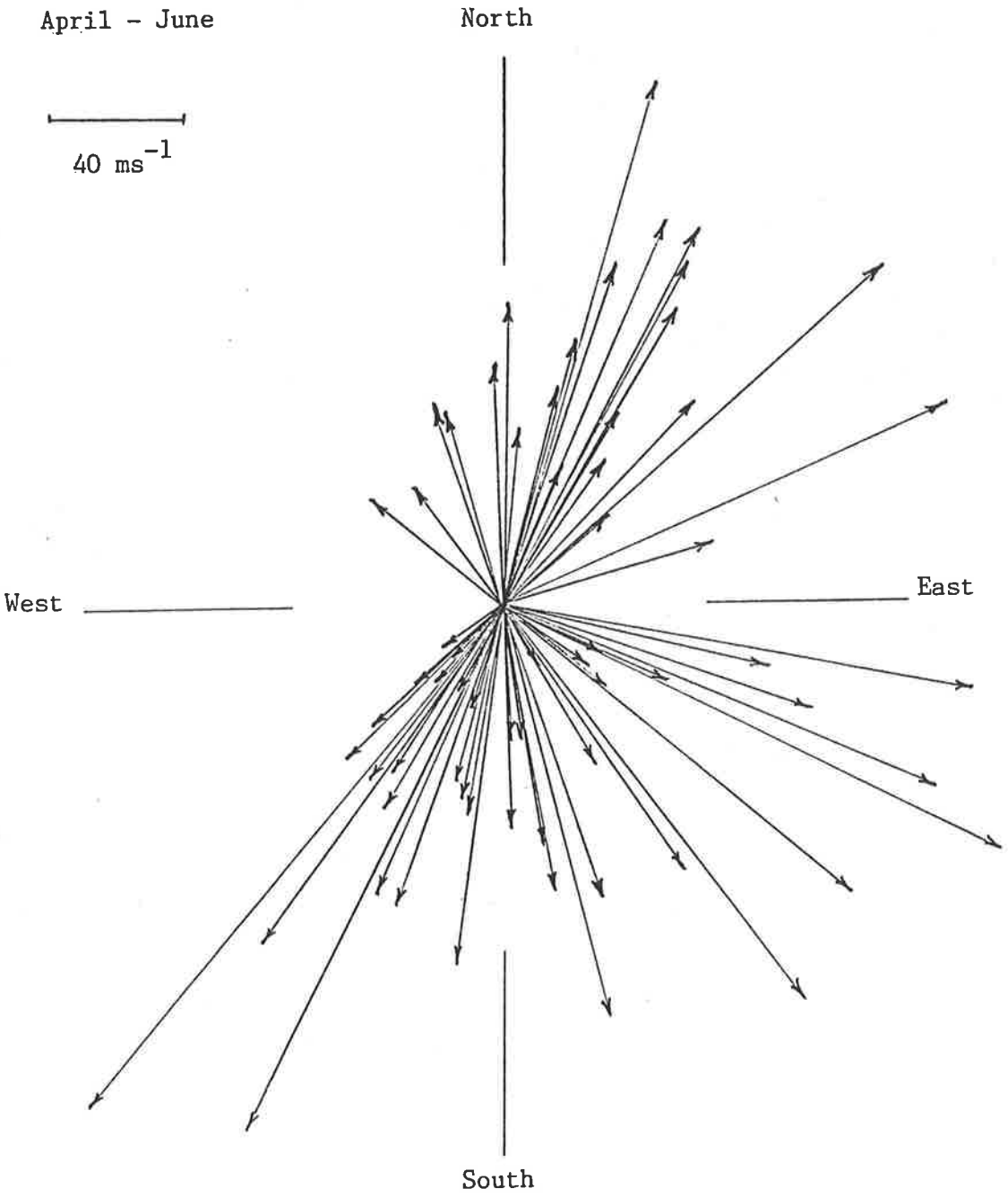

Figure 4.8.2a. Gravity wave phase velocities observed by the 3FP. Velocity directions indicate some degree of polarization by the middle atmosphere winds.

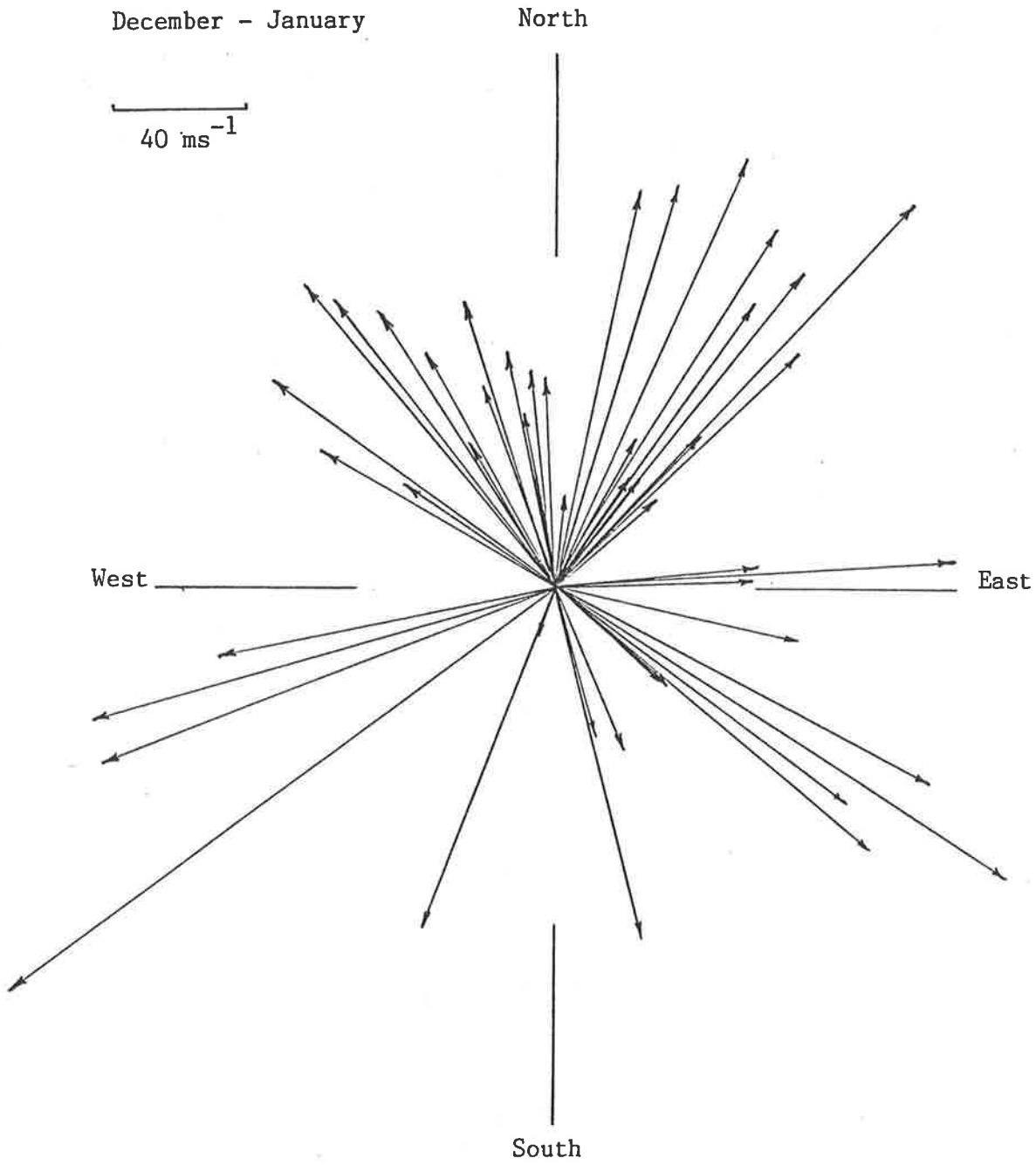

Figure 4.8.2b. Gravity wave phase velocities observed by the 3FP. Velocity directions indicate some degree of polarization by the middle atmosphere winds.

As can be seen, both seasons show a defficiency of waves in the east-west or zonal azimuth. This depletion may be attributed to the effects of the middle atmosphere wind system on the gravity wave field as it propagates through the atmosphere.

As mentioned in §2.4, upward propagating waves may encounter critical levels in the atmosphere due to background winds. Gravity wave frequencies can be Doppler shifted to the local Vaisala Brunt frequency and downwardly reflected for waves propagating anti-parallel to the wind, or, waves travelling with the wind may have their frequencies shifted to zero. In either case the wave will be unable to reach the upper atmosphere.

In the middle atmosphere the winter mean zonal flow at mid latitudes peaks at about 60 km with a velocity of around 80 ms^{-1} to the east. This zonal flow is reversed in summer, reaching a maximum of about 60 ms^{-1} to the west at a similar altitude, (CIRA, 1965). The mean meridional wind component is generally much smaller than the zonal component and will be neglected for the following discussion, (Geller, 1979).

Consider a directionally isotropic gravity wave field generated in the troposphere and propagating through the middle atmosphere. In the summer, waves propagating to the west, in the direction of the wind, may be Doppler shifted to zero frequency if their phase velocities are too low or reflected if travelling towards the east if the wave frequency is shifted to the Vaisala Brunt cut off.

Conversely in the winter, where the zonal flow is stronger and to the east, waves travelling in this direction can be absorbed by the background flow whereas waves in the opposite direction may be reflected. Both conditions will result in the observed depletion of zonally directed gravity waves detected at 95 km with the winter observations showing the effect to a greater extent.

The partial polarization of the gravity wave field, assumed initially unpolarized, adds credibility to the presumption that the majority of waves at the 95 km level originate from the lower atmosphere, a subject considered in greater detail in the following chapter.

Chapter 5. Gravity Wave Sources.

5.1. Introduction.

Results from the cross spectral analysis of the 3FP data have indicated the presence of highly regular periodic fluctuations in the λ557.7 nm nightglow emission due to the propagation of gravity waves. This and other observational photometric evidence such as Freund and Jacka, (1979); Meek and Manson, (1983); Armstrong, (1982); Gavrilov and Shved, (1982) with the radio observations of Manson and Meek, (1980); Herron, (1973) clearly indicate that gravity waves are a major feature of the upper atmosphere. The question naturally arises as to their origin.

It seems likely, as suggested by Hines, (1974) and Gossard, (1962), that gravity waves are generated in the more energetic regions of the lower atmosphere and transport this energy upward. Only small amplitude waves need be generated, growing exponentially with height as they propagate, to become increasingly noticable as they influence the more rarefied regions. This energy may be dissipated in the form of heat or momentum of the mean flow, effecting the temperature and circulation of the middle and upper atmosphere.

To establish possible sources for the waves detected, a reverse ray tracing technique was used to follow the ray paths of waves observed at 95 km down through the atmosphere to an arbitary height of 10 km, the approximate

altitude of the tropopause, where it is likely that meteorological phenomena are a major source of the waves detected, (Hines 1974; Bertin et al 1975; Kersley and Rees 1982).

5.2. Ray theory.

Unless the detected waves are generated at the height of observation then they must be free to propagate vertically through the atmosphere. For the case of medium scale gravity waves, the properties of the atmosphere do not significantly change over a wavelength and the absence of any solid boundary conditions validate the free wave approach. The method used here follows that discussed by Cowling et al, (1971) where the atmosphere is considered to be stratified into horizontal isothermal layers with the neutral background wind constant within each layer. The angular frequency of a gravity wave, ω as viewed by a stationary observer will be shifted in frequency compared to a frame of reference moving with any background wind. For non relativistic velocities the Doppler shifted frequency is given by the Galilean transformation

$$\Omega = \omega - \underline{k}.\underline{U} \qquad (5.2.1.)$$

where Ω is the angular frequency in the moving frame or the intrinsic frequency, $\underline{k}$ the wave vector and $\underline{U}$ the wind vector whose vertical component is assumed negligable. With a knowledge of the vertical profile of the wind, the

above transformation allows the dispersion equation for gravity waves in an isothermal, stationary atmosphere to be used in describing the wave parameters in each horizontal layer. The dispersion equation

$$k_z^2 = \left(\frac{N^2}{\Omega^2} - 1\right) k_h^2 + \frac{\Omega^2 - N_A^2}{C^2} \qquad (5.2.2.)$$

of §2.2 has been made applicable to a stationary layer by the substitution of the intrinsic frequency. For simplicity, the effect of the earths rotation has been neglected. For waves with periods of only a few hours this effect contributes only about 1%. The earths curvature has also been neglected in the following plane geometry approach. This simplyfing assumption can be justified since the area under consideration is only a small fraction of the earths surface and the effect of curvature is nearly compensated by the refraction of a gravity wave induced by the changing direction of the earths gravitational field, (Francis, 1972).

Ray tracing follows the path of the wave packet which moves with a group velocity defined as

$$\underline{V}_g = \underline{\nabla}_k \Omega(\underline{k}) \qquad (5.2.3.)$$

The horizontal and vertical components of the group velocity in the moving frame, S' can be found from equations (5.2.2) and (5.2.3) to be

$$V'_{gh} = \frac{(N^2 - \Omega^2)/\Omega C^2 k_h^2}{C^2(k_h^2+k_z^2) - 2\Omega^2 + N_A^2} \qquad (5.2.4a.)$$

and

$$V'_{gz} = \frac{-C^2 k_z \Omega}{C^2(k_h^2+k_z^2) - 2\Omega^2 + N_A^2} \qquad (5.2.4b.)$$

The negative sign indicating that for downward phase progression there is an upward flow of energy. The group velocities in the earths stationary frame are given by the transformation

$$V_{gh} = V'_{gh} + U_h \qquad (5.2.5a.)$$

and

$$V_{gz} = V'_{gz} \qquad (5.2.5b.)$$

The transit time of the wave packet through a horizontal layer is identical in both frames and is given by

$$t = 1/V_{gz} \qquad (5.2.6.)$$

where 1 is the horizontal slab thickness at height z. Therefore the horizontal displacement of the wave packet is

$$d_h = V_{gh}\ 1\ /\ V_{gz} \qquad (5.2.7.)$$

giving the position vector for the wave packet at time t as

$\underline{r} = \underline{r}(dx,dy,dz,t)$

The kinematic boundary conditions imposed by Snell's law require that the horizontal wave vector k_h and the angular wave frequency, ω, remain constant across each layer. This condition, along with the Galilean transformations, imply that the effect of the background wind is to Doppler shift the wave frequency for wind components parallel to the wave propagation vector $\underline{k}$, and to rotate $\underline{k}$ for perpendicular wind components as viewed by a stationary observer on the earth. In essence the wave packet is advected by the background wind in addition to its own propagation relative to the moving system. Since these wave parameters are constant, then as the wave moves through the non isothermal atmosphere, albeit via isothermal layers, the vertical wave number, k_z varies in accordance to the dispersion equation.

It should be noted that each layer is assumed stable and when a wave interacts with the layer, no turbulence is initiated. This is consistent with the underlying assumptions that the gravity waves are of a small pertubating amplitude and do not introduce higher order or non linear effects.

5.3. Atmospheric profiles.

As pointed out in the previous section, the wind velocity is required to determine the ray path as are the speed of sound, the Vaisala Brunt and acoustic cut off frequencies. For an isotermal layer, (Hines, 1960)

$$N = (\gamma - 1)^{\frac{1}{2}} g/C \qquad (5.3.1a.)$$

$$N_A = \gamma g/2C \qquad (5.3.1b.)$$

and

$$C^2 = \gamma g H \qquad (5.3.1c.)$$

where γ is the ratio of specific heats and for altitudes less than 100 km has a reasonably constant value of 1.4. Using this value then the above equations can be written as

$$N^2 = 0.29\ g/H \qquad (5.3.2a.)$$

$$N_A^2 = 0.35\ g/H \qquad (5.3.2b.)$$

$$C^2 = 1.4\ g/H \qquad (5.3.2c.)$$

where the pressure scale height incorporates the temperature profile of the atmosphere. Tabulated values of H and g were taken from the U.S. Standard Atmosphere, (1976) and used to formulate the altitude profiles for N, N_A and C.

Mean monthly meridional and zonal wind profiles from the ground to 100 km were obtained from several different sources and combined to give mean monthly profiles. Balloon measurements, centred on Adelaide were supplied by the Adelaide Bureau of Meteorology and gave wind components to 30 km. Groves, (1971) gives monthly averages for 30° S and 40° S in the region of 25 km to 60 km and Groves, (1969) from 60 km to 130 km.

Another set of profiles which slightly differ from those given by Groves were adapted from CIRA, (1965) and Murgatroyd and Singleton (1961). These profiles were averaged and weighted towards a third set of profiles from Vincent et al (to be published) from the radar measurements near Adelaide.

It should be noted that because the wind profiles are monthly averages, they contain no contribution from the diurnal and semidiurnal atmospheric tidal oscillations. The amplitude of the tides grow exponentially with height due to the corresponding decrease in atmospheric density. For this reason their effect on the mean flow can be considered negligable below an altitude of about 80 km, (Ball, 1981).

All photometer observations were made between the hours of around 20:00 L.T. and 5:00 L.T. Measurements of the amplitude and phase of the diurnal and semidiurnal tides made near Adelaide between 80 km and 100 km, (Vincent and Ball, 1981) suggest that during 3FP observing times both tides contribute less than 10 ms^{-1} to the zonal and meridional mean flow above 80 km. Since this tidal contribution is small compared to the mean flow, and only effective over less than 20% of the reverse tracing, it was chosen not to include the tidal components in the wind profiles used for the reverse ray tracings.

The combination of these profiles, although unlikely to be the exact wind field for the nights concerned, are assumed not to deviate radically from the nightly average.

Plots of the meridional and zonal averaged wind profiles used can be seen in figures (5.3.1) for the months where the data was available for ray tracing.

5.4. Reverse ray tracing.

The reverse ray tracings were done on a CBM micro computer. The wind profiles were digitized with a 500 metre height resolution as were the data for the scale height and gravitational acceleration. The data analysis of Chapter 4 gives an estimate of the horizontal phase velocity and the Doppler shifted wave angular frequency for periodicites discerned as being gravity waves propagating through the 95 km level. From these estimates the horizontal wave number, which remains invariant throughout the tracing, is given by

$$k_h = \omega / V_h$$

Consider a wave in the first 500 metre thick slab at 95 km for which a horizontal wave number has been established. From the horizontal wind vector appropriate to this layer, an intrinsic wave frequency is calculated using equation (5.2.1). This, together with values of C^2,N^2, and N_A^2 , caculated for any given layer using equations (5.3.2), give a value for k_z^2 from the dispersion equation (5.2.2). The vertical and horizontal group velocities can then be deduced from equations (5.2.4) and transformed to the earths stationary frame using equation (5.2.5). The transit time of a wave packet through the layer and hence the horizontal displacement at the bottom of the layer are given by equations (5.2.6) and (5.2.7).

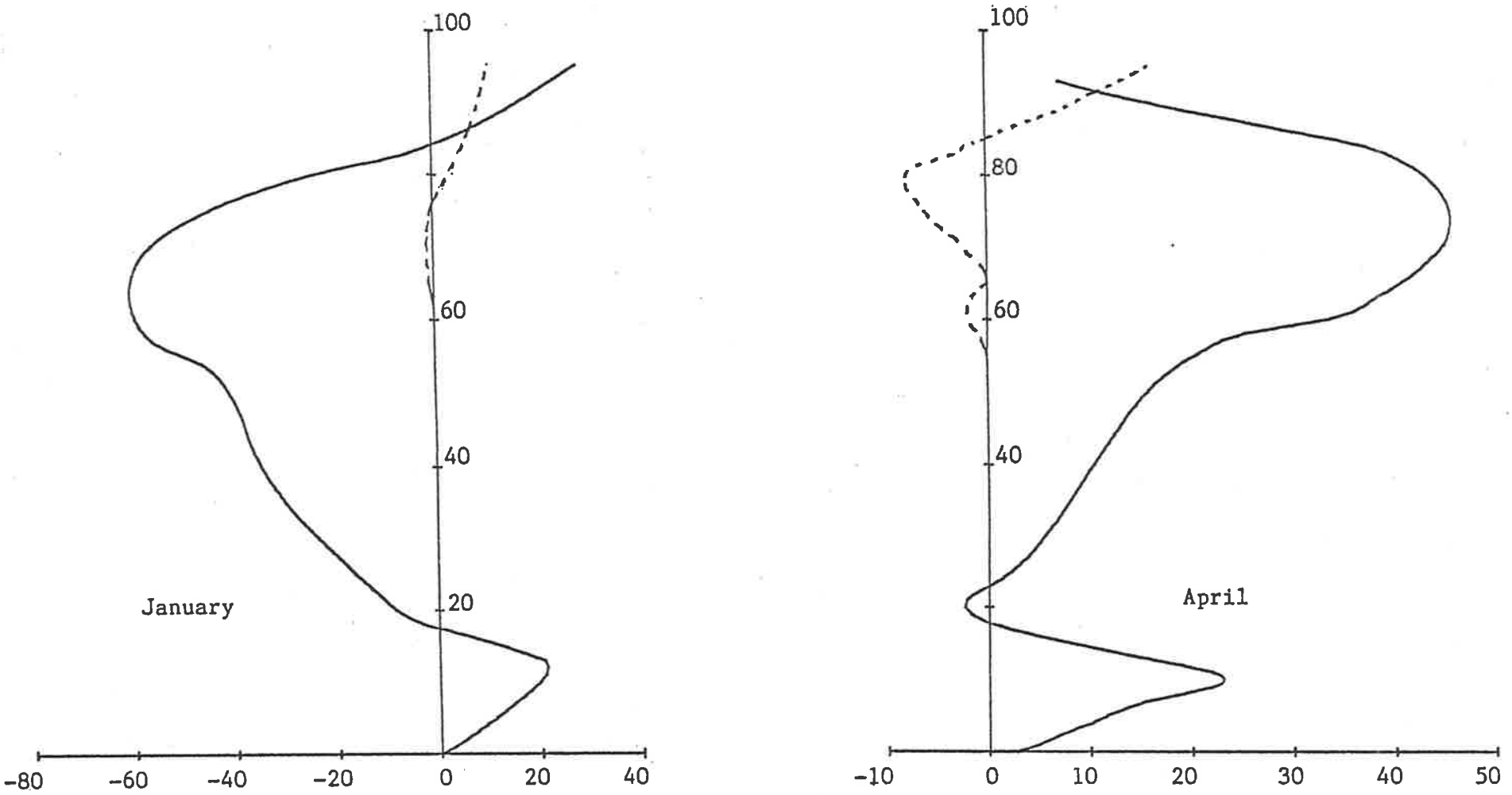

Figure 5.3.1a Mean zonal (solid) and meridional (dashed) wind profiles for 35° S. Wind velocities are in metres per second and positive for winds to the north and east.

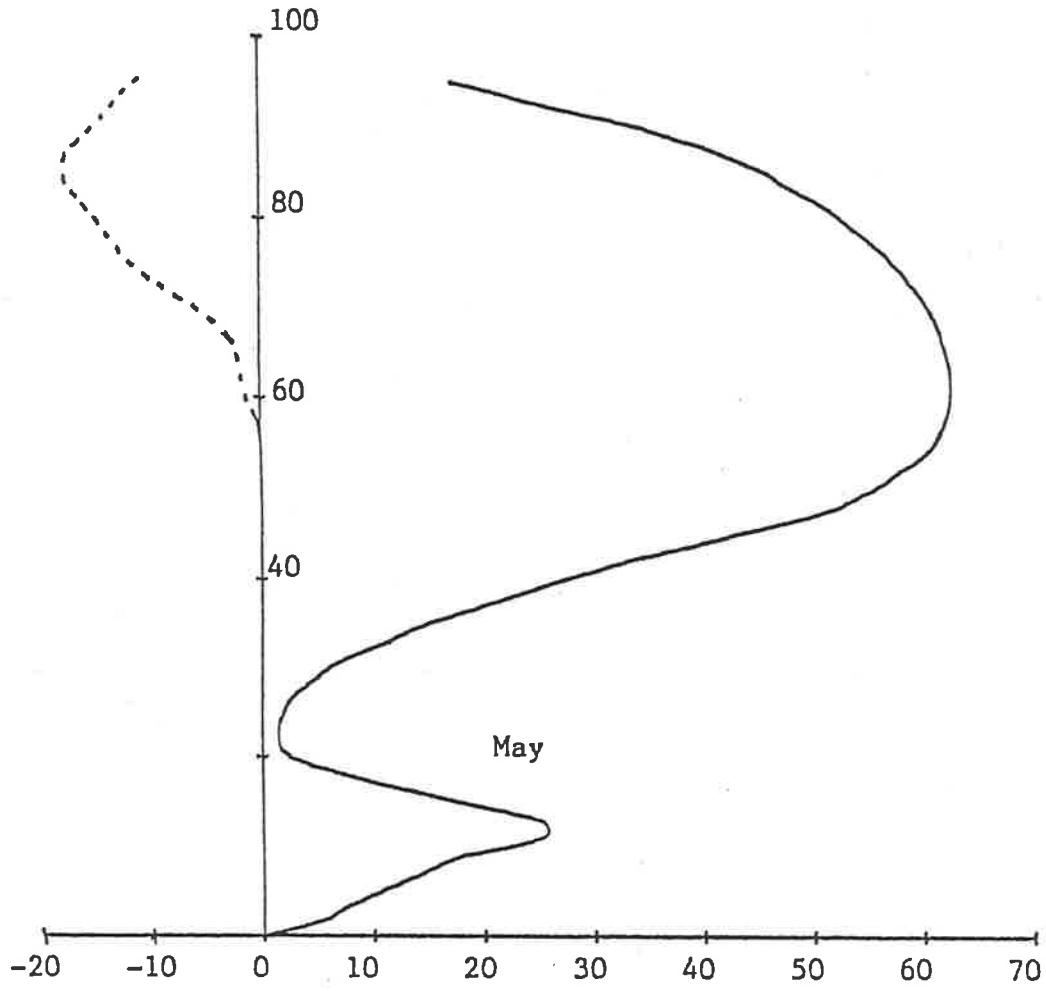

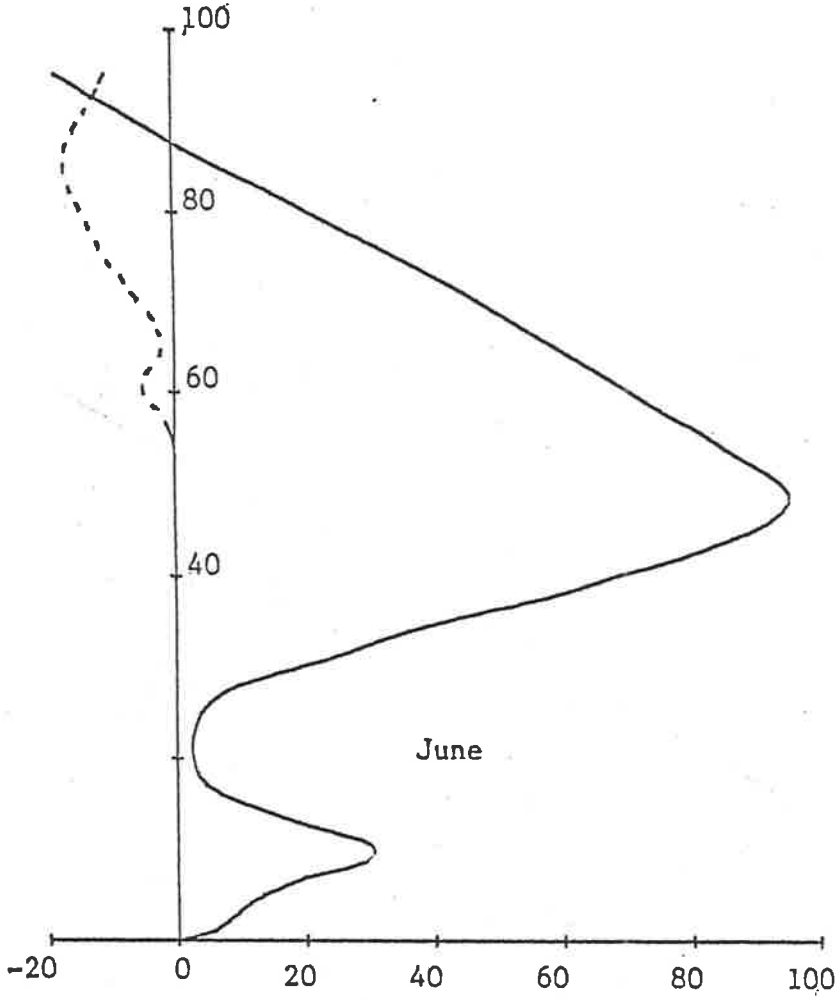

Figure 5.3.1b Mean zonal (solid) and meridional (dashed) wind profiles for 35° S. Wind velocities are in metres per second and positive for winds to the north and east.

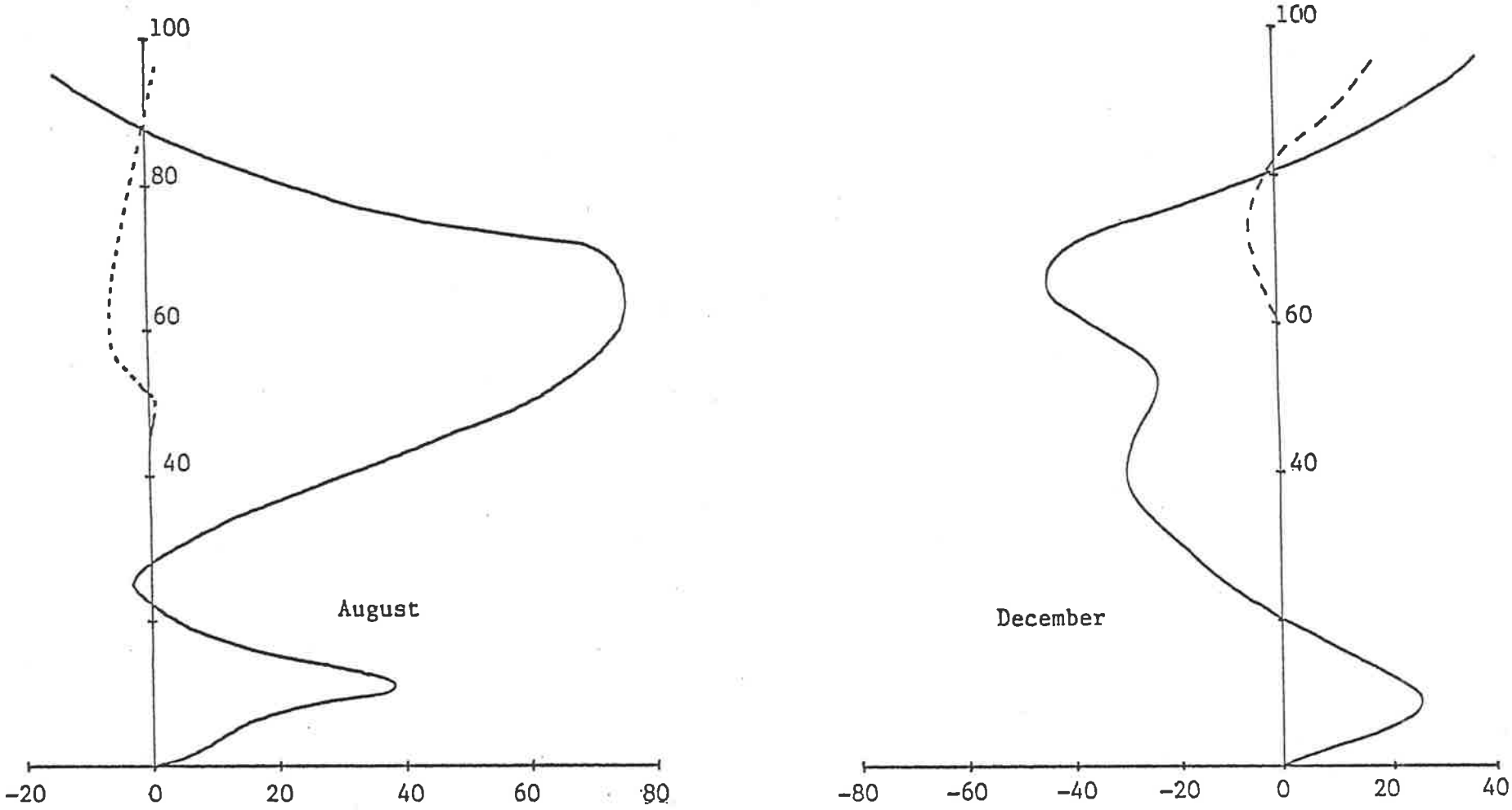

Figure 5.3.1c Mean zonal (solid) and meridional (dashed) wind profiles for 35° S. Wind velocities are in metres per second and positive for winds to the north and east.

This process is iterated through each layer from 95 km down to 10 km using the appropriate atmospheric parameters pertinent to that layer. The final position with respect to the stationary reference frame is then

$$\underline{r} = \int V_{gh} . dt \qquad (5.4.1.)$$

with the total transit time

$$T_{trans} = \int dt \qquad (5.4.2.)$$

Gravity waves can be considered to propagate vertically if $k_z^2 > 0$ and evanescent, unable to transport energy vertically, if $k_z^2 < 0$. This can occur when $\Omega^2 > N^2$ and may be interpreted as representing a reflection level. This would suggest that a wave traced to a reflection level would have been unable to transmit energy through that level from below. This may not always be the case since, depending on the thickness of the layer where reflection takes place, energy may be transmitted through the region by a tunelling effect if the layer is quite thin. Therefore if a reflection level is encountered by reverse ray tracing it is ambiguous as to whether the wave was generated above the reflection level or energy was leaked through from a wave generated from below, (Ball, 1981).

A critical layer is encountered when the horizontal phase velocity approaches the velocity of the background

wind, the wave frequency being Doppler shifted to zero. Here the vertical group velocity tends to zero as the energy propagates more and more horizontally, eventually transferring the wave energy to the mean flow, with negligable energy penetrating the layer, (Hines 1974).

Vincent, (1969) has suggested there is a possibility of spurious reflections if the chosen horizontal layer thickness is too great in a region where the temperature gradient is large. To reduce this likelyhood, he proposes layer widths of less than $\lambda_z/10$. The reverse ray tracing computation was terminated at a reflection level, critical layer or when the vertical wavelength was less than ten times the layer width.

The tracing of waves from 95 km to 10 km does not necessarily mean that the waves originate at 10 km. Such a tracing means that it is possible for the waves to be generated near 10 km but could have originated from any altitude along the ray path.

The reverse ray tracing program was tested using hypothetical phase velocities and produced consistent results in both reverse and forward tracings.

Because of the uncertainty and variety of wave generation mechanisms, the geographical separation between source and observation, the time delays between generation and detection and the small number of observations available, a statistical analysis of possible wave sources would prove fruitless. Therefore each individual case is presented separately, enabling some general conclusions to be reached.

5.5. Results.

The results of the reverse ray tracings from the level of detection to the tropopause can been seen in figures (5.5.1), superimposed on a coastal outline of Australia. As an empirical estimation to the error in the position of the gravity wave source, several tracings were performed for each wave using the limits of the error estimate of the horizontal phase velocity, both in magnitude and direction. A circle of minimum confusion, containing all of the resultant launch positions, is then used as an indication to the uncertainty of the launch site. Tracing resulting in launch sites beyond the border of the map are not included since the uncertainty becomes unacceptable over large distances and it is likely that over such distances, atmospheric profiles are significantly altered. Apart from these, all tracings which terminate at the tropopause are included.

Each map presents the tracings of data from one night with the launch site of each wave identified using the observed wave period, in minutes, with the calculated azimuth of the normal to the wave front at the 10 km level indicated by an arrow. The inset tabulation gives the transit time of wave propagation to the nearest ten minutes and the estimated launch time for each wave. The launch time is calculated simply by subtracting the transit time from the centre time of the data window where the wave was first detected. It should only be regarded as an indicator.

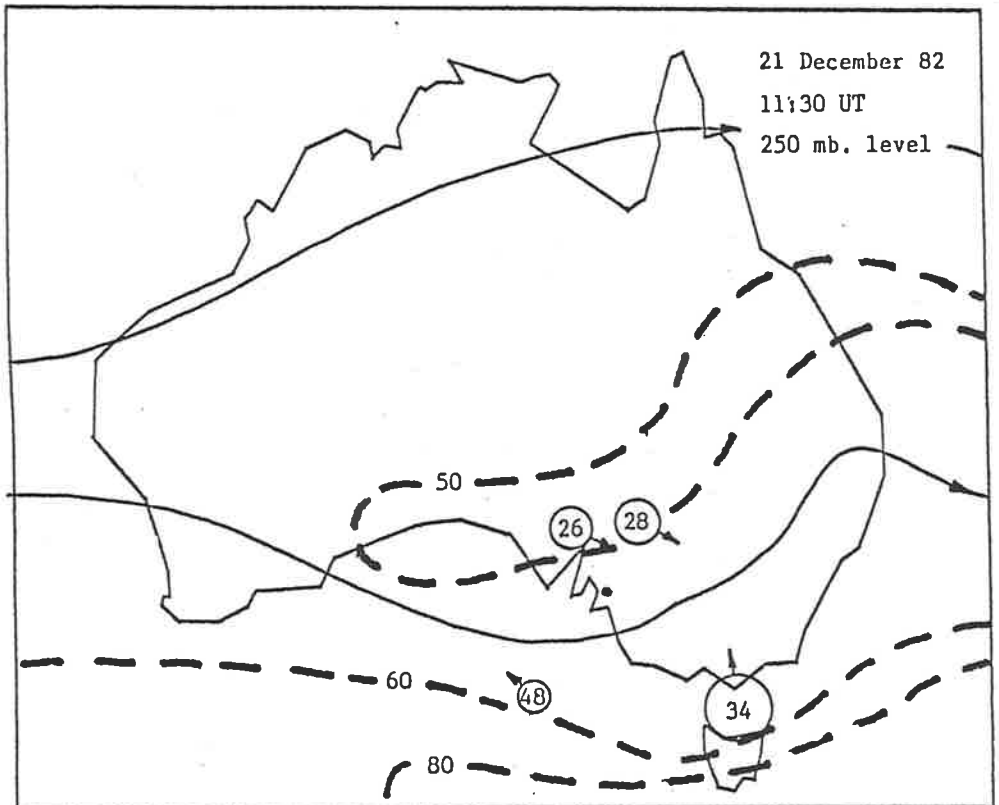

Period (min.)	Transit Time (min.)	Launch Time (UT)
48	110	11:30
34	140	11:00
28	120	12:00
26	140	11:10

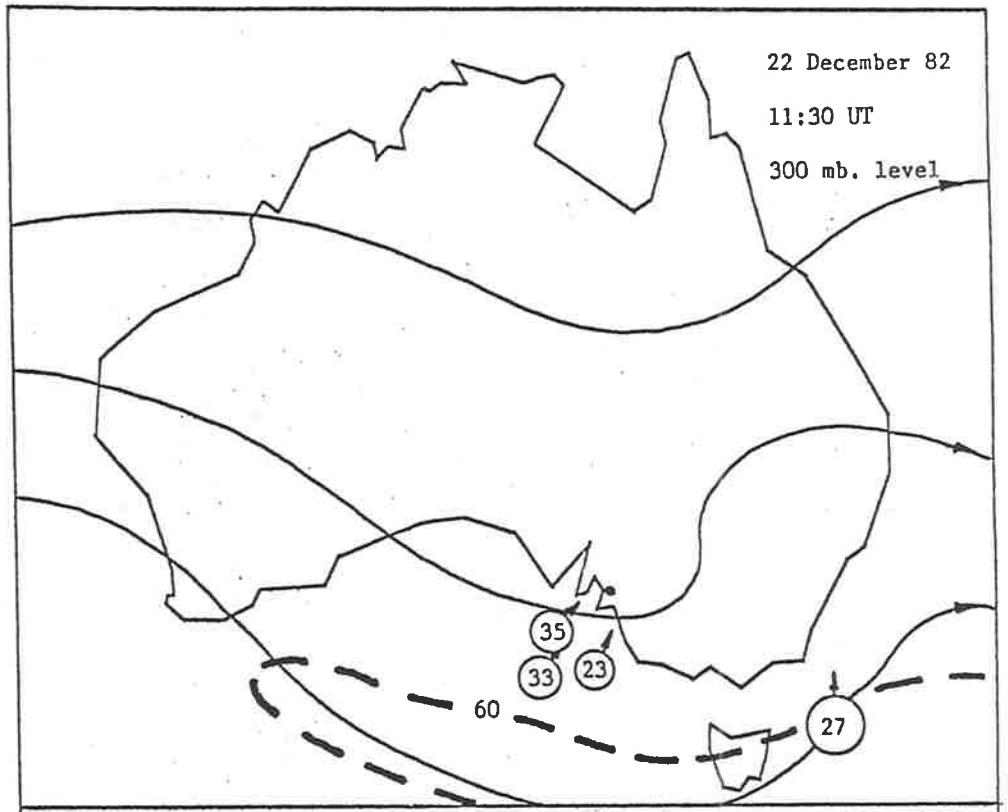

Period (min.)	Transit Time (min.)	Launch Time (UT)
35	70	12:20
33	80	12:30
27	200	8:00
23	50	13:00

Figure 5.5.1a Results of reverse ray tracing from 95km to 10 km.

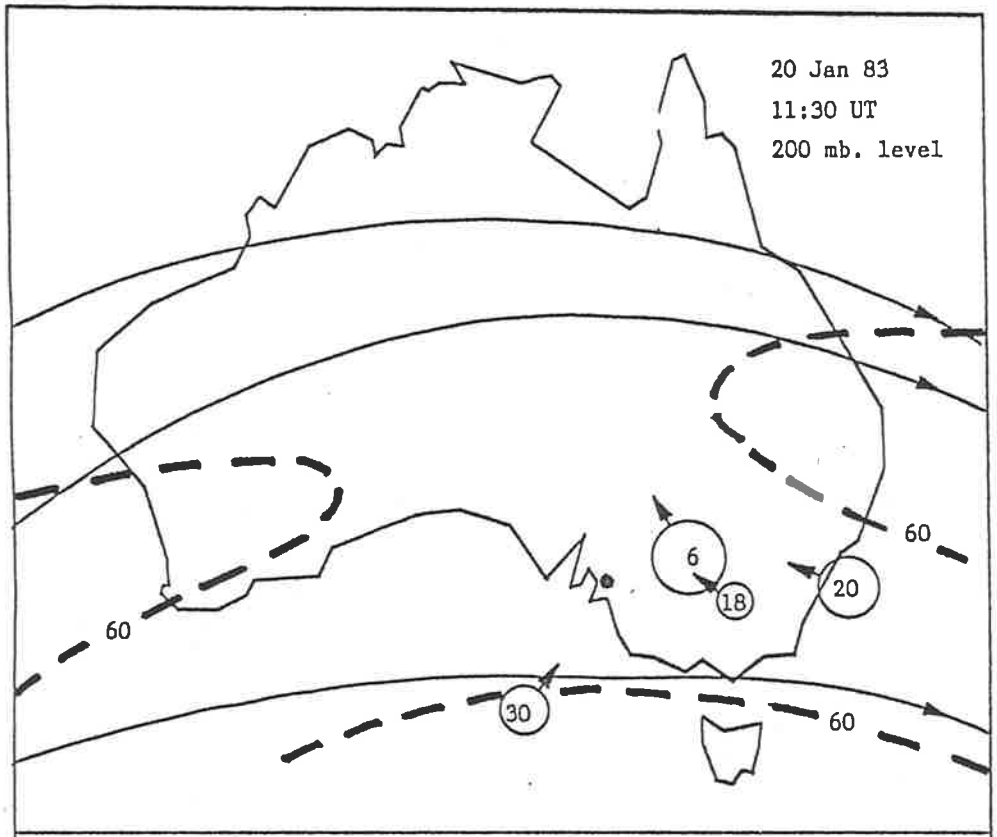

Period (min.)	Transit Time (min.)	Launch Time (UT)
30	220	12:50
20	350	9:00
18	130	11:00
6	120	12:50

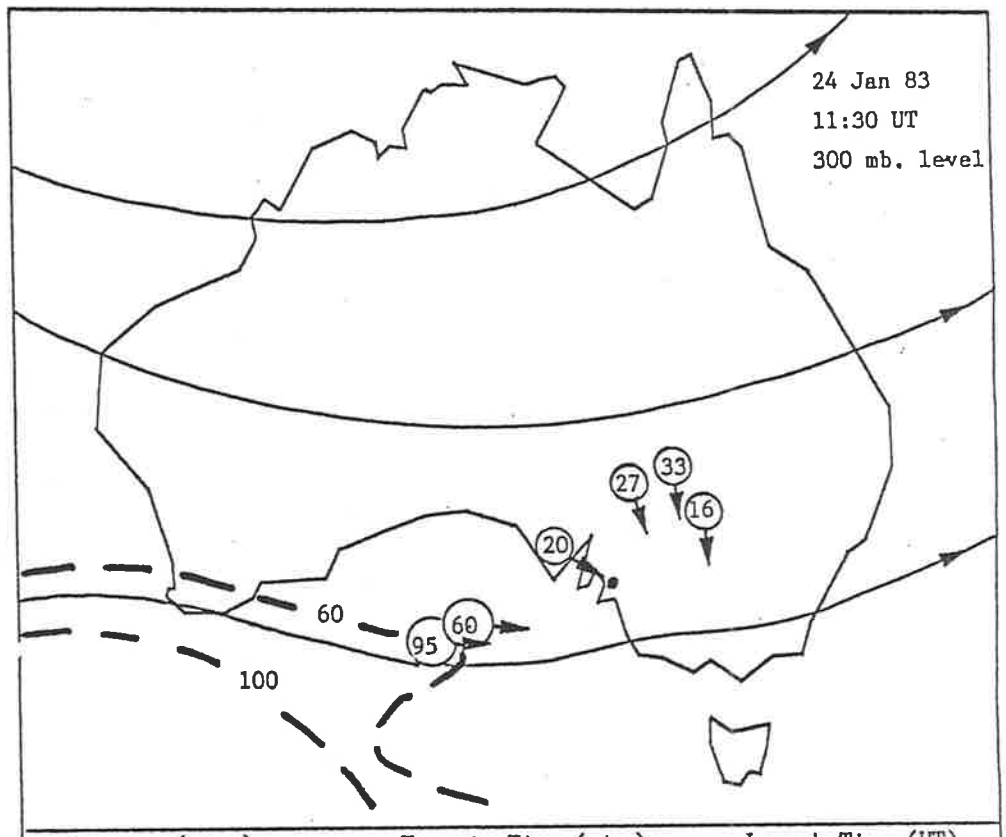

Period (min.)	Transit Time (min.)	Launch Time (UT)
95	180	11:10
60	150	10:40
33	170	10:40
27	110	11:40
20	40	12:50
16	130	10:50

Figure 5.5.1b Results of reverse ray tracing from 95 km to 10 km.

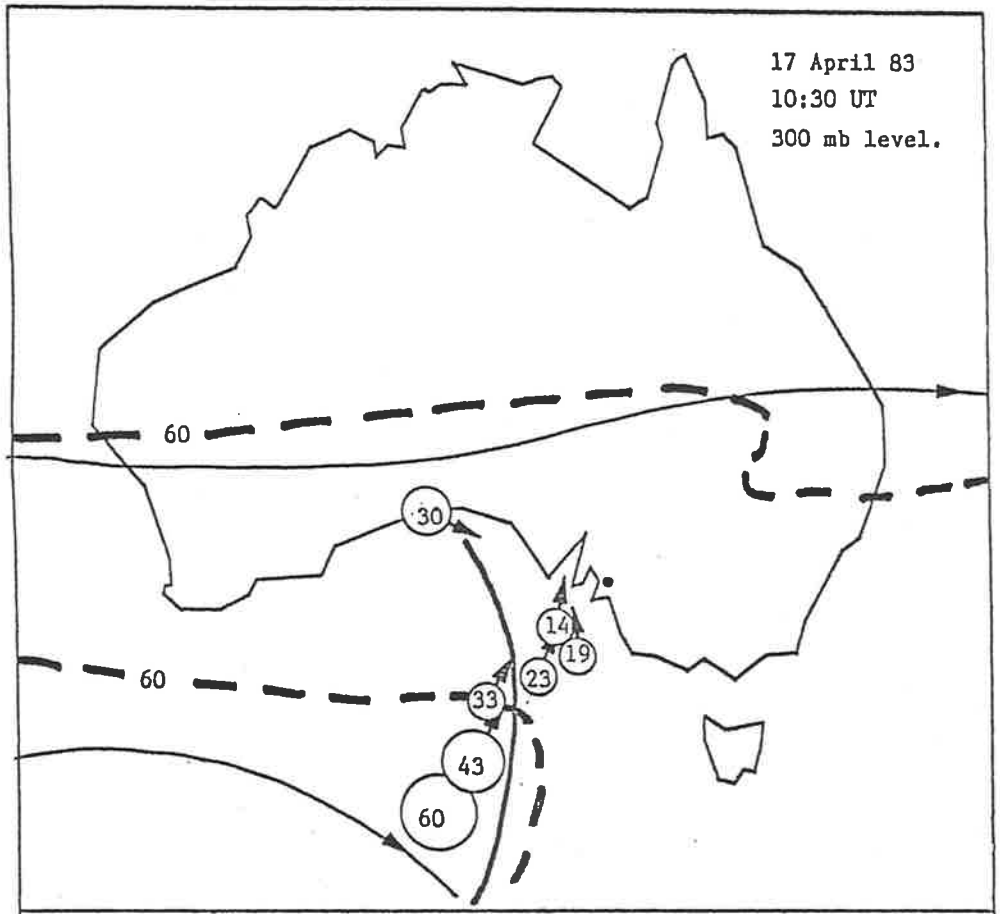

Period (min.)	Transit Time (min.)	Launch Time (UT)
60	200	10:40
43	160	11:30
33	80	11:10
30	80	9:40
23	60	11:30
19	70	12:40
14	30	12:00

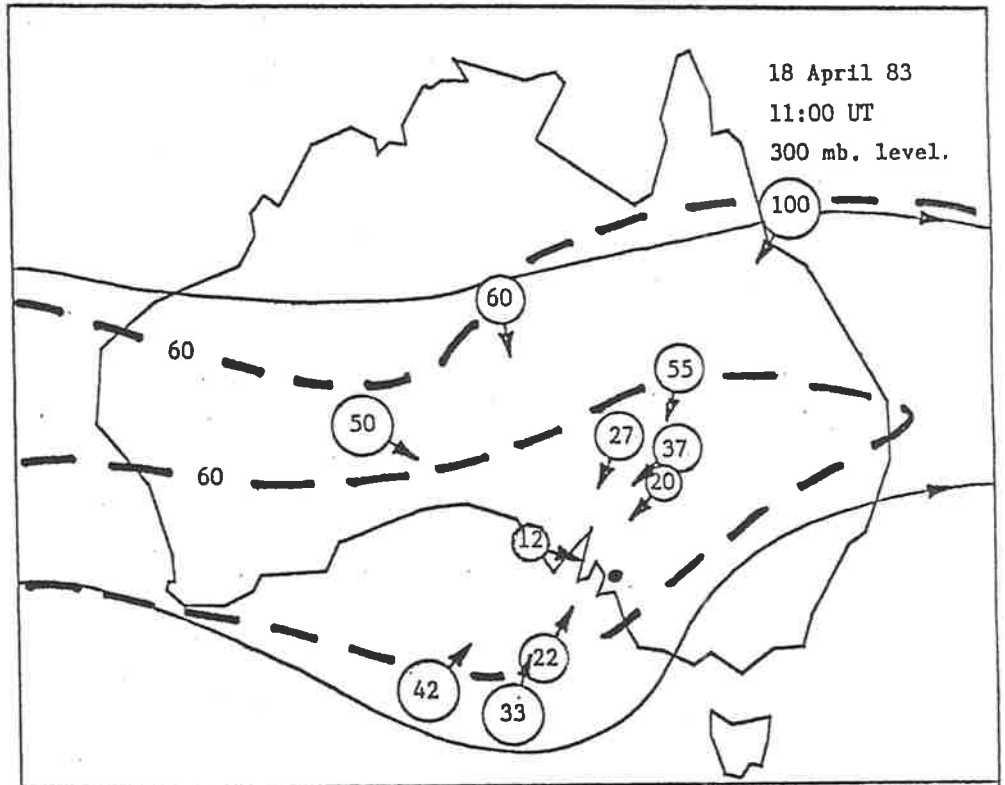

Period (min.)	Transit Time (min.)	Launch Time (UT)	Period (min.)	Transit Time (min.)	Launch Time (UT)
100	450	7:10	33	90	9:40
60	330	8:10	27	90	12:10
55	250	8:10	22	60	10:10
50	130	14:00	20	50	12:40
42	160	11:10	12	90	12:10
37	140	11:20			

Figure 5.5.1c Results of reverse ray tracing from 95 km to 10 km.

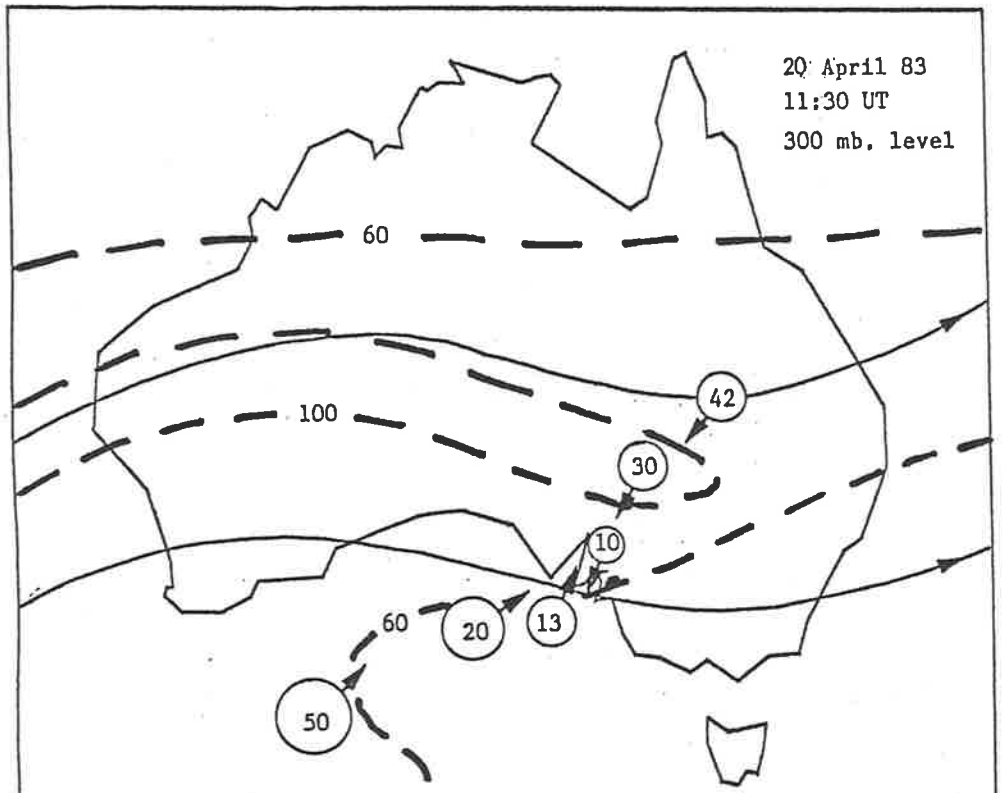

Period (min.)	Transit Time (min.)	Launch Time (UT)
50	300	7:30
30	180	11:00
42	100	12:40
20	50	13:30
13	100	13:40
10	80	12:40

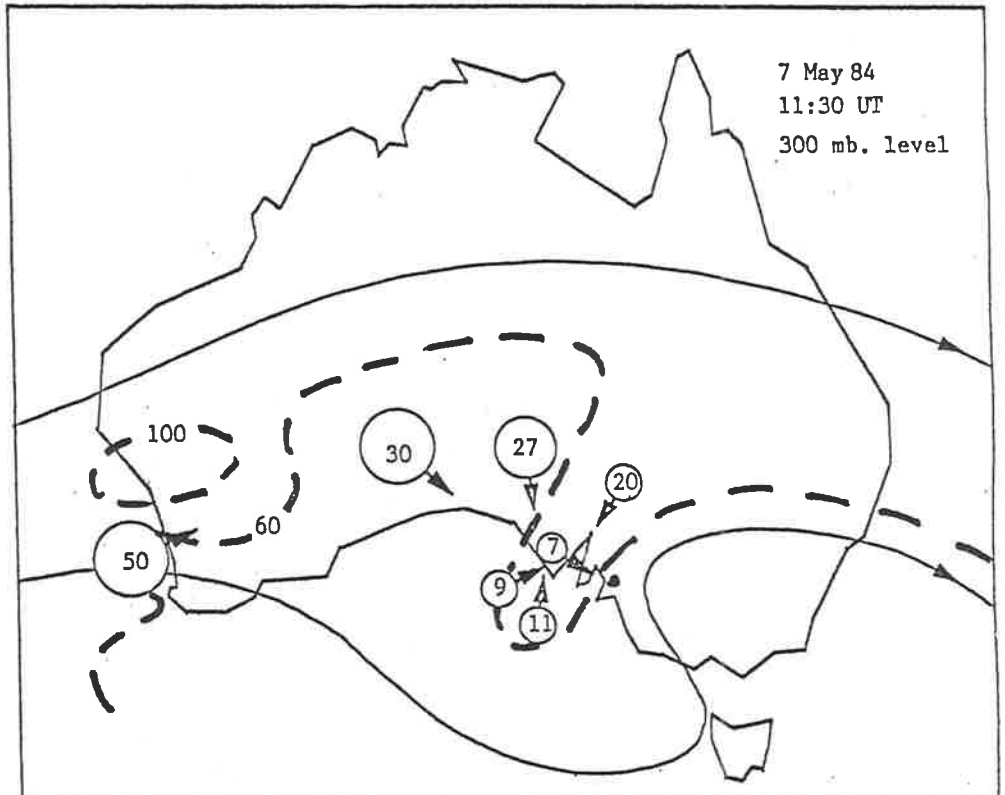

Period (min.)	Transit Time (min.)	Launch Time (UT)
50	280	7:20
30	160	9:40
27	100	12:30
20	40	12:30
11	60	13:00
9	90	11:50
7	20	12:50

Figure 5.5.1d Results of reverse ray tracing from 95 km to 10 km.

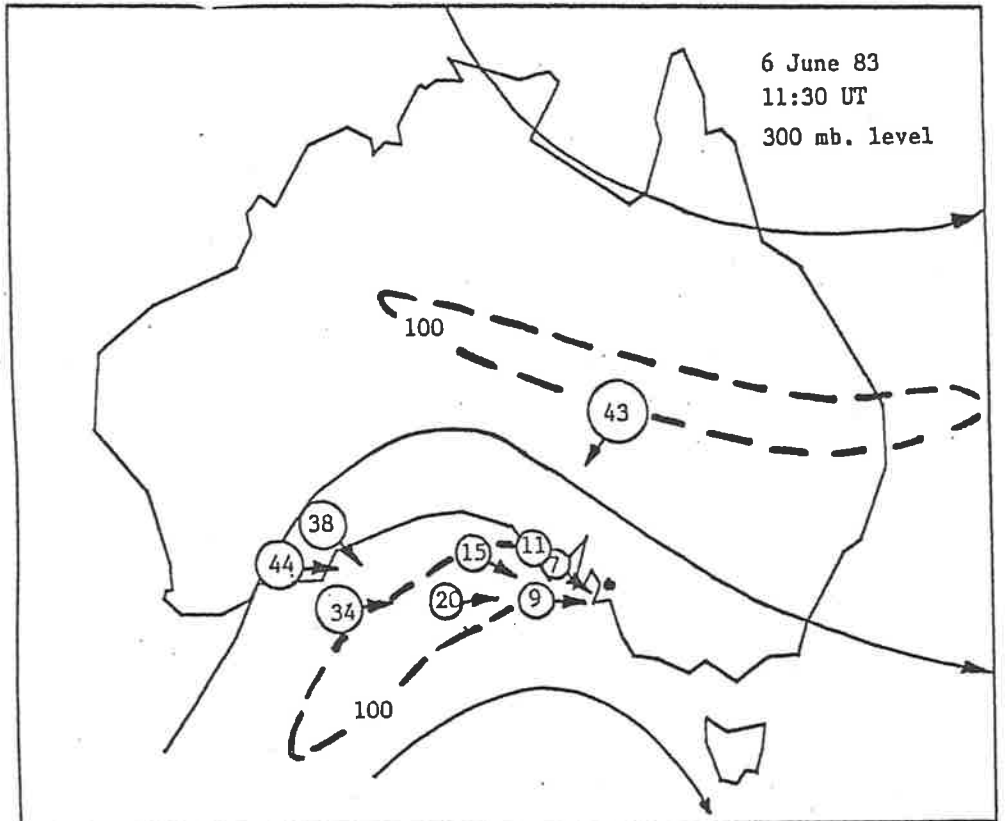

Period (min.)	Transit Time (min.)	Launch Time (UT).
44	140	12:00
43	120	13:20
38	120	12:20
34	120	12:20
20	80	14:00
15	40	15:00
11	30	11:00
9	30	15:30
7	60	13:20

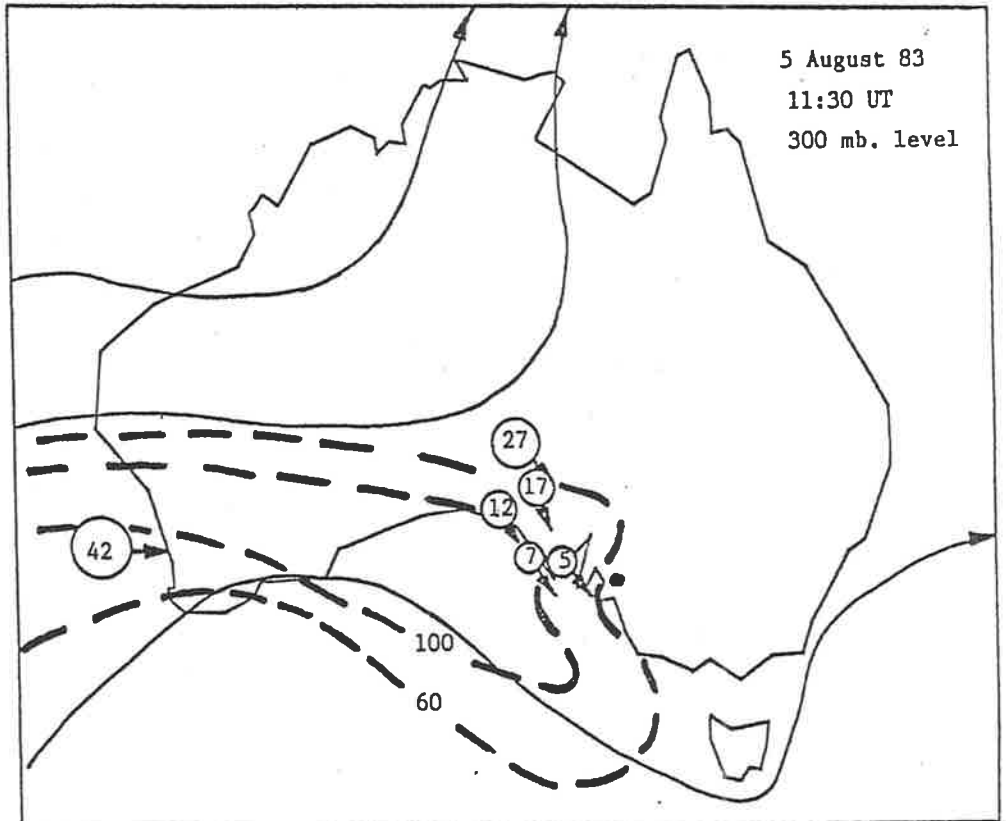

Period (min.)	Transit Time (min.)	Launch Time (UT)
42	350	8:30
27	100	10:50
17	60	13:30
12	80	14:10
7	50	11:40
5	40	14:20

Figure 5.5.1e Results of reverse ray tracing from 95 km to 10 km.

Also shown on the maps is the upper level wind activity typically at the 300 mb (~9 km) level. The upper level wind charts, supplied by the Adelaide Bureau of Meteorology, are inferred mainly from balloon measurements taken from meteorological sites scattered over the continent. Commercial airline flights provide additional information, although these are restricted to the high altitude flight paths, predominately between cities on the south west and east coasts. Polar satellite photographs of high altitude cloud movement also assist in the wind field analysis over the southern regions of Australia. The bold lines indicate the general direction of wind flow, which is predominately from west to east. Only a few lines have been included for clarity. The dashed lines are isotachs of jet streams, the speed of which is indicated in knots. Comparisons were made with meteorlogical surface and upper level isobaric weather maps and unless indicated, no significant frontal activity was present during the time periods of interest.

The upper level wind charts of figures (5.5.1) were recorded between 10:30 and 11:30 U.T. and chosen to coincide, as nearly as possible, to the observing period. The estimated launch time of the waves differ by up to a few hours either side of the wind recordings, so there may be some spacial differences between launch sites and any meteorological disturbances.

From the results presented, the reader may see that in most cases a reasonable association between the possible launch sites for the gravity waves and the position of jet streams can be made. Despite the temporal uncertainty, gravity waves appear to be launched in or near jet streams as opposed to areas far removed from jet stream activity. Contrary to this general trend is the night of 24 January 1983. Here definite wave generation to the north west of Adelaide is indicated, coinciding almost exactly with large localized thunderstorm activity as published by normal surface weather reports. Another night of particular interest is 17 April 1983. Although a jet stream is in the vicinity of the region of wave generation, so too is an upper level front. This front, taken from the 300 mb wind chart, lies to the south of Adelaide and is represented by the solid curve. The motion of this front is from west to east as is the order of wave generation indicated by the transit and launch times. This strongly indicates the front or the front-jet interaction as being the generating source of this wave field.

The direction of the normal to the wave front seems uncorrelated with the orientation of the jet streams, although such a statement should not be taken strictly due to the uncertainty of the exact position of the jet stream at the time of wave generation.

5.6. Discussion.

It is likely that certain kinds of severe weather can generate gravity waves in the troposphere which can propagate through the atmosphere and interact with the E region. Georges and Young, (1972) have associated gravity waves with thunderstorm activity, so too has Jordan (1972). The process of penatrative convection may be responsible for the generation of gravity waves from thunderstorms, whereby strong upward motion of air in a storm cell is incident on an upper level inversion. The upward displacement of the air parcel will be opposed by a restoring force due to the inherent stability of the inversion layer and an overshoot will result in a bouyancy oscillation of the layer. This process has been theoretically examined by Townsend (1966) and further experimental evidence of mesospheric waves generated by thunderstorms has been reported by Rottger (1977).

The association of gravity waves detected in the E and F regions with tropospheric frontal activity has been reported by Freund and Jacka (1979) and Bertin et al (1975). Jordan (1972) also attributes gravity wave sources to frontal activity with the additional observation of an increase in wave frequency with time as the front progresses. This can be observed for the night of 17 April 1983 where not only the launch sequence follows the path of the front but the observed period of the detected waves decreases as the front advances.

The exact mechanism by which a front may generate waves remains obscure. It is likely that waves are produced by wind shears accompanying moving squall lines generated when a cold front interacts with unstable air.

Large and medium scale gravity waves can propagate over considerable horizontal distances from the polar auroral regions, (Francis, 1975). The principle high latitude ionospheric source of these waves are Joule heating and Lorentz forces, (Chimonas and Hines, 1970) associated with the auroral electrojet and intense particle precipitation, (Hunsucker, 1982). The level of generation from these sources is typically 100 km, restricted in the vertical extent by 2-4 scale heights, constraining the vertical wavelengths, hence horizontal velocities of the generated waves. The dissipating effects of viscosity, heat conduction and Joule dissipation tend to filter out the slower moving, short period waves. Therefore, in order for waves generated at high latitudes to be detected at mid latitudes they would require periods greater than about 30 minutes and horizontal velocities of several hundred metres per second, (Richmond, 1978). For such waves, generated near 100 km at high latitudes, to be detected at 95 km at mid latitudes they must propagate almost horizontally. Upward propagating waves generated in the auroral regions, will continue in this direction with their ascent angle increasing with time. Downward propagating waves may be reflected upward when their phase velocity equals that of sound. Therefore downward

propagating waves with phase velocities less than 300 ms^{-1} may be deflected upwards at a level of about 70 km and be detected later at 95 km. From the data analysed, no such fast moving waves with periods greater than 30 minutes were observed, and only one instance where a wave with an observed period of 17 minutes and a horizontal phase velocity of 270 ms^{-1} was traced to a reflection at 75 km.

It seems that from the data considered here, the main source of tropospheric gravity waves can be attributed to jet streams. However, it should be pointed out that the results may be slightly biased towards jet streams since the method of observation requires clear weather. Local frontal and thunderstorm activity often imply poor observing conditions, whereas jet streams are largely a clear weather phenomena. Similar studies by Bertin et al, (1975) and Kersley and Rees, (1982), using radio techniques unaffected by cloud cover, show jet streams and frontal activity to contribute equally to wave generation for the cases they consider.

A realistic model for the production of gravity waves from regions of wind shear, in particular jet streams, is discussed by Mastrantonio et al, (1976). Here a vertical shear in the background wind is assumed to have superimposed on it an oscillating pertubation in the vertical velocity. The Richardson number of the flow is the main stability parameter and is defined as

$$R_i = \frac{N^2}{(du/dz)^2} \qquad (5.6.1.)$$

where du/dz is the vertical gradient of the horizontal wind. If $R_i > 0.25$ the system is stable, (Merril, 1977) so unstable modes correspond to $0 < R_i < 0.25$, with some of these modes able to propagate away from the regions of shear. Of these modes the minimum horizontal wavelength is about 25 km at a height of 10 km. For medium scale gravity waves with horizontal phase velocities about that of the velocity of the jet, say 40 ms^{-1}, this gives a lower limit to gravity wave periods of about 10 minutes which is consistent with the minimum periods observed for waves traced to the tropopause.

Typical values for the vertical wind profile can be estimated from equation (5.6.1). For waves to be generated by this mechanism,

$$(du/dz) > 2N \qquad (5.6.2.)$$

If the Vaisala Brunt period for the tropopause is taken to be 10 minutes then the minimum wind gradient necessary for the onset of instability corresponds to 20 ms^{-1} (40 knots) over a one kilometre height interval. Upper level wind charts at pressure levels of 250 mb (10 km) and 300 mb (9 km) show jet streams with typical wind gradients between 20 and 30 knots per kilometre, but it is by no means uncommon to identify regions of vertical wind gradient greater than 40 knots per kilometre.

Another gravity wave generation mechanism involves surface air blowing over mountain ranges to produce

mountain lee waves, (Gossard and Hooke, 1975). Waves detected above Mt. Torrens are unlikely to be associated with mountain lee waves due to the lack of any significant topography on the Australian continent. Other more exotic events have also been responsible for wave activity such as earthquakes, tsunamis, eclipses of the sun, cyclones, nuclear explosions etc. but, fortunately, none of these were reported around the times of observation.

Chapter 6. Gravity Wave Power Spectra.

6.1. Introduction.

The energy spectra of gravity waves in the mesosphere seem to show some degree of universality. Results of radio partial reflection techniques for measurement of zonal and meridonal wind components of gravity waves, taken from Vincent, (1984) are shown in figure (6.1.1). These mean spectra, with the diurnal and semidiurnal tides removed, are taken from three locations, two in Australia, Adelaide (35°S, 138°E) and Townsville (19°S, 147°E) by Vincent and Ball (1981) and the other at Poker Flat (65°N, 147°W) in Alaska by Carter and Balsley (1982). As can be seen, very similar spectral slopes are maintained throughout the gravity wave range extending from the inertial period, beyond which no gravity waves exist, to the Vaisala Brunt period with a spectral index, k = 1.5 to 1.6. Note the log-log format implies the energy density for the gravity wave region takes the form of a power law

$$E(\omega) = c\omega^{-k} \qquad (6.1.1)$$

where c is a constant and k the spectral index.

6.2. Recorded spectra.

Power spectra for each of the three fields of the photometer were computed using a fast Fourier transform routine over the entire data length. Prior to

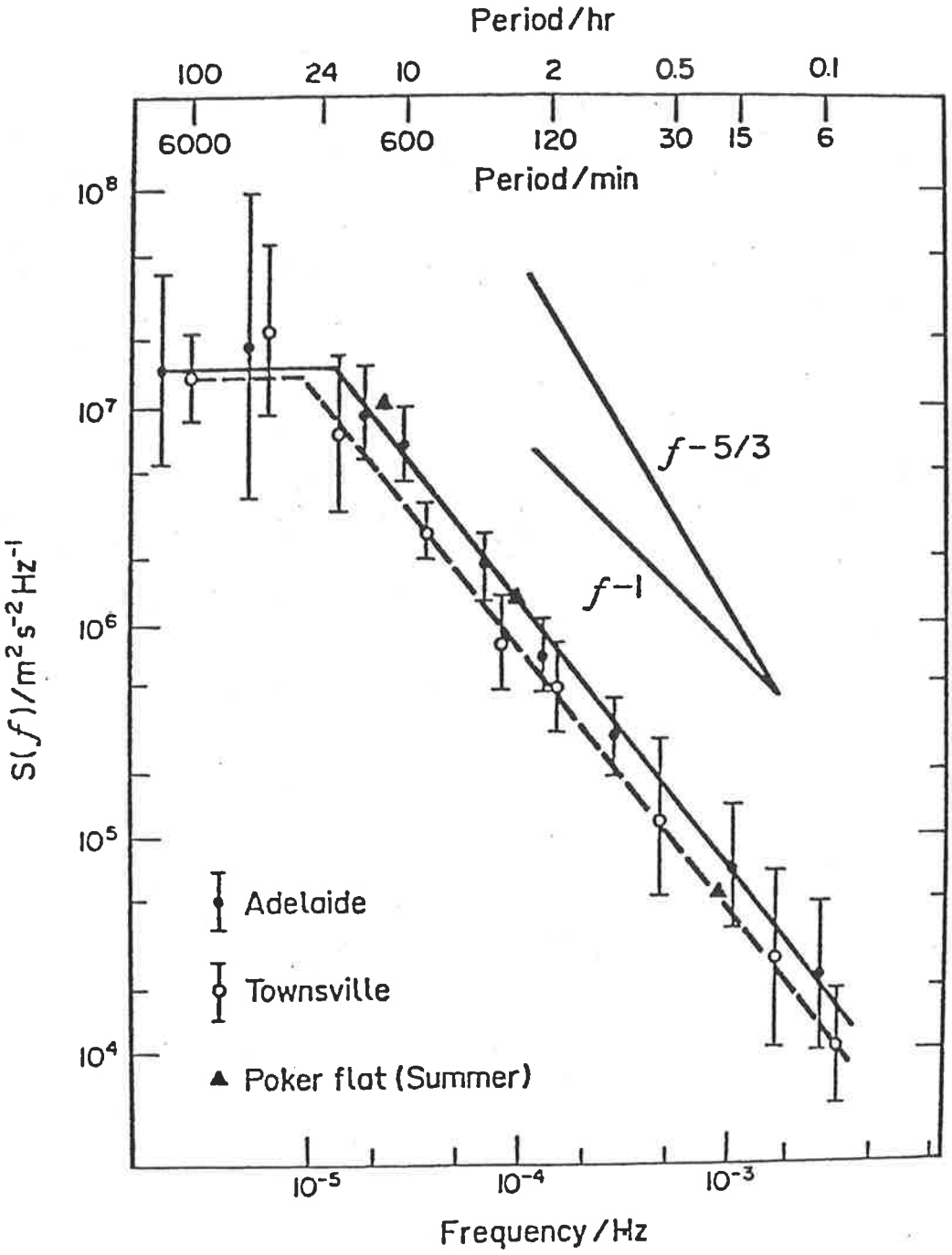

Figure 6.1.1. Seasonally averaged spectral densities for horizontal wind fluctuations observed at a height of 85 km at Adelaide and Townsville. The spectra are the average of the zonal and meridional spectra and the bars indicate the range of the individual spectra. ▲ Show spectral densities of wind motions observed at Poker Flat. Taken from Vincent, (1984)

transformation, the data mean and any linear trend were removed and the data treated with a cosine taper as discussed in §4.3. The transform of the time series, X(t) from field m, can be written as the sum of the real and imaginary parts

$$X_m(t) \xleftrightarrow{FFT} A_m(f) + jB_m(f) \qquad (6.2.1.)$$

The power spectrum is then defined as

$$P(f) = [\ A_m^2(f) + B_m^2(f)\ ]$$

where P(f) has the arbitary units of [intensity]^2. To plot the power spectra against frequency in Hertz, it was multiplied by the square of the sampling interval in seconds. To increase the reliability, the spectra of all three field were averaged.

Two typical examples of the recorded λ557.7 nm intensity fluctuations are shown in figures (6.2.1). Apart from spectral peaks, these graphs can be analysed into two components. The first is a linear decrease in power with increase in frequency, with a spectral index of around 1.6, consistent with the spectra of mesospheric wind pertubations caused by gravity waves. The other is a constant power level, maintained by frequencies greater than the Vaisala Brunt frequency, indicated by the small arrow and taken to be 4.6 minutes at 95 km. This spectral flattening is to be expected beyond the Vaisala Brunt

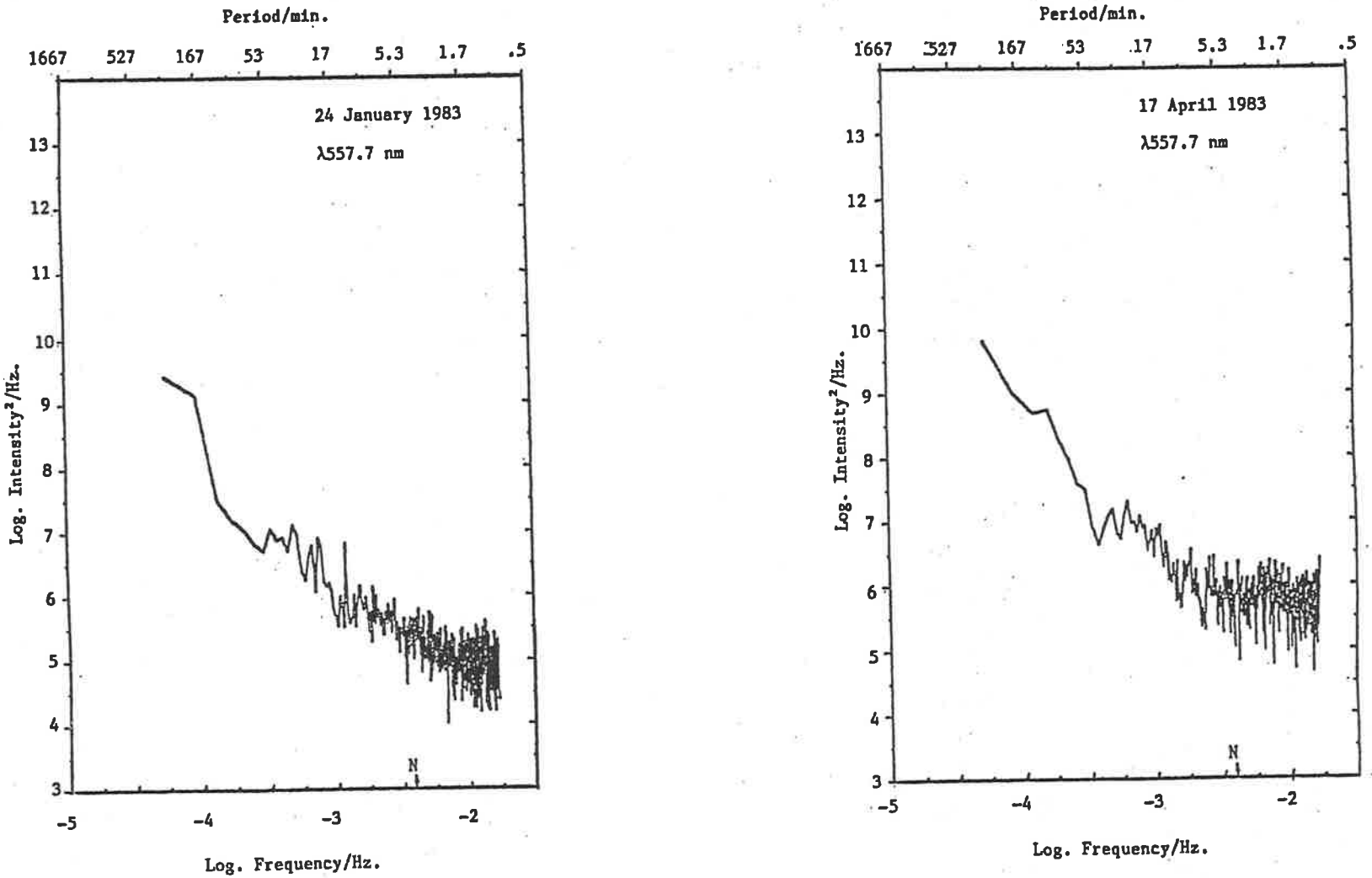

Figure 6.2.1. Examples of 3FP power spectra. The Vaisala Brunt cut off frequency is indicated by N.

frequency due to the absence of gravity waves. Although this cut off coincides well for the spectrum of 17 April 1983, it is displaced to higher frequencies for the night of 24 January 1983. This displacement may be caused by the effect of the background winds Doppler shifting the wave spectrum to shorter periods relative to a ground based observer. This explanation is consistent with the mean wind being somewhat larger at 95 km in December than April.

The signal measured by the 3FP is the integrated intensity of the emission line and the background continuum at λ557.7 nm. This will result in a spectrum made up of the following components-

a) The airglow emission line fluctuation due to the passage of a gravity wave field across the fields of view of the photometer. This is expected to show the general power law trend for gravity waves with a sharp cut off at frequencies greater than the Vaisala Brunt frequency. A component also may be contributed from fluctuations in the emission line caused by turbulence and carried by the neutral wind at the emission level. Let these components be represented by P_{557}

b) The background continuum at λ557.7 nm will fluctuate due to scattering of man made and natural light from aerosols, dust etc. in the lower atmosphere; that is, from altitudes less than a few kilometres. This is expected to show a similar spectral index, (Larson et al, 1982). Let this component be P_b.

c) The third contribution is due to Poisson noise from statistical fluctuations of all of the above sources. Naturally, this noise will give rise to a constant power level across the entire frequency range and will be represented by N_{557} and N_b.

The recorded spectrum can then be expressed as

$$R = P_{557} + P_b + N_{557} + N_b \qquad (6.2.3.)$$

6.3. Scaling.

Simultaneously run with the λ557.7 nm filter were two background filters centred at λ500 nm and λ530 nm, corresponding to areas in the nightglow spectrum where little emission is found, (Broadfoot and Kendall, 1968). In order to estimate the true gravity wave power spectrum, P_{557}, the background spectrum was estimated using the spectra from these filters. For this estimation the different effects of photomultiplier spectral responses, filter characteristics and signal sources at the different wavelengths must be considered.

The signal measured by the photometer is given by

$$S = K \int q(\lambda)\, T(\lambda)\, I(\lambda).d\lambda$$

where

K = instrument constant including optics losses, counting, data logging etc. considered constant for all filters.

q = photomultiplier quantum efficiency

T = filter transmission

I = source intensity

To a good approximation, $q(\lambda)$ and $I(\lambda)$ are constant over the filter bandwidth, therefore the ratio of the signal at λ and background is

$$S_\lambda / S_b = \frac{q_\lambda I_\lambda A_\lambda}{q_b I_b A_b} \qquad (6.3.2.)$$

where, for filter i

$$A_i = \int T_i(\lambda).d\lambda \qquad (6.3.3.)$$

The intergrated filter transmission, A_i was measured for each filter using the monochromator and a technique similar to that of filter calibration discussed in §3.4. Over the filter bandwidths, the nightglow background spectrum is nearly equal for all three filters, (Broadfoot and Kendall, 1968). From the quantum efficiencies quoted in §3.3, a scaling factor was assigned to normalize observations at the emission and background wavelengths.

6.4. Noise spectra.

The statistical variations of the nightglow and background spectra are distributed as a Poisson variate. An estimate of this statistical noise was generated using a standard computer routine to give time series with variance equal to the mean emission line and background

signals. The effect of instrument acquisition time jitter, determined to be less than 1%, and the rounding effects of scaling were included in the generation of the noise series. The noise spectra were then calculated using exactly the same process as the real data to give N_{557} and N_b.

6.5. Background spectra.

For convenience the estimate of the background spectrum is best represented as a smooth curve. As mentioned in §6.2, this spectrum is considered to obey some power law with a constant noise level

$$B = P_b + N_b \quad \text{where} \quad P_b = c_b \omega^{-k_b} \qquad (6.5.1.)$$

Because of this power relation, to average P_b would introduce large bias at the lower frequencies so an average of log B is taken over equal intervals of log ω to reduce this bias, since log B against log ω is nearly linear. The antilog is then taken to give the mean recorded background spectrum $\overline{B}$ from which the background noise is subtracted giving $\overline{P}_b = \overline{B} - \overline{N}_b$. To log $\overline{P}_b$, a straight line is fitted and from this line of best fit the power law parameters, c_b and k_b are determined and an estimate for the mean background power, $\langle \overline{P}_b \rangle$, is calculated. To this the generated noise spectra for the background and emission lines are added giving

$$\langle \overline{R}_b \rangle = \langle \overline{P}_b \rangle + \overline{N}_{557} + \overline{N}_b \qquad (6.5.2.)$$

This estimate of the mean recorded background can then be compared visually with the recorded emission spectrum, the difference indicating the gravity wave spectrum, i.e.

$$P_{557} = R - \langle \overline{R}_b \rangle$$

6.6. Discussion.

A comparison between the recorded spectrum at λ557.7 nm and the smooth background spectrum can be seen in figure (6.6.1). For frequencies less than the Vaisala Brunt the λ557.7 nm spectrum shows, on average, greater power than the estimated power of the background at λ557.7 nm. This is to be expected if fluctuations in the emission line, caused by gravity waves, are much larger than any background fluctuations. For frequencies greater than the Vaisala Brunt cut off the two spectra merge. Here gravity wave activity is absent and both spectra are dominated by noise.

The spectral index of the gravity wave spectrum is affected only slightly by the background since they are of very nearly the same slope with the mean value of the gravity wave power typically an order of magnitude above that of the background for frequencies less than the Vaisala Brunt. The mean spectral index is k = 1.7 which compares favourably with that of Vincent (1984) and Balsley and Carter (1982). The effect of the background spectrum, although small, will tend to increase this slightly.

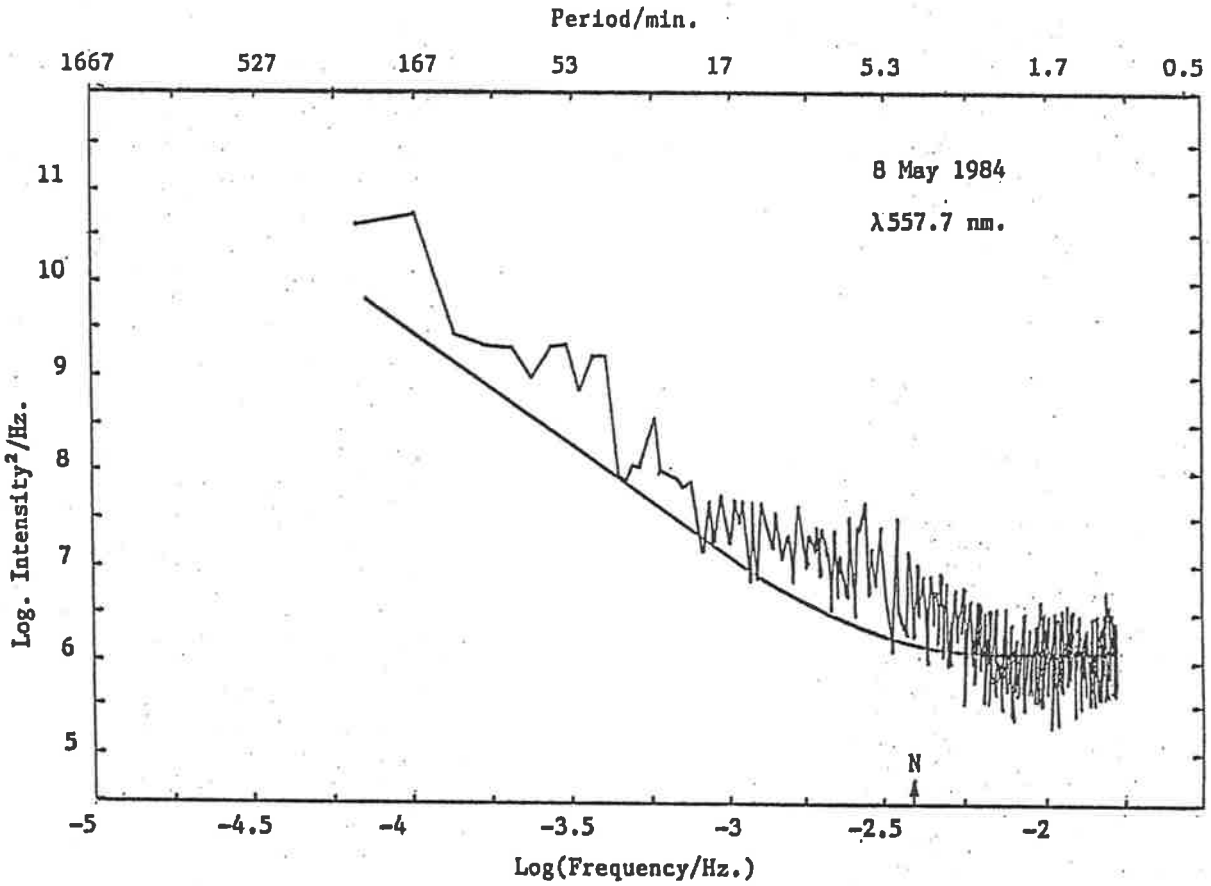

Figure 6.6.1. Comparison between a typical recorded power spectrum, averaged over all three fields, and the estimated background spectrum shown by the smooth curve.

Chapter 7. Gravity Wave Energy Flux.

7.1. The dispersion diagram.

Recalling the dispersion equation (2.2.5)

$$k_z^2 = \left(\frac{N^2 - \Omega^2}{\Omega^2 - f^2}\right) k_h^2 - \left(\frac{N_A^2 - \Omega^2}{C^2}\right) \qquad (7.1.1.)$$

Following the discussion of §2.3, the dispersion equation for gravity waves gives a family of hyperbolae. The dispersion contours of selected wave periods are illustrated in figure (7.1.1). Here the vertical coordinate is taken to be $-k_z$, increasing upwards, in order to show those gravity wave modes whose energy flow is upward. The values of N, N_A and C were chosen such that the diagram corresponds to the 95 km level. Points plotted on the diagram represent waves detected by the 3FP and verified by the analysis procedure. The k_h position of each point on the diagram is determined from the observed horizontal phase velocity and the intrinsic frequency. This is estimated from the observed wave frequency and an estimate of the wind vector at 95 km using equation (2.4.2) and the wind profiles of figures (5.3.1). The k_z position is calculated directly from equation (7.1.1).

The vertical line at λ_h=26 km indicates an instrument limitation of the photometer. Since field spacings are 13 km, then horizontal wavelengths less than twice this spacing become ambiguous and are rejected by the analysis criteria.

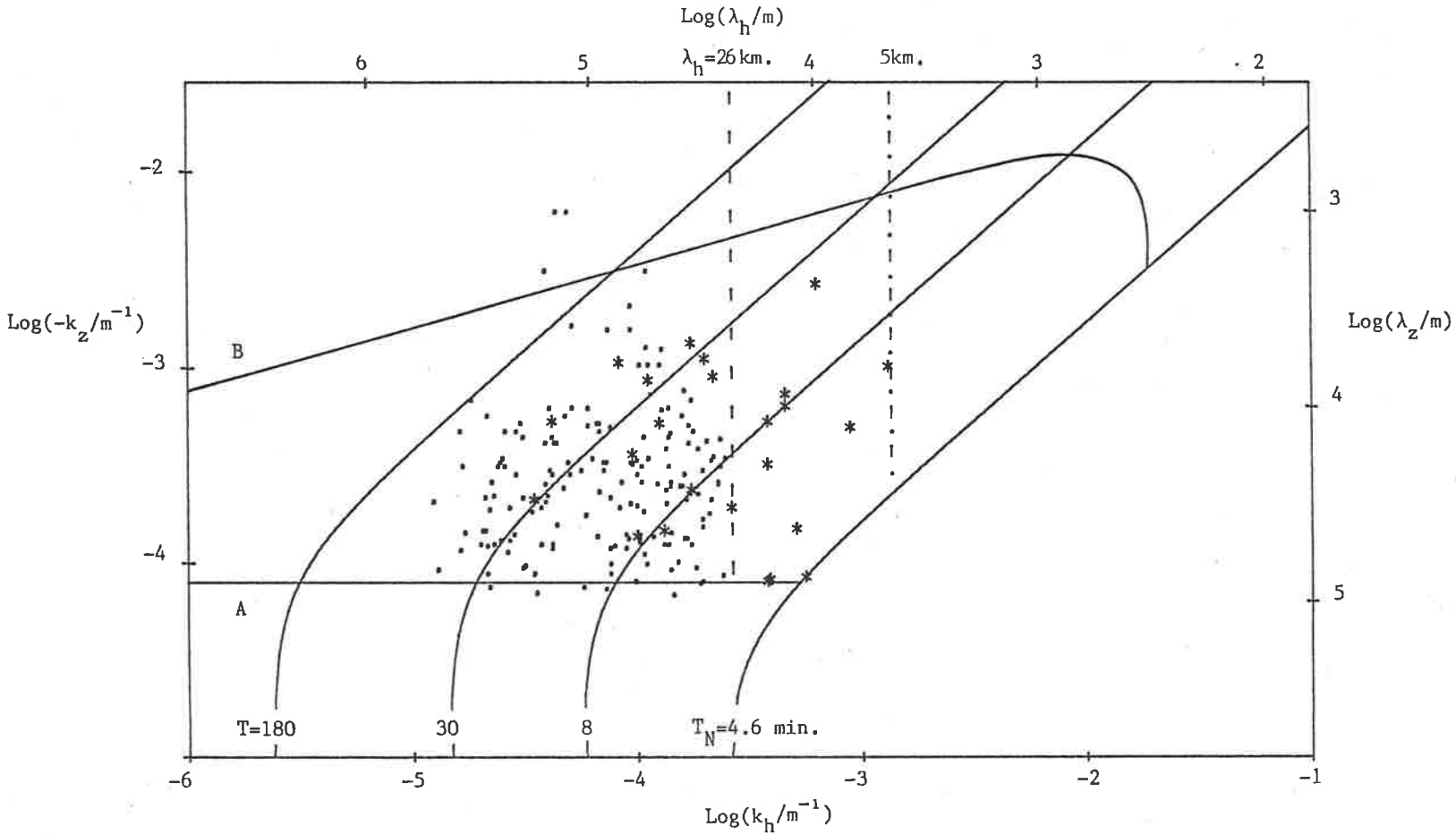

Figure 7.1.1. Dispersion diagram presenting selected constant period contours for gravity waves at 95 km. Plotted are observed wave parameters for 3FP measurements with reduced field data indicated by asterisks. Instrumental limitations are depicted by broken lines at λ_h = 25 km and 5 km. The theoretical limits due to reflection and dissipation are shown by A and B respectively.

To confirm this, two nights of data were recorded with each field divided into three subfields having spacings of 2.5 km. This was done using three λ557.7 nm interference filters spaced at 120 degrees in the filter wheel. Each filter was masked such that the field stop was now defined as a small circular off axis aperature. The aperatures on each filter were identical but relatively displaced at 120 degree intervals. As the filter wheel is rotated, this new system now defines three groups of three fields, each group spaced 13 km and the spacing within each group 2.5 km. Waves detected from this arrangement are shown by asterisks with the cut off wavelength now at λ_h=5 km.

Because photometer observations are limited to night time, with typical data lengths of about eight hours, then measurements of periods greater than about four hours become unreliable, therefore detected waves with periods greater than this are rare.

In an isothermal atmosphere, a lower limit to the vertical wave number exists. This is indicated by the horizontal boundary A . Waves propagating from lower altitudes will be reflected if, at any stage along their path, $k_z^2 < 0$. As discussed in §2.4, this will occur if the horizontal phase velocity exceeds CN/N_A. This value has a minimum in the middle atmosphere of about 170 ms^{-1} at about 80 km, (Gossard and Hooke, 1975), therefore waves propagating from below with intrinsic horizontal phase speeds exceeding this value are unable to reach the 95 km level, (Hines, 1960).

As would be expected, this demarcation lies on the elbow of the hyperbola, as only small increases in the horizontal phase speed will result in a very rapid decrease of k_z. The good agreement of the observed waves lying above this boundary reinforces the argument that the waves detected originate from below 80 km.

For waves with periods close to the Vaisala Brunt cut off period, T_N, another boundary occurs corresponding to the minimum Vaisala Brunt period. In the middle atmosphere the maximum value for T_N is about 8 minutes at 60 km, (Gossard and Hooke, 1975). Therefore, for a stationary atmosphere, waves incident at the 60 km level from below with period shorter than 8 minutes will be reflected. However, figure (7.1.1) shows waves detected at 95 km with periods less than 8 minutes. The reason for this apparent contradiction may be resolved by realizing that the atmosphere is not stationary. The middle atmosphere zonal wind profile peaks at about 60 km, so wave periods can be Doppler shifted to greater than 8 minutes and escape reflection. The wind reversal above 60 km enables these waves to be shifted back to shorter periods to be detected at 95 km. Naturally no waves are detected with periods shorter than 4.6 minutes, the Vaisala Brunt period at 95 km.

The final boundary, labelled B in figure (7.1.1), results from the dissipation of gravity wave energy by the atmosphere. The effect of molecular viscosity can be treated by introducing the appropriate stress tensor in the force equation (2.2.2).

Thermal conduction can be expressed by modifing the equation of energy, (2.2.3) to include heat conduction with the introduction of an additional heat flow equation. The solution of these extensions is not justified for the following discussion. Instead a simpler approach is adopted, following that of Hines, (1960). Here only viscous effects are considered which are normally comparable to those of thermal conduction, (Pitteway and Hines, 1963). The mean rate of dissipation per unit mass in the asymptotic limit is

$$\overline{R} \simeq \frac{\eta(k_h^2 + k_z^2)\ VV^*}{2k_z^2} \qquad (7.1.2.)$$

where η is the kinematic viscosity and V^* the complex conjugate of the horizontal velocity perturbation induced by the gravity wave. The mean energy content per unit mass, averaged over one wave cycle is then

$$\overline{E} \simeq \frac{N^2 k_h^2\ VV^*}{2k_z^2\ \Omega^2} \qquad (7.1.3.)$$

For a gravity wave to be dissipated over one cycle then

$$T\overline{R} = \overline{E} \qquad (7.1.4.)$$

with T the period of the gravity wave. This represents maximum dissipation and can be considered as representing an upper limit to viscous dissipation but perhaps a reasonable value if thermal conduction were to be included.

In the asymptotic region of the dispersion diagram where relatively small scale sizes are considered, it is useful to approximate the dispersion equation to

$$\Omega^2 k_z^2 = (N^2 - \Omega^2)k_h^2 \qquad (7.1.5.)$$

where $f^2 << \Omega^2$ and $k_z^2 >> N_A^2/C^2$, (Hines, 1960). Using this asymptotic approximation and combining equations (7.1.2) and (7.1.3) into (7.1.4) gives,

$$2\pi\eta k_h^2 = \Omega^3 \qquad (7.1.6.)$$

which has been plotted as the viscous dissipation boundary B using $\eta = 10\ m^2 s^{-1}$ as the kinematic viscosity at the 95 km level, (U.S. Standard Atmosphere, 1976). Waves appearing above this boundary would be severely attenuated at lower levels. Since kinematic viscosity decreases with height much more rapidly than changes in N, then the position of the viscous boundary moves upward with decreasing height. In general for waves propagating upward through the atmosphere, those of the smaller scales are dissipated first.

How much energy is transported from the lower to the upper atmosphere by these waves? What follows is a unique procedure for the estimation of the vertical energy flux of these waves at the 95 km level from the 3FP observations. Although the method may seem indirect, with many assumptions and approximations, the end results are

quite consistent with those of other workers using entirely different techniques.

7.2. Energy density.

The mean energy per unit volume of a stationary, isothermal atmosphere due to a gravity wave perturbation is given by,

$$\overline{E} = \tfrac{1}{2}\rho_o(\overline{V}^2 + N^2\overline{\zeta}^2) \qquad (7.2.1.)$$

where ρ_o is the unperturbed atmospheric density, $\overline{V}^2$ is the mean square deviation of the horizontal velocity perturbation and $\overline{\zeta}^2$, the mean square vertical displacement perturbation, (Gossard and Hooke, 1975), where

$$\overline{\zeta}^2 = \frac{k_h^2\,\overline{V}^2}{k_z^2\,(\Omega^2 + f^2)} \qquad (7.2.2.)$$

At frequencies where $\Omega^2 >> f^2$ the energy density is equally partitioned between potential energy and kinetic energy. The last term in equation (7.2.1), upon substituting equation (7.2.2), gives the wave energy content quoted by Hines (1960) in equation (7.1.3) for the asymptotic limit. At lower frequencies, approaching the intertial frequency, the wave motion is nearly horizontal, hence energy is predominately kinetic with the density reducing to $\tfrac{1}{2}\rho_o\overline{V}^2$. The energy density can therefore be written

$$\overline{E} = \tfrac{1}{2}\rho_o\,\overline{V}^2\left(1 + \frac{k_h^2}{k_z^2}\frac{N^2}{(\Omega^2 + f^2)}\right) \qquad (7.2.3.)$$

For the dispersion diagram presented in figure (7.1.1), the observed waves can be seen to lie in the asymptotic region because of the selective filtering of the middle atmosphere. Using the asymptotic approximation, the mean square fractional density perturbation of the atmosphere caused by the passage of a gravity wave can be related by, (Vincent, 1984)

$$\overline{\left(\frac{\rho}{\rho_o}\right)^2} = \frac{N^2}{g^2}\left(\frac{\Omega^2 - f^2}{\Omega^2 + f^2}\right)\overline{V}^2 \qquad (7.2.4.)$$

Assuming a sinusoidal fluctuation in the density perturbation then from the discussion of §2.5, this can be expressed as a function of the intensity perturbation of the λ557.7 nm nightglow emission.

$$\overline{\left(\frac{\rho}{\rho_o}\right)^2} = \beta^2 \overline{\left(\frac{Q}{Q_o}\right)^2} \qquad (7.2.5.)$$

By definition, for the population, Q_i/Q_o of N samples is given by

$$\overline{\left(\frac{Q_i}{Q_o}\right)^2} = \frac{1}{N-1}\sum (Q_i/Q_o - 1)^2$$

$$= \frac{1}{(N-1)Q_o^2}\sum (Q_i - Q_o)^2$$

$$= \frac{\overline{Q_i^2}}{Q_o^2}$$

so equation (7.2.5.) becomes $\overline{\left(\frac{\rho}{\rho_o}\right)^2} = \beta^2\frac{\overline{Q^2}}{Q_o^2}$ (7.2.6.)

$\overline{Q^2}$ being the variance of the intensity oscillation about some mean level Q_o.

Consolidating the discussion reveals that substitution of equation (7.2.6) into (7.2.4), and (7.2.4) into (7.2.3) gives

$$\overline{E} = \tfrac{1}{2}\rho_o \beta^2 \frac{g^2}{N^2} \frac{\overline{Q^2}}{Q_o^2} \frac{(\Omega^2+f^2)}{(\Omega^2-f^2)} \left\{ 1+\frac{k_h^2}{k_z^2} \frac{N^2}{(\Omega^2+f^2)} \right\} \qquad (7.2.7.)$$

An estimate of $(\overline{Q^2}/Q_o^2)$ can be realized from the power spectra of the data since $\overline{Q^2}$, the variance, is the area under the power spectrum for that frequency interval. Let the average value of the emission intensity, over the recorded data interval be $\overline{Q}$, measured from zero intensity. If the average value of the background at the emission wavelength is $\overline{Q_b}$ then

$$Q_o = \overline{Q} - \overline{Q_b} \qquad (7.2.8.)$$

The mean emission intensity, $\overline{Q}$ can be simply obtained by averaging the λ557.7 nm emission over the record length. The value for $\overline{Q_b}$ was estimated from the background emissions using the techinque discribed in §6.3. That is, although the background emissions are measured by different filters displaced from the wavelength of interest, $\overline{Q_b}$ was estimated using suitable scaling factors determined from the alignment of the recorded spectrum, R and the estimated background spectrum $\langle\overline{R_b}\rangle$.

For each detected wave, the energy density was calculated using equation (7.2.7). Examples of the energy density of waves recorded from two nights can be seen in figure (7.2.1).

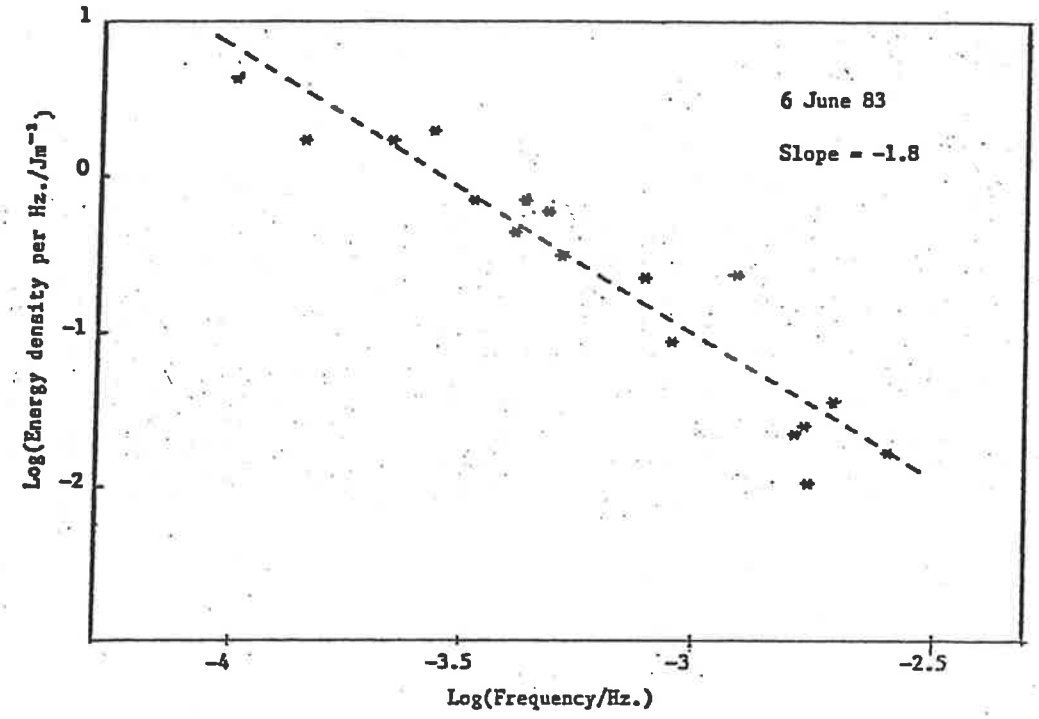

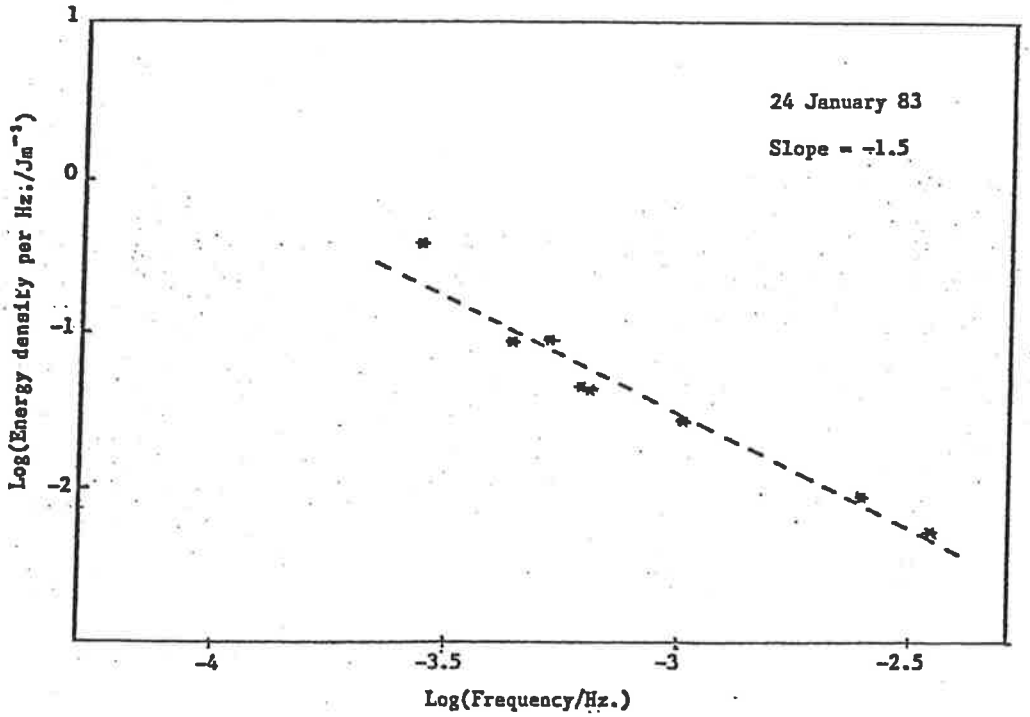

Figure 7.2.1. Typical examples of gravity wave energy density spectra at 95 km. Values were calculated from intensity fluctuations of the λ557.7 nm nightglow.

The points fit well to straight lines, with slopes of -1.8 and -1.5. This is to be expected for the energy spectra for gravity waves and agrees with those described earlier in §6.1. The estimated energy density, resulting from all the data extrapolated to the inertial period, gives a total value of 7.1×10^{-3} Jm^{-3}. This agrees well with the value obtained from the radio partial reflection wind technique of Vincent, (1984). Here the energy density of the wave spectrum is estimated at 7×10^{-3} Jm^{-3} for Adelaide and 6.5×10^{-3} Jm^{-3} for Townsville at the 85 km level. Manson et al, (1981), also using radio partial reflection wind observations, give seasonally averaged values for gravity wave energy densities at 95 km of $\simeq 10^{-3}$ Jm^{-3}. The λ557.7 nm observations of Battaner and Molina, (1980) give seasonal average energy densities of $6 \times 10^{-3} Jm^{-3}$, supported by comparable values from the photometric measurements of Meek and Manson, (1983).

The energy density has been calculated using a value for β of 0.9, consistent with the hypothesis that the altitude of the λ557.7 nm intensity maximum is greater than the altitude of the peak in the atomic oxygen profile as discussed in §2.5, table 2.5.1. For this hypothesis there is little difference between the Chapman or the Barth mechanisms since, using β = 0.8, the value for the Chapman mechanism, the energy density decreases to $5.6 \times 10^{-3} Jm^{-3}$ which is also consistent with the results of other workers.

For the case where $Q_{zm} \ll [O]_{zm}$, the value for β gives energy densities a factor of five lower than in the

case of $Q_{zm} = [O]_{zm}$ and over double for $Q_{zm} < [O]_{zm}$. So from agreement between observed results, it seems more likely that the λ557.7 nm emission peaks above the atomic oxygen maximum, although whether the Chapman or Barth mechanism dominates is still unclear.

7.3. Vertical group velocity.

The vertical component of the group velocity of a gravity wave packet is given by equation (2.3.4b) and from the dispersion equation (7.1.1) can be expressed as,

$$V_{gz} = \frac{-C^2[(\Omega^2 - f^2)/\Omega]k_z}{C^2(k_h^2 + k_z^2) - 2\Omega^2 + f^2 + N_A^2} \qquad (7.3.1.)$$

The negative sign signifying that the vertical components of the group and phase velocities are opposed in direction. From equation (7.3.1), the group velocities for each of the waves depicted in figure (7.1.1) have been calculated and are seen plotted in figure (7.3.1). As indicated, the boundaries which confine the observations in figure (7.1.1) also restrict the range of group velocities. These confines are labelled A and B ; the instrumental limitation boundaries are also shown. These boundaries have been extrapolated to the inertial period.

Despite the limited amount of data, particularly for the reduced field measurements, is seems that the group velocities are evenly distributed between the limiting boundaries; that is for a given permissable frequency interval, the vertical group velocity of a gravity wave at the 95 km level can lie anywhere within the boundaries.

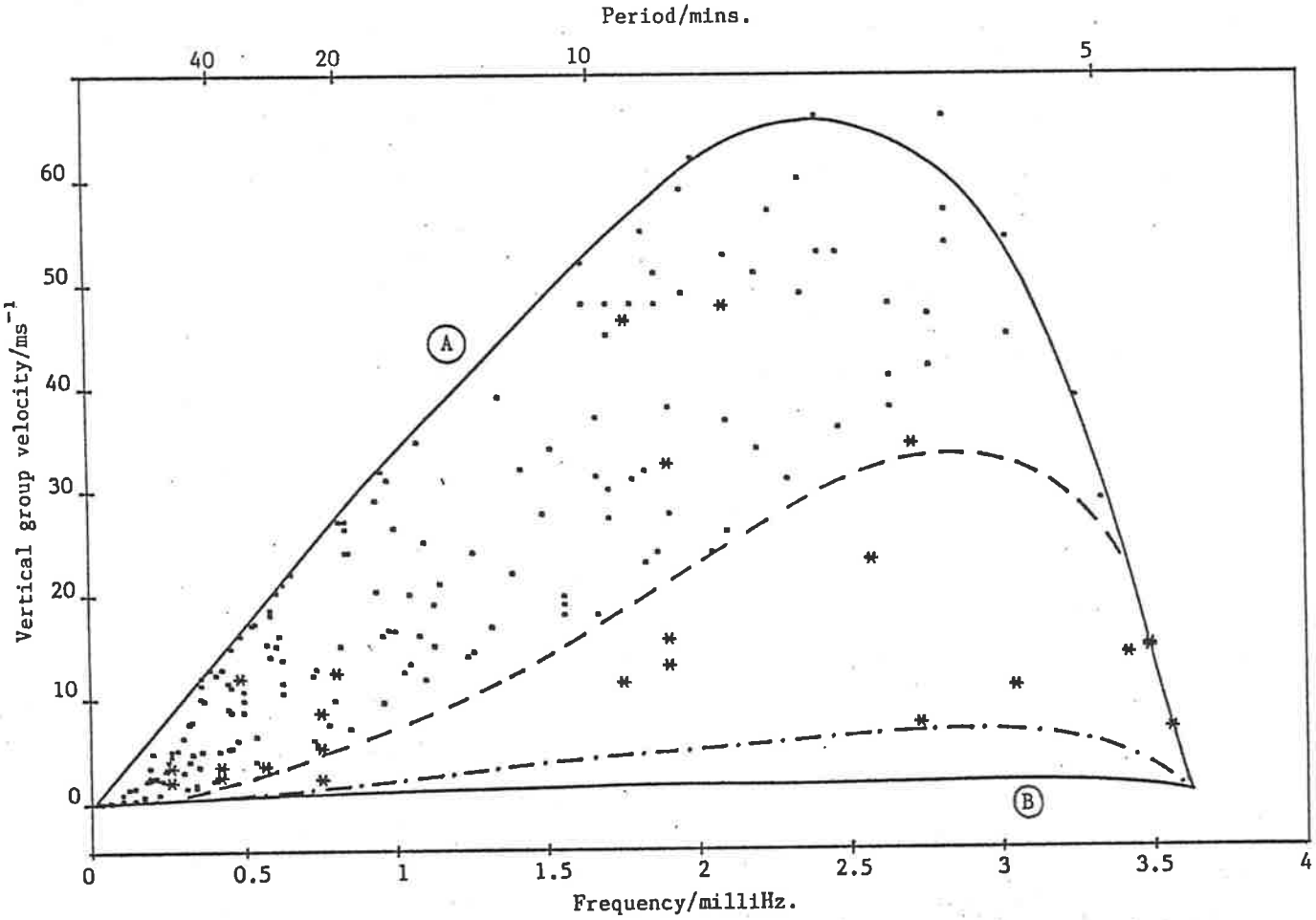

Figure 7.3.1. Distribution of gravity wave vertical group velocities from 3FP measurements. Consistent with Figure 7.1.1. are the reflection and dissipation boundaries A and B with the broken lines indicating the instrumental limitations.

This even distribution justifies the following procedure: the spectrum was divided into equal intervals of log frequency and a mean velocity, $\overline{V}_{gz}$, assigned for each interval, it being the average of the limiting velocities dictated by the upper and lower boundaries for that frequency interval i.e. curves A and B . Since gravity waves cannot propagate with frequencies less than the inertial frequency or larger than the Vaisala Brunt frequency, the vertical group velocity must vanish at these limits. The waves observed with horizontal wavelengths greater than those allowed by the viscous dissipation limit but less than the 5 km instrument limitation offer little weight to the mean vertical group velocity. The results of this average $\overline{V}_{gz}$ along with the line of best fit to the individual wave energy densities for all the data are plotted on the same graph in figure (7.3.2).

7.4. Vertical energy flux.

It is evident that an appreciable amount of energy, generated by tropospheric weather systems, is provided to the upper atmosphere via gravity waves, (Hines and Reddy, 1967). Although the main contributors to the gravity wave energy of the atmosphere are the large amplitude, long period waves, their near horizontal motions make the upward transport of this energy quite small. The mean vertical energy flux, or the average energy crossing unit

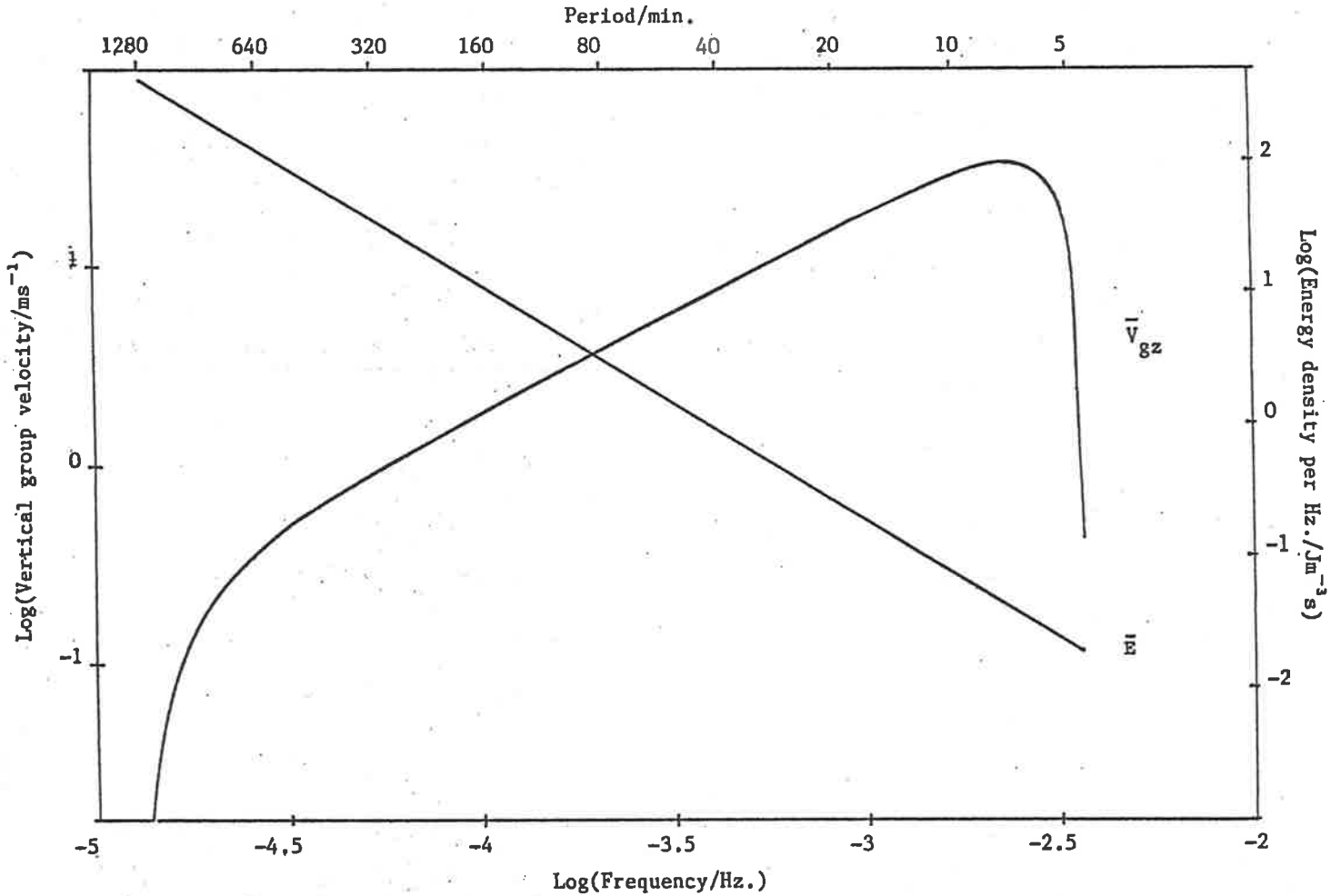

Figure 7.3.2. Mean gravity wave vertical group velocity spectrum averaged from the distribution shown in Figure 7.3.1. Also depicted is the mean gravity wave energy density calculated from 3FP energy density estimates. Both curves have been extrapolated to the inertial frequency.

area per second of a wave is

$$\overline{F}_z = \rho_o \overline{E}\,\overline{V}_{gz} \qquad (7.4.1.)$$

Figure (7.4.1) shows the energy flux of the gravity wave spectrum based on the product of the two curves of figure (7.3.2). The area under the curve of figure (7.4.1) is the total energy flux, extrapolated from 3FP measurements at the 95 km level. As can be seen, most of the total flux is contained in the shorter period waves, between 85% and 90% being contributed by waves with periods less than about four hours, periods directly measurable from 3FP observations.

Assuming that the data here represent a seasonal average and that the detected waves are incident on the 95 km level from below, then this analysis estimates the total upward energy flux to be about 15 mWm^{-2}. The seasonal average results from the 85 km level of Vincent, (1984) give fluxes of 13 mWm^{-2} for Adelaide and 12 mWm^{-2} for Townsville. Earlier investigations by Gossard, (1962) suggest vertical fluxes out of the troposphere from a variety of weather conditions, high as 150 mWm^{-2} for periodicities up to two hours. This value, although high, may be realistic since not all of the energy can be expected to reach the mesopause.

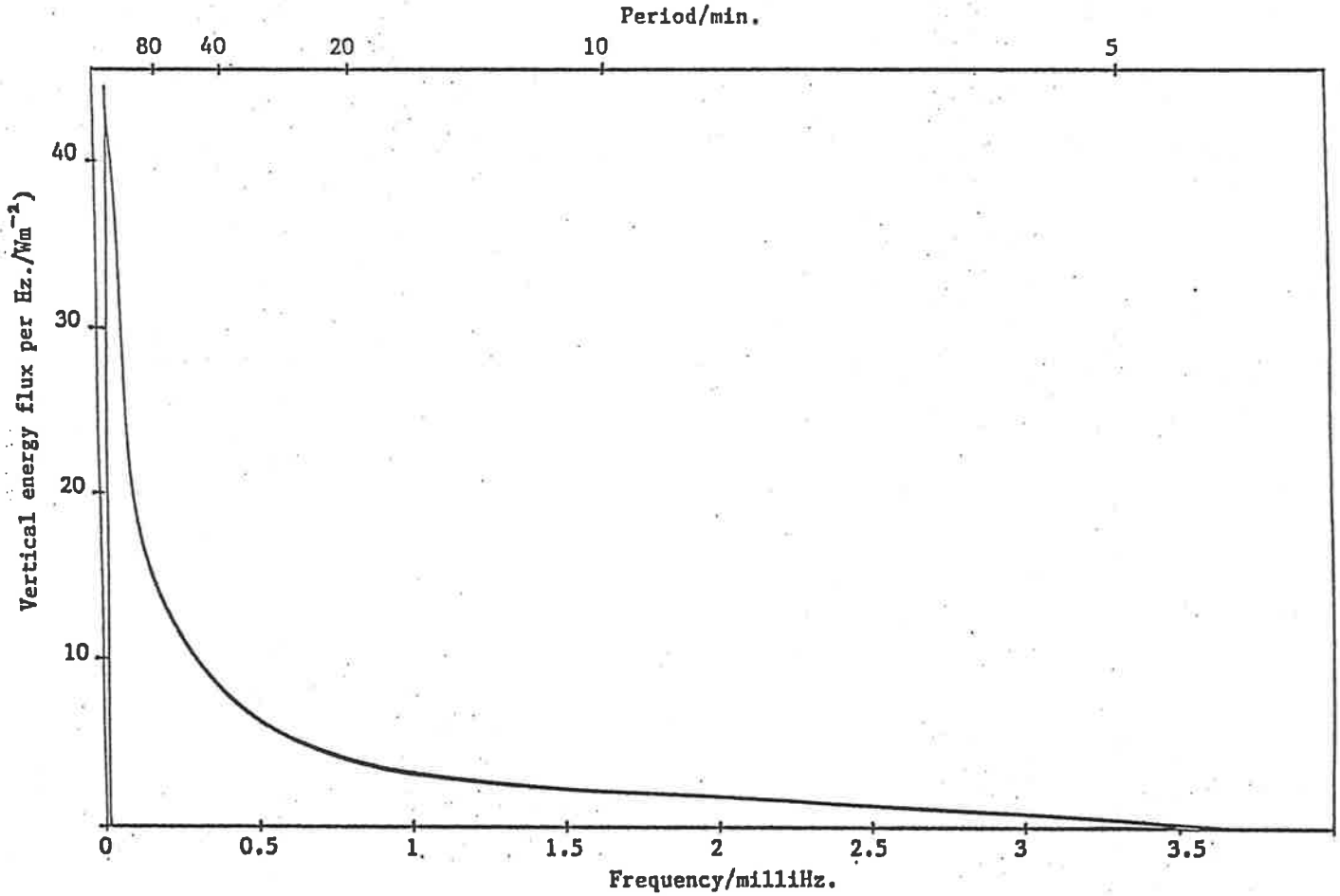

Figure 7.4.1. Gravity wave mean vertical energy flux spectrum calculated from the the product of the mean energy density and vertical group velocity spectra of Figure 7.3.2.

CONCLUSION.

Photometric measurements of fluctuations in the λ557.7 nm nightglow emission at 95 km caused by the passage of atmospheric gravity waves have been observed from three spaced fields of view. Cross spectral analysis of these observations has enabled the gravity wave field to be decomposed, isolating highly coherent periodicities. The period and horizontal phase velocity, in both magnitude and direction, are determined from the analysis and allow each detected wave to be assigned a horizontal wavelength.

The propagation direction of waves detected at 95 km clearly show evidence of polarization. This observation is consistent with reflection levels and critical coupling of waves by the mean flow of the middle atmosphere.

The gravity wave dispersion equation, derived from the linearized equations of motion, has enabled ray paths of waves detected at 95 km to be traced to the troposphere. The multilayer approach, using mean monthly meridional and zonal wind profiles, shows high correlation of gravity wave generation with tropospheric weather activity; in particular upper level jet streams with instances of thunderstorm and frontal disturbances contributing to wave generation.

The dispersion diagram of figure (7.1.1.) depicts good agreement between theory and experimental observations. The theoretical boundaries due to reflection and dissipation, the reverse ray tracings and the polarization

of the gravity wave field all give credibility to the proposal that the detected waves have their origin in the lower atmosphere. The theoretical boundaries, supported by experimental observation, limit the vertical wavelength of gravity waves and hence their vertical group velocities. The distribution of the vertical group velocity in figure (7.3.1.) justifies the assignment of a mean vertical group velocity extrapolated to the gravity wave inertial period.

Power spectra of the λ557.7 nm nightglow observations also permit the mean gravity wave energy density spectrum to be estimated. The shape and slope of this spectrum is consistent with those of other workers and allow the energy spectrum to be extrapolated to cover the entire gravity wave frequency range. Given the mean energy and vertical group velocity spectra, the mean vertical energy flux spectrum follows. Integration of this spectrum gives a total vertical energy flux of around 15 mWm^{-2} with the majority of this energy being transported upwards. It is also determined that over 85% of this energy flux is contributed by gravity waves with periods less than about 4 hours; periods directly observable by the three field photometer.

The most severe limitation of the instrument is its restriction to night time observing under favourable seeing conditions. Despite this limitation it has been demonstrated that useful information on the dynamics of medium scale gravity waves can be extracted from only a few nights data and that this information agrees well with theory and the results of other workers.

The flexibility of the three field photometer permits other nightglow emissions to be observed; either individually or simultaneously. An example of a combination of emissions is the OH (8-3) band at about 85 km and the λ630 nm emission at 250 km. These together with the λ557.7 nm emission at 95 km will allow gravity waves to be investigated at three separate levels simultaneously and may provide direct measurements on vertical as well as horizontal wavelengths of gravity waves as they propagate through the atmosphere.

References.

Armstrong E.B. "The association of visible airglow features with gravity waves." J.Atmos. Terr. Phys. 44, No. 4, p325, 1982.

Ball S.M. "Upper atmospheric tides and gravity waves at mid- and low- latitudes." Ph. D. thesis, University of Adelaide, 1981.

Balsley B.B. and Carter D.A. "The Spectrum of Atmospheric Velocity Fluctuations at 8 km and 86 km." Geophys. Res. Lett. 9, No. 4, p465, 1982.

Barth C.A. and Hilderbrant A.F. "The 5577A Airglow Emission Mechanism." J. Geophys. Res. 66, p985, 1961.

Battaner E. "Transport phenomena and the chemical composition in the mesosphere and lower thermosphere." J.Atmos. Terr. Phys. 37, p1155, 1975.

Battaner E. and Molina A. "Turbopause Internal Gravity Waves, 557.7 nm Airglow, and Eddy Diffusion Coefficient." J.Geophys. Res. 85, No. A12, p6803, 1980.

Bertin F., Testud J. and Kersley L. "Medium scale gravity waves in the ionospheric F-Region and their possible origin in weather disturbances." Planet. Space Sci. 23, p493, 1975.

Bevington P.R. "Data Reduction and Error Analysis for the Physical Sciences."
McGraw Hill, New York, 1969.

Blifford I.H. "Factors Effecting the Performance of Commercial Interference Filters."
App. Optics 5, No.1, p105, 1966.

Booker J.R. and Bretherton F.P. "The critical layer for internal gravity waves in shear flow."
J. Fluid Mech., 27, p513, 1967.

Bracewell R.N. "The Fourier Transform and its Applications." second ed.
Mc Graw-Hill Kogakusha Ltd, Tokyo, 1965.

Brault J.W. and White O.R. "The Analysis and Restoration of Astronomical Data via the Fast Fourier Transform."
Astron. and Astrophys. 13, p169, 1971.

Briggs B.H. "On the analysis of moving patterns in geophysics I. Correlation Analysis."
J.Atmos. Terr. Phys. 30, p1777, 1968.

Briggs B.H. and Golley M.G. "A test for dispersion in F region drifts observed by the radio star scintillation method."
J. Atmos. Terr. Phys. 30, p963, 1968.

Brigham E.O. "The Fast Fourier Transform."
Prentice-Hall, New Jersey, 1974.

Broadfoot A.L. and Kendall K.R. "The Airglow Spectrum 3100-10,000 Å."
J. Geophys. Res., Sp. Phys. 73, No. 1, p 426, 1968.

Carter D.A. and Balsley B.B. "The Summer Wind Field between 80 km and 93 km Observed by the MST Radar at Poker Flat, Alaska (65° N)." J. Atmos. Sci. 39, p2905, 1982.

Chamberlain J.W. "Physics of Aurora and Airglow." Acedemic Press, New York, 1961.

Chamberlain M.T. and Jacka F. "Optical evidence for mid latitude particle precipitation." J. Atmos. Terr. Phys. 41, p111, 1979.

Chapman S. "Some phenomena of the upper atmosphere." Proc. R. Soc. London, Ser A, 132, p353, 1931a.

Chapman S. "The absorption and dissociative or ionizing effects of monochromatic radiation in an atmosphere on a rotating earth." Proc. Phys. Soc. 42, p26, 1931b.

Chimonas G. and Hines C.O. "Atmospheric gravity waves launched by auroral currents." Planet. Space Sci. 18, p565, 1970.

C.I.R.A. Cospar International Reference Atmosphere, North-Holland Publ. Co., Amsterdam, 1965.

Cowling D.H., Webb H.D. and Yeh K.C. "Group Rays of Internal Gravity Waves in a Wind Stratified Atmosphere." J.Geophys. Res. 76, No. 1, p213, 1971.

Dandekar B.S. and Turtle J.P. "Atomic Oxygen Concentration from the measurement of the [OI] 5577A Emission of the Airglow." Planet. Space Sci. 19, p949, 1971.

Davies W.E.R. "Reduction of Dark Current in Photomultiplier Tubes."
Rev. of Scientific Instr. 43, No.3, p556, 1972.

Dudis J.J. and Reber C.A. "Composition effects in Thermospheric Gravity Waves."
Geophys. Res. Lett., 3, No. 12, p727, 1976.

Eather R.H. and Reasoner D.L. "Spectrophotometry of Faint Light Sources with a Tilting Filter Photometer."
App. Optics, 8, No. 2, p227, 1969.

Fogle B. and Haurwitz B. "Noctilucent Clouds."
Space Sci. Rev., 6, p279, 1966.

Francis S.H. "Global propagation of atmospheric gravity waves: a review."
J.Atmos. Terr. Phys. 37, p1011, 1975.

Francis S.H. "Propagation of internal acoustic waves around a spherical earth."
J.Geophys. Res. 77, p4221, 1972.

Frederick J.E. "Influence of Gravity Wave Activity on Lower Thermospheric Photochemistry and Composition."
Planet. Space Sci. 27, p1469, 1979.

Freund J.T. and Jacka F. "Structure in the λ557.7 nm [OI] airglow."
J.Atmos. Terr. Phys. 41, p25, 1979.

Gavrilov N.M. and Shved G.M. "A Study of Internal Gravity Waves in the lower Thermosphere based on Skyglow Isophots."
Atmosp. and Oceanic Phys. 18, No. 1, p5, 1982.

Geller M.A. "Dynamics of the middle atmosphere."
J.Atmos. Terr. Phys. 41, p683, 1979.

Georges T.M. "Evidence for the influence of atmospheric waves on ionospheric motions."
J.Geophys. Res. 72, p422, 1967.

Georges T.M. and Young J.M. "Remote sensing of the troposphere."
ed. V.E. Torr, US Government Printing Office, Washington. 1972.

Gossard E.E. "Vertical Flux of Energy into the Lower Ionosphere from Internal Gravity Waves Generated in the Troposphere."
J.Geopyhs. Res. 67, No. 2, p745, 1962.

Gossard E.E. and Hooke W.H. "Waves in the Atmosphere."
Elsevier Scientific Publ. Co., 1975.

Groves G.V. "Wind Models from 60 to 130 km Altitude for Different Months and Latitudes."
J. of the British Interplanetaty Soc. 22, p285, 1969.

Groves G.V. "Atmospheric structure and its variation."
Airforce Cambridge Res. Labs. Environ. Res. paper 368, 1971.

Gulledge I.S., Packer D.M., Tilford S.G. and Vanderslice J.T. "Intensity Profile of the 6300A and 5577A OI Lines in the Night Airglow." J.Geophys. Res. 73, No. 17, p5535, 1968.

Harker Y.D., Masso J.D. and Edwards D.F. "Merits of Photomultiplier Cooling for Photon Counting Experiments." App. Optics 8, No.12, p2563, 1969.

Herron J.T. "Phase velocity dispersion of F-region waves." J. Atmos. Terr. Phys. 35, p101, 1973.

Hines C.O. "The Upper Atmosphere in Motion." American Geophysical Union, Washington D.C., 1974.

Hines C.O. "The Upper Atmosphere in Motion." Q.J.Roy. Meteorl. Soc., 89, p1, 1963.

Hines C.O. "Internal Atmospheric Gravity Waves at Ionospheric Heights." Can. J. Phys., 38, p1441, 1960.

Hines C.O. "A Possible Source of Waves in Noctilucent Clouds." J. Atmos. Sci., 25, p937, 1968.

Hines C.O. and Reddy C.A. "On the Propagation of Atmospheric Gravity Waves through Regions of Wind Shear." J.Geophys. Res. 72, p1015, 1967.

Hunsucker R.D. "Atmospheric Gravity Waves Generated in the High Latitude Ionosphere: A Review." Rev. of Geophys. and Space Phys. 20, No. 2, p293, 1982.

Hunten D.M. "Airglow- Introduction and Review." The Radiating Atmosphere. D. Reidel Publ. Co. Dordrecht, Holland, 1971.

Hunten D.M. "Spectroscopic Studies of the Twilight Airglow." Space Sci. Rev. 6, D Reidel Publ. Co. Dordrecht, Holland. 1967.

Jenkins G.M. "General Considerations in the Analysis of Spectra." Technometrics 3, No.2, p133, 1961.

Jenkins G.M. and Watts D.G. "Spectral Analysis and its Applications." Holden Day, San Fransisco, 1969.

Jonas M. and Alon Y. "Dependence of Signal-to-Noise Ratio on Operating Voltages in Photomultipliers." App. Optics 10, No.11, p2436,1971.

Jordan A.R. "Atmospheric Gravity Waves from Winds and Storms." J. Atmos. Sci. 29, p445, 1972.

Julian P.R. "Comments on the Determination of Significance Levels of the Coherence Statistic." J. Atmos. Sci. 32, p836, 1975.

Kersley L. and Rees P.R. "Tropospheric gravity waves and their possible association with medium scale travelling ionospheric disturbances." J. Atmos. Terr. Phys. 44, No. 2. p147, 1982.

Larsen M.F., Kelley M.C. and Gage K.S. "Turbulence Spectra in the Upper Troposphere and Lower Stratosphere at Periods Between 2 Hours and 40 Days." J. Atmos. Sci. 39, p1035, 1982.

Lillen W. and Whipple F.L. "High altitude winds by meteor trail photography." J. Atmos. Phys., Spec. Suppl. 1. p112, 1954.

Lindzen R.S. "Tides and Gravity Waves in the Upper Atmosphere." Mesospheric Models and Related Experiments. D. Reidel Publ. Co., Dordrecht-Holland, 1971.

Manson A.H. and Meek C.E. "Gravity waves of short period (5-90 min), in the lower thermosphere at 52°N (Saskatoon, Canada)" J.Atmos. Terr. Phys. 42, p103, 1980.

Manson A.H., Gregory J.B. and Meek C.A. "Atmospheric Waves (10 min-30 days) in the Mesosphere at Saskatoon (52°N, 107°W), October 1978-September 1979." Planet. Space Sci. 29, p615, 1981.

Martyn D.F. "Cellular atmospheric waves in the ionosphere and troposphere." Proc. Roy. Soc. Ser a, 201, p216, 1950.

Mastrantonio G., Einaudi F., Fua D. and Lalas D.P. "Generation of Gravity Waves by Jet Streams in the Atmosphere." J. Atmos. Sci. 33, p1730, 1976.

McEwan M.J. and Phillips L.F. "Chemistry of the Atmosphere." Edward Arnold Publ. Ltd., London, 1975.

Meek C.E. and Manson A.H. "Measurements of the structure and drift velocities of airglow (λ=557.7 nm) irregularities; Saskatoon (52°N, 107°W), Canada." J.Atmos. Terr. Phys. 45, No. 4, p203, 1983.

Merril J.T. "Observational and theoretical study of Shear Instability in the Airglow near the Ground." J. Atmos. Sci. 34, p911, 1977.

Molina A. "Visible Continuum Emission and Gravity Waves." Planet. Space Sci. 31, No. 3, p331, 1983.

Munro G.H. "Travelling ionospheric disturbances in the F region." Aust. J. Phys. 11, p91, 1958.

Murgatroyd R.J. and Singleton F. "Possible meridional circulations in the stratosphere and mesosphere." Q.J.Roy. Meteorol. Soc. 87, p125, 1961.

Offermann D. and Drescher A. "Atomic Oxygen Densities in the Lower Thermosphere from In Situ 5577A Night Airglow and Mass Spectrometer Measurements."
J.Geophys. Res. 78, No 28, p6690, 1973.

Oke J.B. and Schild R.E. "A Practical Multiple Reflection Technique for Improving the Quantum Efficiency of Photomultiplier Tubes."
App. Optics 7, No.4, p617, 1968.

Pitteway M.L.V. and Hines C.O. "The Viscous Damping of Atmospheric Waves."
Can. J. Phys. 41, p1935, 1963.

Pitteway M.L.V. and Hines C.O. "The Reflection and Ducting of Atmospheric Acoustic-Gravity Waves."
Can. J. Phys. 43, p2222, 1965.

Rao M.N.M., Murty G.S.N. and Jain V.C. "Altitude of peak emission of (OI) 5577A in the lower thermosphere: Chapman versus Barth mechanisms."
J.Atmos. Terr. Phys. 44, No 7, p559, 1982.

Ratcliffe J.A. "An introduction to the ionosphere and magnetosphere."
Cambridge University Press, 1972.

Richards P.I. "Computing reliable Power Spectra."
IEEE spectrum p83,1967.

Richmond A.D. "Gravity Wave generation, Propagation and Dissipation in the Thermosphere."
J.Geophys. Res. 83, No. 9, p4131, 1978.

Rottger J. "Travelling disturbances in the equatorial ionosphere and their association with penetrative cumulus convection."
J.Atmos. Terr. Phys. 39, p987, 1977.

Slanger T.G. and Black G. "O(^{1}S) in the lower thermosphere -Chapman vs Barth."
Planet. Space Sci. 25, p79, 1977.

Thomas R.J. and Young R.A. "Measurement of Atomic Oxygen and Related Airglows in the lower Thermosphere."
J.Geophys. Res. 86 No. C8, p7389, 1981.

Tohmatsu T. and Nagata T. "Dynamical Studies of the Oxygen Green Line in the Airglow."
Planet. Space Sci. 10, p103, 1963.

Tolstoy I. "The Theory of Waves in Stratified Fluids Including the Effects of Gravity and Rotation."
Rev. of Modern Physics 35, No.1, p207, 1963.

Townsend A.A. "Internal waves produced by a convective layer."
J. Fluid Mech. 24, p307, 1966.

US Standard Atmosphere, 1976.
NOAA US Gov. Printing Office, Washington.

Vincent R.A. "A criterion for the use of the multilayer approximation in the study of acoustic-gravity wave propagation."
J.Geophys. Res. 74, p2996, 1969.

Vincent R.A. "Gravity-wave motions in the mesosphere." J.Atmos. Terr. Phys. 46, No. 2, p119, 1984.

Vincent R.A. and Ball S.M. "Mesospheric Winds at Low and Mid Latitudes in the Southern Hemisphere." J.Geophys. Res. 86, p9159, 1981.

Waldock J.A. and Jones T.B. "The effects of neutral winds on the propagation of medium-scale atmospheric gravity waves at mid latitudes." J.Atmos. Terr. Phys. 46, No 3, p217, 1984.

Weinstock J. "Theory of the Interaction of Gravity Waves with $O_2(^1\Sigma)$ Airglow." J.Geophys. Res. 83, No A11, p5175, 1978.

Witt G. and Stegman J. "A measurement of the $O_2(b\Sigma_g^+ - X^3\ \Sigma_g^-)$ Atmospheric Band and the $OI(^1S)$ Green Line in the Nightglow." Planet. Space Sci. 27, p341, 1979.

Yeh K.C. and Liu C.H. "Acoustic-Gravity Waves in the Upper Atmosphere." Rev. Geophys and Space Phys. 12, No. 2, p193, 1974.

Yeh K.C., Webb H.D. and Cowling D.H. "Evidence of directional filtering of travelling ionospheric disturbances." Nature Phys. Sci. 235 (59), p131, 1972.

POSTSCRIPT.

It has come to my attention that the effect the tidal components have on the wind profiles used for gravity wave tracings is somewhat understated, (§5.3). It is therefore appropriate that in this postscript I elaborate on why the tidal components were not included in the wind profiles.

Clearly, any change to the wind profiles used for ray tracings will affect the position of gravity wave launch sites at the tropopause. Initial ray tracings were conducted using two separate sets of monthly averaged meridional and zonal wind profiles adapted from Groves (1969,1971), CIRA (1965) and Murgatroyd and Singleton (1961) for the region between 30 km and 95 km. The general trend of wind velocity with altitude for these two sets were similar although the magnitude of the wind components, particularly in the height range of 80 km to 95 km, often differed considerably for the months of the observations.

Ray tracings using these two wind profile sets on the same observed wave parameters, naturally gave rise to different launch sites. However, the general regions of these launch sites in most cases were maintained due to the similarity of the overall trend of velocity with altitude in the profiles. The launch sites, in a great many cases, could still be attributed to the same possible wave generation mechanisms which are discussed in §5.6.

In only a few cases, for waves where the horizontal phase velocity and period were such as to be most sensitive

to the wind field, the two wind sets gave rise to significantly different ray tracings. Accurate tracings for these waves can only be carried out with a precise knowledge of the wind field, including tidal components, for the nights in question - an unrealistic expectation.

However, the two sets of wind profiles for the majority of tracings did not significantly alter the regions of likely gravity wave generation. It was clear that the error in the tracings introduced by the differences in these wind profiles would be larger than those incurred by including the tidal components in the 80km to 95 km region. Additional complications would also arise from including the tidal components due to their temporal variations, particularly the semi diurnal component.

For these reasons, along with those pointed out in §5.3, it was decided not to include the tidal components in the wind profiles used for the tracings since the purpose of the tracings could be realized without their inclusion. For clarity of presentation an average of the two wind profile sets was used for the final tracings which are presented in §5.5.

In summary, all tracings are sensitive to the wind profile to a variable extent. The tracing presented in this thesis, culminating in proposed launch sites and likely wave sources, are obviously those waves which are least sensitive to the mean wind profile.

A further comment should also be made regarding the points plotted on the log k_z, log k_x diagram of Figure (7.1.1). Here estimates of the wind field at 95 km are used to determine the intrinsic wave frequency and the log k_z coordinate via the dispersion relation of equation (7.1.1). Again the tidal components were not included, giving some doubt to the integrity of the positions of these points.

Since the horizontal wave number, k_h is invariant then any variation in the intrinsic frequency of a wave, brought about by an uncertainty in the wind field, will result in its representative point being displaced only vertically on the diagram.

The purpose of this diagram is to verify the linearized theory of gravity waves with experiment and more importantly to identify restraints in the vertical wave number of detected gravity waves. These constraints in turn lead to an upper limit to the vertical group velocity of these waves which allow estimates of vertical energy flux to be made, (§7.3). In this context it is only the integrity of boundary A which need be considered since, from Figure 7.3.1, boundary B offers little weight to the restriction in the vertical group velocities of the waves.

Again the question arises as to how much the real wind fields at 95 km during the observing times differ from the estimates used and whether the inclusion of an estimate of the tidal components significantly improves the results.

The following argument is a quantitative analysis resulting in the error in log k_z as a function of the error in the wind velocity. Since the horizontal wave number is invariant and derived from the observed horizontal phase velocity and wave period, the error associated with it is considered negligable compared to the error in the intrinsic wave frequency which directly results from an uncertainty in the magnitude of the wind field.

Consider the asymptotic approximation to the dispersion equation given by equation (7.1.5). Taking the logarithm of both sides and rearranging gives,

$$\log k_z = \tfrac{1}{2}\log (N^2 - \Omega^2) + \log k_h - \log \Omega$$

It is then straightforward to show that the error in log k_z is related to the relative error in the intrinsic frequency by,

$$\Delta \log k_z \doteq 0.43\, \Delta\Omega / \Omega \qquad (1)$$

Recalling equation (5.2.1), $\Omega = \omega - U k_h$ where U is the horizontal component of the wind velocity and ω the observed wave frequency. Since $\Delta\omega$ is considered negligable then,

$$\Delta\Omega/\Omega = Uk_h/\Omega \quad \text{or} \quad \Delta\Omega/\Omega = U/V_{int} \qquad (2)$$

where V_{int} is the intrinsic wave phase velocity.

Combining equations (1) and (2) gives,

$$\Delta \log k_z \doteqdot 0.43 \, \Delta U / V_{int} \qquad (3)$$

Empirical evaluations using the full dispersion equation (7.1.1) verify the above result and validate the use of the asymptotic approximation in deriving equation (3).

Referring back to Figure (7.1.1), the boundary designated by A corresponds to gravity waves with intrinsic phase velocities of around 170 m/s. For an error in the magnitude of the wind velocity of say ΔU = 40 m/s, which is more than adequate to account for tidal variations, then from equation (3) $\Delta \log k_z$ is only 0.1 for a wave travelling in the same direction as the wind.

Naturally a full knowledge of the wind field at 95km during the observing times would give greater accuracy to the position of the points plotted in Figure (7.1.1), particularly those of low horizontal phase velocity. Some initial studies, beyond the scope of this thesis, were conducted using reduced field measurements as described in §7.1 to measure the wind at the λ557.7 nm emission level. These measurements use autocorrelation techniques to follow turbulent patches of airglow as they are advected by the mean flow to infer the background wind.

It is hoped in the future that spectral and auto-correlation analyses may be used on the 3FP observations to simultaneously measure, both temporally and spacially,

gravity wave parameters and wind velocities to allow more accurate determination of gravity wave energy flux at the 95km level.